



**Leap forward in Space Weather forecast:**

**Novel prediction of flares**

**Marianna Brigitta Korsós**

**Submitted for the degree of  
Doctor of Philosophy**

**School of Mathematics and Statistics**

**2018**

**Supervisor: Professor Michael S. Ruderman**

**The University of Sheffield**

## DECLARATION

I, Marianna Korsós, hereby certify that I am the author of this thesis and that all the work presented in it, unless otherwise referenced, is entirely my own. The thesis work was conducted from April 2015 to November 2018 under the supervision of Professor Michael S. Ruderman at University of Sheffield. I also declare that this work has not been submitted, in whole or in part, to any other university for any degree or other qualification.

---

Marianna Korsós

---

Date

## ACKNOWLEDGEMENTS

First of all, I would like to give my special thanks to my supervisor, Prof. Michael S. Ruderman. Without his continuous motivation, invaluable intellectual support and help of various kinds, this dissertation could barely be accomplished. I would like to give a huge thanks to Prof. Robertus Erdélyi for his unlimited useful discussions, intellectual guidance and his endless support during my PhD. I would also like to thank to Profs Manolis Georgoulis (Academy of Athens), Stefaan Poedts (KU Leuven), Yihua Yan (Chinese Academy of Sciences), Dr. Norbert Gyenge (University of Sheffield), Drs Susanta Bisoi (Chinese Academy of Sciences), Sijie Yu (New Jersey Institute of Technology) and Piyali Chatterjee (Indian Institute of Astrophysics) for their indispensable contributions to my research, which came in many critical discussions and advises and provided program codes for my PhD topic. I cannot quite believe I have been so lucky as to have such excellent mentors and supporters. They have been so generous with their time and efforts over the past three-and-a-half years and have given me something to really aspire to. I would not be in the position I am today if it had not been for their support and belief.

Secondly, I would like to express my gratitude to all of the funding bodies and institutions who have contributed financially to my studies, including my stipend and travel budget which came from University of Sheffield.

I would also like to thank to my advisor Prof. Shaun Quegan, my Co-Supervisor Dr. Viktor Fedun for their assistance and all the wonderful members of SP2RC who have put up with me in my good and challenging times.

I am also so extremely grateful to my extended family and my close friends in Sheffield, especially my lovely Hungarian, Chinese and Russian friends.

## Refereed publications in the thesis

**Korsós, M. B.**, S. Yang , Erdélyi, R: *Pre-flare dynamic investigation by weighted horizontal magnetic gradient method: From small to major flare class*, 2019, Journal of Space Weather and Space Climate, under review, (accepted)

**Korsós, M. B.**, Chatterjee, P., Erdélyi, R.: *Applying the Weighted Horizontal Magnetic Gradient Method to a Simulated Flaring Active Region*, 2018, The Astrophysical Journal, 857, 103

**Korsós, M. B.**, Poedts, S., Gyenge, N., Georgoulis, M. K., Yu, S., Bisoì, S. K., Yan, Y., Ruderman, M. S., Erdélyi, R.: *On the evolution of pre-flare patterns of a 3-dimensional model of AR 11429*, 2018, Space Weather of the Heliosphere: Processes and Forecasts, Proceedings of the International Astronomical Union, IAU Symposium, Volume 335, pp. 294-297

Ye, Y., **Korsós, M. B.**, Erdélyi, R.: *Detailed analysis of dynamic evolution of three Active Regions at the photospheric level before flare and CME occurrence*, 2018, Advances in Space Research, 61, 2, 673-682

**Korsós, M. B.**, Ruderman, M. S., Erdélyi, R.: *An application of the weighted horizontal magnetic gradient to solar compact and eruptive events*, 2018, Advances in Space Research, 61, 595-602

**Korsós, M. B.**, and Ruderman, M. S.: *On Flare and CME Predictability Based on Sunspot Group Evolution*, 2016, ASP Conference Series, Vol. 504. San Francisco: Astronomical Society of the Pacific, 43

# Abstract

In this thesis, our aim was to further test and develop our  $WG_M$  flare prediction method. First, we extended the number and GOES flare intensity range of the previously applied data sample to reinforce the two diagnostic properties of the  $WG_M$  method. This extended statistical sample confirmed that the characteristic pre-flare behaviour of the  $WG_M$  and distance ( $D_{pm}$ ) parameters both need to appear concurrently for a follow-up flaring to take place in a  $\delta$ -spot. Furthermore, we verified the relationship between the value of highest flare class intensity (from B- to X-class) of a flaring AR and the maximum value of  $WG_M$ . Also, the new sample reaffirmed the linear connection between the duration of the converging and diverging motions of the barycenters of opposite polarities up to flare onset.

Next, we further probed the  $WG_M$  method, by applying it to magneto-hydrodynamic simulations modelling solar-like flares. The pre-flare evolution of  $WG_M$  and the behavior of  $D_{pm}$  at various heights identified in the simulated sample  $\delta$ -type AR were investigated as a case study. We identified the optimum heights where  $D_{pm}$  yielded the earliest sign of pre-flare behaviour, compared its to photospheric counterpart. These loci in height, found for being most beneficial for predicting flares, agree reasonably well with the heights of the occurrence of flares themselves. We also estimated the expected time of flare onsets from the durations of the converging-diverging motion of the barycenters of opposite polarities before each flare. The estimated onset time and the actual time of occurrence of each flare were in good agreement at the corresponding optimum heights.

Finally, based on the analyses of the simulated flaring AR cases, we proposed to extend our studies into 3D embracing a solar atmospheric region from the photosphere into low corona. To make advances, over a dozen of ARs were analysed. We showed that if the optimum height is between 1000-1800 km in the solar atmosphere then this would allow us to increase the flare prediction with 3.2 hrs  $\pm 2.5$  hours lead time.

# Contents

<b>List of Figures</b>	<b>viii</b>
<b>List of Tables</b>	<b>xi</b>
<b>1 Introduction</b>	<b>1</b>
1.1 The Sun . . . . .	1
1.2 Active Regions . . . . .	5
1.3 3D magnetic field of solar ARs . . . . .	9
1.4 Energy Build-up before Flares and CMEs . . . . .	16
1.5 Energy Release - Magnetic Reconnection . . . . .	18
1.6 Standard solar flare and CME occurrence model . . . . .	22
1.7 The classification of solar eruptions . . . . .	26
1.7.1 Flare classification . . . . .	27
1.7.2 Coronal Mass Ejection (CME) classification . . . . .	28
1.8 Space Weather . . . . .	29
1.9 Thesis Aims . . . . .	34
<b>2 Data initialisation and database</b>	<b>38</b>
2.1 Data source . . . . .	39
2.1.1 Zeeman effect . . . . .	39
2.1.2 Michelson interferometer . . . . .	41

2.1.3	Stokes-parameters . . . . .	42
2.1.4	Magnetic field measurements in space . . . . .	43
2.1.5	Transformation of sunspot coordinates . . . . .	47
2.2	Applications . . . . .	49
2.2.1	The $WG_M$ method . . . . .	50
2.2.2	Geostationary Operational Environmental Satellites - GOES flare list . . . . .	53
2.2.3	Photospheric investigation . . . . .	55
2.2.4	The 3D analyses . . . . .	60
<b>3</b>	<b>From B- to X-class flares</b>	<b>66</b>
3.1	Introduction . . . . .	67
3.2	Applying the $WG_M$ method . . . . .	68
3.2.1	Example for intensive X- and M-class flare case . . . . .	69
3.2.2	Example for weak M-class flare case . . . . .	71
3.2.3	Example for C-class flare case . . . . .	72
3.2.4	Example for microflare case . . . . .	73
3.2.5	Example for non-flaring case . . . . .	75
3.3	Statistical analyses . . . . .	77
3.4	Visualisation of pre-flare behaviour of $D_{pn}$ . . . . .	80
3.5	Conclusion . . . . .	83
<b>4</b>	<b>An simulated <math>\delta</math>-type flaring Active Region</b>	<b>85</b>
4.1	Introduction of applied simulation . . . . .	86
4.2	Testing the $WG_M$ method . . . . .	92
4.2.1	At the photosphere . . . . .	93
4.2.2	At 0.59 Mm level in the low chromosphere . . . . .	95
4.2.3	At 1.28 Mm in middle chromosphere . . . . .	95
4.2.4	At 3.24 Mm above the photosphere . . . . .	97

<i>CONTENTS</i>	vii
4.3 Searching for Optimum height(s) . . . . .	99
4.4 Conclusions . . . . .	102
<b>5 Magneticfield Extrapolation</b>	<b>104</b>
5.1 Introduction . . . . .	105
5.2 Comparison analyses of PF and NLFFF . . . . .	106
5.2.1 AR 11158 . . . . .	110
5.2.2 AR 11166 . . . . .	112
5.2.3 AR 11283 . . . . .	113
5.3 Application of PF to more ARs . . . . .	128
5.4 Conclusions . . . . .	132
<b>6 Conclusions and Future Work</b>	<b>134</b>
6.1 Principal Results . . . . .	135
6.2 Future Work . . . . .	140
<b>A Appendix</b>	<b>142</b>
A.1 List of investigated ARs in Chapter 3 . . . . .	142
A.2 List of investigated ARs in Chapter 5 . . . . .	150

# List of Figures

1.1	Cartoon view of the structure of the Sun . . . . .	2
1.2	VAL atmospheric column model . . . . .	5
1.3	3D structure of a sunspot . . . . .	7
1.4	Babcock Solar Dynamo Model . . . . .	8
1.5	McIntosh sunspot groups classification system . . . . .	10
1.6	Comparison of extrapolated field lines with AIA 171 Å coronal loops for AR 11158 . . . . .	15
1.7	Magnetic helicity . . . . .	17
1.8	Reconnection models . . . . .	20
1.9	CSHKP flare and CME model . . . . .	23
1.10	Eruptive events on the Sun . . . . .	26
1.11	The types of the detected CME . . . . .	30
1.12	Traveling time of solar particles to the Earth . . . . .	31
1.13	Space Weather . . . . .	32
1.14	Transformer severe internal damage . . . . .	33
2.1	Zeeman effect . . . . .	40
2.2	Michelson interferometer . . . . .	42
2.3	Vector magnetic field component . . . . .	44
2.4	MDI and HMI instruments . . . . .	45
2.5	Cartesian and Polar coordinate systems . . . . .	48

2.6	Illustration for the $WG_M$ proxy . . . . .	51
2.7	Illustration of the two characteristics pre-flare behaviors . . . . .	52
2.8	GOES flare catalogue . . . . .	54
2.9	Debrecen Data catalogue . . . . .	57
2.10	The $WG_M$ application on the solardisc . . . . .	58
2.11	Extrapolated magnetic structure of AR 11158 . . . . .	61
2.12	Automatic identification of $\delta$ -spots . . . . .	64
3.1	AR 11429 with intensive flare class . . . . .	70
3.2	AR 11504 with weak M-class flares . . . . .	73
3.3	AR 11281 with C-class flares . . . . .	74
3.4	AR 11967 with microflare . . . . .	75
3.5	AR 11495 - Non-flaring case . . . . .	76
3.6	Relationship of the $WG_M^{max}$ and flare intensity class . . . . .	78
3.7	Statistical analyses of the $D_{pn}$ . . . . .	79
3.8	Visualisation of pre-flare behaviour of $D_{pn}$ . . . . .	81
4.1	The initial state of the simulated 3D $\delta$ -spot . . . . .	87
4.2	The local temperature map of the four flares . . . . .	89
4.3	The $\bar{Q}_{FL}$ obtained by integrating the Ohmic heating . . . . .	91
4.4	Evolution of various pre-flare indicators in the photosphere . . . . .	94
4.5	Evolution of various pre-flare indicators at 500 km . . . . .	96
4.6	Evolution of various pre-flare indicators at 1284 km . . . . .	97
4.7	Evolution of various pre-flare indicators at 3240 km . . . . .	98
4.8	Distance parameter as a function of height . . . . .	101
5.1	3D visitation of the AR 11158 . . . . .	106
5.2	3D visitation of the AR 11166 . . . . .	107
5.3	3D visitation of the AR 11283 . . . . .	107

5.4	$D_{pn}$ parameter of AR 11158 as a function of height . . . . .	111
5.5	$D_{pn}$ parameter of AR 11166 as a function of height . . . . .	113
5.6	$D_{pn}$ parameter of AR 11283 as a function of height . . . . .	114
5.7	Identified $\delta$ -spots of AR 11158, 11166 and AR 11283 . . . . .	118
5.8	$WG_M$ analyses of the 1st $\delta$ -spot of the AR 11158 in the photosphere	119
5.9	$WG_M$ analyses of the 2nd $\delta$ -spot of the AR 11158 in the photo- sphere . . . . .	120
5.10	$WG_M$ analyses of the 2nd $\delta$ -spot of the AR 11158 at the optimum height . . . . .	121
5.11	$WG_M$ analyses of the $\delta$ -spot of the AR 11166 in the photosphere	122
5.12	$WG_M$ analyses of the $\delta$ -spot of the AR 11166 at the first optimum height . . . . .	123
5.13	$WG_M$ analyses of the $\delta$ -spot of the AR 11166 at the second op- timum height . . . . .	124
5.14	$WG_M$ analyses of the $\delta$ -spot of the AR 11283 in the photosphere	125
5.15	$WG_M$ analyses of the $\delta$ -spot of the AR 11283 in the photosphere	126
5.16	$WG_M$ analyses of the $\delta$ -spot of the AR 11283 at optimum height	127
5.17	Comparison analyses of PF and NLFFF extrapolations . . . . .	130
5.18	PF analyses of 13 ARs . . . . .	131

# List of Tables

1.1	Mount Wilson sunspot groups classification system . . . . .	9
1.2	Summary of basic flare/CME models . . . . .	22
1.3	H $\alpha$ flare classification . . . . .	27
1.4	GOES flare classification . . . . .	28
3.1	Data summary of the 5 AR examples for the different flare classes	77
4.1	Summary of the relevant data for the four flares . . . . .	88
4.2	Summary of the optimum heights of the flares . . . . .	100
5.1	Ascertainment of the two flare precursors ( $WG_M$ and $D_{pn}$ ) of AR 11158, 11166 and AR 11283 . . . . .	116
5.2	Comparison analyses of the PF and NLFFF in AR 11158, 11166 and AR 11283 cases . . . . .	117
5.3	PF analyses in 13 ARs . . . . .	132
A.1	List of the investigated ARs in 1997 . . . . .	142
A.2	List of the investigated AR in 1998 . . . . .	142
A.3	List of the investigated ARs in 1999 . . . . .	143
A.4	List of the investigated ARs in 2000 . . . . .	143
A.5	List of the investigated ARs in 2001 . . . . .	144
A.6	List of the investigated ARs in 2002 . . . . .	144

A.7	List of the investigated ARs in 2003 . . . . .	145
A.8	List of the investigated ARs in 2004 . . . . .	145
A.9	List of the investigated ARs in 2005 . . . . .	145
A.10	List of the investigated ARs in 2006 . . . . .	145
A.11	List of the investigated ARs in 2010 . . . . .	146
A.12	List of the investigated ARs in 2011 . . . . .	147
A.13	List of the investigated ARs in 2012 . . . . .	148
A.14	List of the investigated ARs in 2013 . . . . .	148
A.15	List of the investigated ARs in 2014 . . . . .	149
A.16	List of the investigated ARs in 3D . . . . .	150

# Chapter 1

## Introduction

### 1.1 The Sun

If we compare the Sun with the other stars in the Universe, then we can say that the Sun is not unique in this context. It is a standard, medium-sized “ball of gas” already half way through its lifetime. However, the Sun is very important for us. Our star is at the centre of the Solar System and provides energy for the Earth. Furthermore, studying the Sun with its proxy offers researchers a unique insight into stellar structures and astrophysical plasmas.

The Sun contains 99.8% of the mass of our entire solar system, and it is nearly all in plasma state. About 70% of our star consists of hydrogen, while the rest is mostly helium, with much smaller quantities of heavier elements, such as oxygen, iron, magnesium and silicon. Every second,  $4.26 \cdot 10^9$  kg of the Sun’s mass is converted into energy by nuclear fusion reactions taking place inside the solar core. At the Sun’s equator, the rotation period is approximately 26 days, and it increases with latitude to about 35 days near the poles. This feature is called the differential rotation and occurs due to the rotation of this gaseous plasma body. The solar plasma is held together by gravity, and gravitational forces create tremendous pressure and temperatures in the core. Encasing the core, the solar interior consists of three other layers, namely: the radiative zone, the tachocline, and the convective zone (see Fig. 1.1). The basic properties of each region are:

- Core: The solar core extends up to 0.25% of the radius of the Sun ( $R_{\odot}$ )

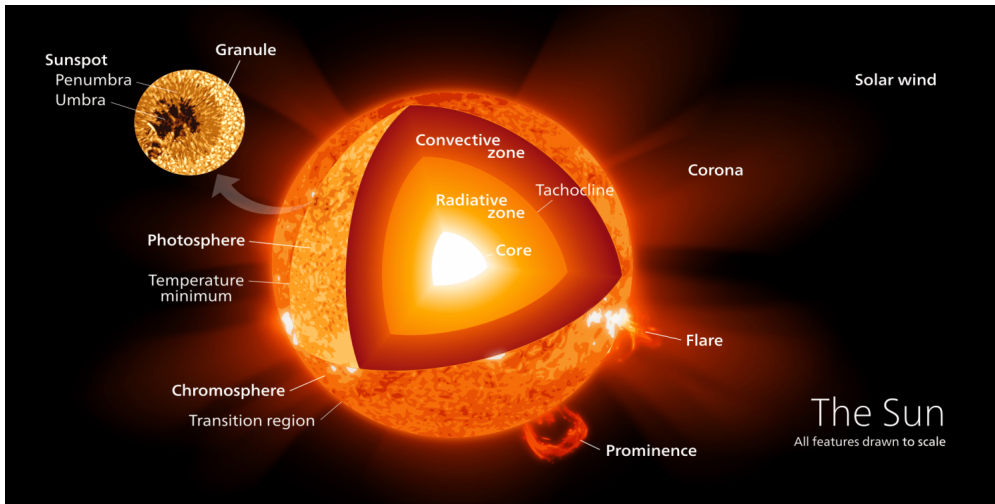


Figure 1.1: Cartoon view of the structure of the Sun. Credit:Wikipedia Commons/kelvinsong.

is 695 508 km). Here, the plasma is under massive pressure and is highly compact, therefore, the temperature reaches about 15.5 million K. The extreme temperature and pressure provide the conditions necessary for the nuclear fusion of hydrogen. Through quantum tunnelling, hydrogen nuclei are able to cross the Coulomb barrier, which allows fusion to occur enough to fundamentally power a total solar luminosity of  $3.8 \cdot 10^{33}$  ergs<sup>-1</sup>. Helium is produced by the fusion of hydrogen nuclei, through two basic avenues: the carbon-nitrogen-oxygen (CNO)-cycle, and, more importantly in the case of our Sun, the proton-proton (p-p) chain.

- Radiative zone: The radiative zone lies above the core from 0.25 to 0.75  $R_{\odot}$ . The  $\gamma$ -rays of the p-p chain continuously scatter in this high-density region when they meet free electrons, protons and atomic nuclei. The  $\gamma$ -rays are absorbed by atomic nuclei, therefore, the energy or particle motions do not increase in the plasma. The random travel through the radiative zone under this process means that protons from the core take on average about 1 million years to reach the surrounding convective zone.
- Tachocline: This is a 0.04  $R_{\odot}$  thin region between the radiative zone and the differentially rotating convective zone. The tachocline is where the solid body rotation mutates rapidly into differential rotation, which causes

the region to have a very large shear in velocity. The shearing process is the key to the so-called solar dynamo mechanism which generates the solar magnetic field. The differential rotation is the power that alters the poloidal magnetic field and enables it to become toroidal field.

- Convective zone: This most outer part of the solar interior starts from  $0.75 R_{\odot}$  and reaches all the way up to the surface, the latter known as the photosphere. The temperature drop enables the recombination process of electrons and ions. The absorption of photons heats up localised plasma elements and forms convective cells. The convective cells carry hot gas from the lower part of the convective zone (as deep as from the tachocline) to the photosphere, where it cools down. After the cooling, the material is transported back into the deeper layers, and the process starts again.

In the outer part of the Sun (the solar atmosphere), the first layer is the photosphere. There is a point where the transparency of the Sun changes from 100% down to 0%, where the surface becomes truly opaque, and the temperature decreases until a minimum is reached. Upwards from the photosphere it is easy to see the further distinct regions of the atmosphere, namely, the chromosphere, the transition region and the corona. Let us briefly discuss there atmospheric regions.

- Photosphere: This is the layer from which the majority of Sun's energy is radiated, in the form of light. The absorption lines in the solar spectrum help us to discover the diverse magnetic field topology of the photosphere in great detail. Due to the Zeeman splitting (see later in Sec. 2.1.1) of magnetically sensitive lines, measurements of the local magnetic field can be performed. We may distinguish quiet Sun, active Sun and the polar magnetic fields at the solar surface based on magnetic field measurements. The quiet Sun magnetic fields are ephemeral regions which rise with the convective flows. They are observed as an intra-granular network. The active regions (ARs) contain stronger and more compact magnetic field elements than quiet Sun magnetic fields. When the magnetic field strength of the AR is just a few hundred Gauss (G) then, it is called facule, but when the value reaches 1000-3000 G and it becomes spatially more extended (a few Mm), the area is termed a sunspot. The number and magnetic field strength of ARs follow the 11-year solar cycle (see later in Sec. 1.3). Solar physics researchers, including us, pay particular attention

to the magnetically complex solar ARs, because they are the source of the biggest eruptions of the Solar System (i.e. the source of flares and coronal mass ejections (CMEs)).

- **Chromosphere:** The temperature and the plasma density of the chromosphere vary substantially with height above the photosphere. At first, the temperature decreases with height - from about 6000 K at the photosphere to about 4000 K a couple hundred kms higher up. Strangely, temperatures begin to increase in the upper reaches of the chromosphere, rising up to a few tens of thousands K. The plasma density decreases approximately from  $2 \cdot 10^{-4} \text{ kg/m}^3$  to less than  $1.6 \cdot 10^{-11} \text{ kg/m}^3$ . The magnetic flux tubes, even in the ARs, rapidly expand with height as the ambient gas pressure drops. The chromosphere is normally hidden from our view, because it is drowned out by the brightness of the underlying photosphere. The chromospheric features are mostly examined in the  $H\alpha$  line which is a specific wavelength of red light (656 nm) emitted by hydrogen atoms in the Sun's atmosphere. Some other wavelengths of ultraviolet light also help us see into the chromosphere, especially into the hotter, higher sections near the transition region. Here, the main observed features are filaments and prominences that rise up through this area into the solar corona. Furthermore, most of the solar flares occur somewhere in the chromosphere.
- **Transition Region:** This is a highly dynamic part of the solar atmosphere. It is an extremely thin layer (in solar term) serving as the border between the chromosphere and the solar corona. Here, the temperature grows very quickly from a few tens of thousands to about two million K.
- **Corona:** The corona is the outer part of the solar atmosphere. During total solar eclipses, it is seen as a white crown surrounding the Sun. Furthermore, we can investigate the corona with a special instrument called the coronagraph that allows us to view the corona at all times, not only at an eclipse. The overall shape of the corona changes with the solar cycle. Coronal features include a large variety of magnetic structures, such as e.g. coronal loops, streamers, plumes and corona holes. Primarily electrons, protons and alpha particles that escape from the Sun's powerful gravity and stream out from the corona along the magnetic field lines extending into interstellar space make up the solar wind [Parker, 1958]. This stream

of energised, charged particles varies in density, temperature and speed over time, especially during impulsive flares and CME occurrences.

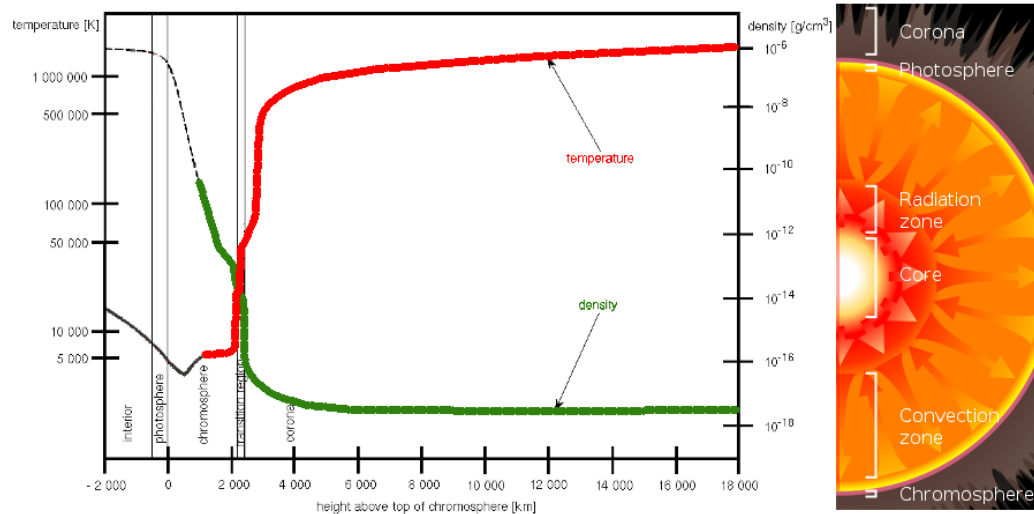


Figure 1.2: Temperature and density in the solar atmosphere. Credit: NASA

The 1D VAL atmospheric column model [Vernazza et al., 1981] is used to infer basic parameters of the solar atmospheric layers described above. Fig. 1.2 demonstrates that the characteristic height, temperature, number density, magnetic field and the dominance of gas pressure over magnetic pressure in the case of the quiet Sun is in good agreement with spectroscopic observations. Despite the fact that the solar atmosphere is much more complex and dynamic, the VAL atmospheric model has still been widely used for decades in various form.

## 1.2 Active Regions

The major solar eruptions originate from the magnetically strong ARs, which appear on the solar surface as sunspot groups, as we mentioned above in the paragraph discussing the photosphere. One of the important elements to be investigated in this work is the ARs. Originally, the convective cells and the tachocline are the cradle of the ARs. The 11-year and the associated 22-year solar cycle are strongly influenced by the combination of convective currents,

which bring the charged plasma from the deep to the photosphere and cause the differential rotation of the convection zone. The continuous strong shearing builds up the magnetic field in the azimuthal direction. The magnetic pressure associated with these azimuthal field lines ( $B^2/8\pi$ ) forces out the infused plasma ( $p_i$ ) in order to maintain a pressure balance with the surrounding plasma ( $p_0$ ):

$$p_i + \frac{B^2}{8\pi} = p_0. \quad (1.1)$$

The absence of plasma gives rise to buoyancy force within the field-lines [Abbett and Fisher, 2003]. The rising flux tubes interact with the turbulent convective flows and make a tangled,  $\Omega$ -shaped structure of magnetic field lines, forming an AR, visible above the photosphere. The magnetic field is pushed around by fluid motions at the photosphere continuously, because the gas pressure exceeds the magnetic pressure in this highly dynamic granular environment.

Sunspots are observed to be depressed compared to the brightness of the surrounding plasma [see a review by van Driel-Gesztelyi and Green, 2015]; this is known as the Wilson depression [Loughhead and Bray, 1958]. Sunspots are made up of two distinct parts. The outer region is the brighter penumbra with a fibril structure, see Fig. 1.3. The dark central part of the sunspot is called the umbra. Umbrae are dark because they are cooler than the surrounding photosphere. A strong vertical field (1000-4000 G) rises from the umbra, while in the outer penumbra, the horizontal component of the field dominates. The strong and highly vertical fields inhibit convective cells from replenishing the area with hot plasma from the deep convection zone. Evershed [1909] observed an outward flow from umbrae through the penumbrae which advects heat away [Schlichenmaier and Solanki, 2003]. Furthermore, a downflow was found within umbrae, below the surface [Duvall et al., 1996]. In addition to this, outside of penumbra boundaries, a further moat outflow creates a small ring where line-of-sight (LOS) magnetic field is weak [Brickhouse and Labonte, 1988]. This flow also advects the heat from convective cells, away from penumbrae [Fox et al., 1991]. Convective upflows encounter and are forced outward by the mostly horizontal field lines of penumbrae. The outflow cools and flows down when the plasma is pulled inward (toward the sunspot) to maintain pressure balance [Hindman et al., 2009].

When the AR appears, it has a leading and a trailing part, which have opposite polarities on the northern and southern hemispheres. This is known

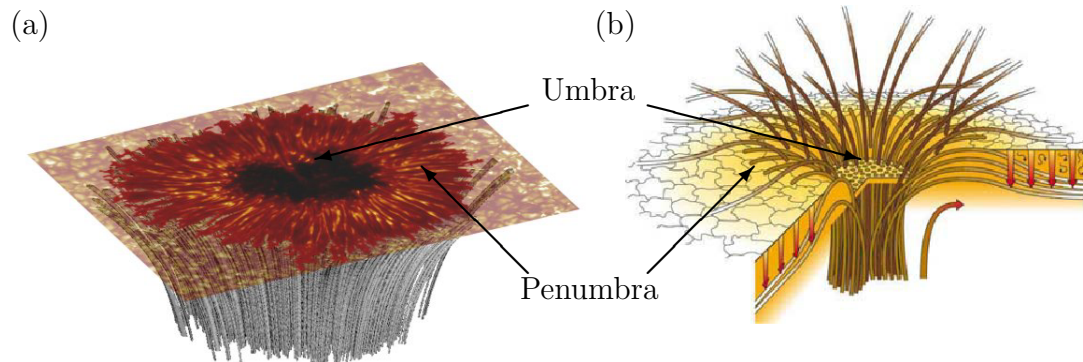


Figure 1.3: The 3-dimensional structure of a sunspot: (a) Swedish Solar Telescope (SST) observation combined with a sketch of the inferred 3D structure (schematic) underneath the spot. Credit: MPA - Max-Planck-Gesellschaft. (b) An artistic visualisation of the magnetic structure in a sunspot [Thomas and Weiss, 2004]. Some of the penumbral flux ends up in a shallow canopy above the solar surface. The vertical arrows illustrate the Evershed flows that pump downwards by the small-scale granular convection cells (small black arrows are between vertical arrows). The curved arrow shows the large-scale outflows in the moat cell that surrounds the spot.

as Hale's law [Hale et al., 1919]. The line connecting the centroids of the leading and following polarities is inclined towards the equator (Joy's Law) and the inclination decreases with emergence latitude [Howard, 1991]. At the photospheric interface, the magnetic dipole structure actually is the part of the flux rope that is rising from the interior and the other part entering (the Sun) again. As one cycle draws to the end and the new one begins, the polarity of the leading spot in both hemispheres is observed to change.

The sunspots appear at about  $40^\circ$  latitude at the beginning of the solar cycle, and this latitude of emergence gradually migrates towards the equator during 11 years, the length of the cycle. Additionally, when the sunspot cycle is close to the maximum, then the polar field cycle is at its minimum phase and vice versa. The leading polarity of the sunspot group is opposite with the polar field in each hemisphere. Also, it has been observationally proven that the decaying leading magnetic polarity of the sunspot group migrates along the meridional lines to the pole, and the following polarity to the equator. This process reduces the strength and eventually flips the polarity of the polar field

over the solar cycle. An explanation of the solar cycle was first put forth in 1961 by the American astronomer Horace Babcock, and it is now known as the Babcock Model [Babcock, 1953] (see Fig.1.4).

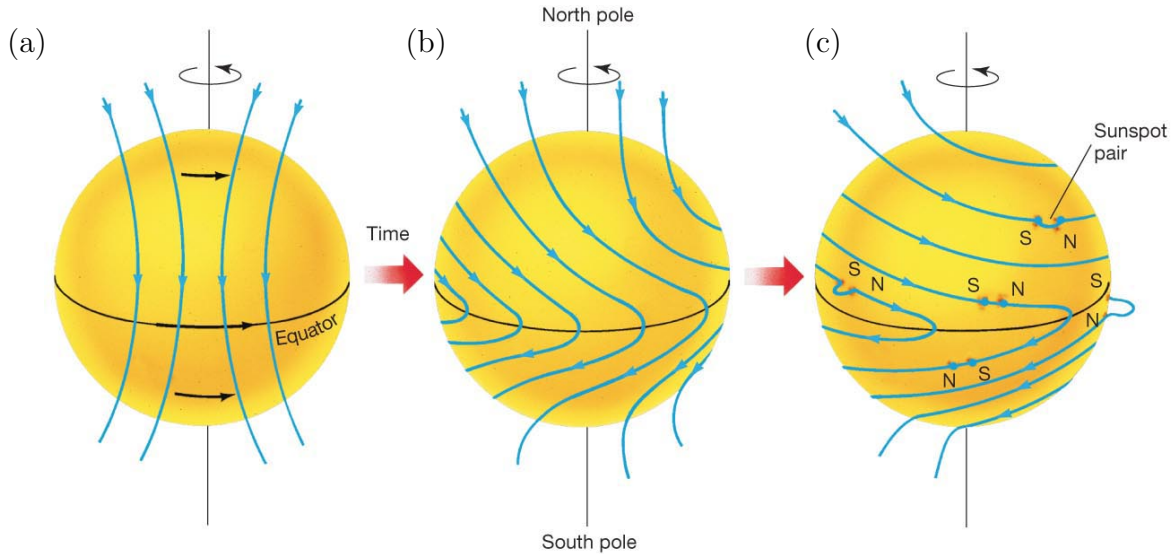


Figure 1.4: Schematic of solar flux-transport dynamo processes according to the Babcock Model [Babcock, 1953]. (a) Shearing of poloidal field by the Sun's differential rotation. (b) Toroidal field produced due to shearing by differential rotation. (c) When the toroidal field is strong enough, buoyant loops rise to the surface and sunspots are visible in the photosphere. Credit: Pearson Education (2014)

Sunspot groups are traditionally classified using the Mount Wilson and McIntosh classification systems [Hale et al., 1919, McIntosh, 1990]. These two main classification methods are currently applied to all sunspots by eye. The Mount Wilson sunspot group classification system was introduced in 1919 based on the configuration and characteristics of the positive and negative polarities. Each group is labelled with a combination of designations (i.e. unipolar ( $\alpha$ ), bipolar ( $\beta$ ) or multipolar ( $\gamma$  or  $\delta$ )) nature of the sunspots, see Table 1.1. The McIntosh method is a three-component classification system, taking the form Zpc. The first (Z) component is the modified Zürich sunspot classification, the second one (p) classifies the largest spot, and the last digit (c) shows the degree of spottiness in the interior of the AR. Accordingly, the three-component

classification system has 60 distinct types of sunspot groups, as source, shown are in Figure 1.5.

Classification	Description
$\alpha$	Unipolar AR.
$\beta$	Bipolar AR with a clear division between two opposite polarities.
$\gamma$	Several smaller opposite polarities distributed in bipolar AR.
$\delta$	AR has the two opposite polarity umbrae within one penumbra.

Table 1.1: Mount Wilson sunspot groups classification system.

When becoming closer to the solar maximum, then the magnetically complex sunspots ( $\delta$ -type) appear more frequently, and those serve as the source of powerful solar flare and CME eruptions. These eruptions, in turn, could affect our modern technology-based society in some very serious and damaging ways, therefore, we need to predict the intensive solar eruptions with high accuracy. The most current prediction techniques all connect in a different kind of way to the Mount Wilson and McIntosh classification systems. The methods try to find relationships between the extremely powerful solar events and some pre-defined observable proxies that measure the magnetic complexity of the host ARs.

### 1.3 3D magnetic field of solar ARs

The Mount Wilson and McIntosh classification systems are useful tools to identify the flare-producing ARs, but these classification systems do not provide yet accurate enough flare prediction. A reliable flare prediction method is still a challenging problem, which may be resolved if we concentrate on the pre-flare evolution of flare-producing ARs. The dynamics and evolution of flare and CME eruptions in the solar atmosphere is related to the (upper chromospheric and coronal) magnetic field of ARs, as in the upper chromosphere and corona, magnetic forces dominate. Nevertheless, detailed routine magnetic field measurements are only available in the photosphere, and the measurement of the upper chromospheric and coronal magnetic fields is one of the major difficulties in solar physics. The structure of tangled and  $\Omega$ -shaped magnetic field lines above the photosphere has been studied mostly by EUV observations [Aschwanden et al., 1999b], but the three-dimensional (3D) solar magnetic field of the ARs is still difficult to measure directly.

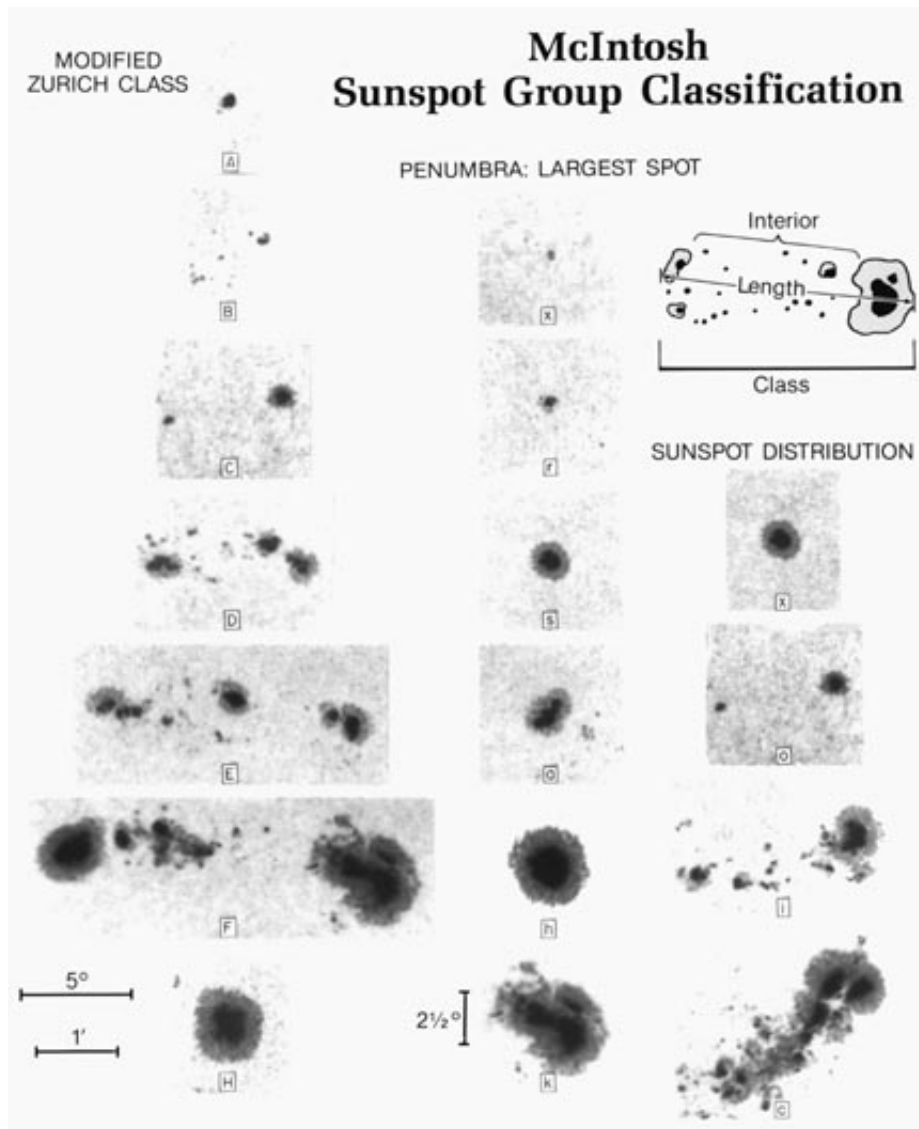


Figure 1.5: The three-component classification system known as the McIntosh method. Credit: <http://www.petermeadows.com/html/glossary.html>

Nowadays, we have to compute 3D magnetic field structures of the ARs, for which we use the measured photospheric magnetic field as boundary condition. The thermal conductivity is parallel to the field by large, therefore, the field lines become visible by emission at the corresponding temperature,

which allows us to test constructed and modelled magnetic field structures. The presence of constructed magnetic field could be in agreement with real coronal images, however, coronal field models simplify the true nature of the coronal magnetic field. The knowledge of the coronal magnetic field plays an important role in numerous problems, such as magnetic energy storage, magnetic instabilities, magnetic reconnection, and magnetic energy dissipation in solar flares and CMEs.

For performing a magnetic field reconstruction, we need to take into account the value of the plasma- $\beta$ . This parameter plays a fundamental role in the physics of the solar corona. The plasma- $\beta$  is a dimensionless number quantifying the ratio of the kinetic plasma pressure and the magnetic pressure:

$$\beta = 2\mu_0 \frac{p}{B^2}. \quad (1.2)$$

The plasma- $\beta$  changes with height in the solar atmosphere. When  $\beta \ll 1$ , then the magnetic pressure dominates over the kinetic pressure.

Force-free-field (FFF) modelling is able to reconstruct the invisible magnetic structure from photosphere to the corona using measurements of the surface magnetic field [Wiegmann and Sakurai, 2012]. The FFF reconstruction gives a good first-insight information about the energy, structure, morphology and topology of the magnetic field. The FFF can be derived from the equation of motion. The left-hand side of the equation of motion vanishes when the flow speed is much smaller than the sound speed, Alfvén speed and the gravitational free-fall speed for the vertical scale-length. The result is a magnetohydrostatic balance between the pressure gradient, the Lorentz force and the gravitational force.

$$0 = -\nabla p + \mathbf{j} \times \mathbf{B} - \rho g \hat{z}. \quad (1.3)$$

The gravitational force is negligible when the height of the structure is much less than the pressure scale height. The Lorentz force is:

$$\mathbf{j} \times \mathbf{B} = \mathbf{0}. \quad (1.4)$$

If the Lorentz force is equal to 0, then the magnetic field satisfies the force-free condition. The Lorentz force is not allowed under force-free conditions, because the pressure gradient and the gravitational forces would not be strong enough

to balancing it. We can conclude that inside a magnetic structures the magnetic field keeps force-balance by itself. When the electric current density vanishes everywhere, i.e.

$$\mathbf{j} = \frac{1}{\mu_0} \nabla \times \mathbf{B} = 0, \quad (1.5)$$

and the magnetic field can be written as a gradient of the scalar potential:

$$\mathbf{B} = \nabla \Phi, \quad (1.6)$$

then the solenoidal condition

$$\nabla \cdot \mathbf{B} = 0 \quad (1.7)$$

leads to the Laplacian of  $\Phi$  being

$$\nabla^2 \Phi = 0, \quad (1.8)$$

with the scalar potential solution  $\Phi$  given by

$$\Phi(x, y, z) = \frac{1}{2\pi} \int_{s'} \frac{\partial \Phi}{\partial n} \frac{1}{r} ds' = \frac{-1}{2\pi} \int_{s'} \frac{B_z(x', y', z' = 0)}{r} ds'. \quad (1.9)$$

Here,  $B_z = \frac{\partial \Phi}{\partial z}$  is the normal component of the field on the boundary  $s'$ , and

$$r = \sqrt{[(x - x')^2 + (y - y')^2 + (z - z')^2]}.$$

The components of the field are:

$$B_i = \frac{\partial \Phi(x, y, z)}{\partial x_i}, \quad (1.10)$$

where  $(x_1, x_2, x_3) = (x, y, z)$ , which is a consequence of the irrotational character of the current free field or potential field [Gary, 1989]. Furthermore, the field satisfies the magnetostatic equation:

$$\nabla \times \mathbf{B} = \alpha \cdot \mathbf{B}, \quad (1.11)$$

where  $\alpha$  is the *force-free parameter*. When  $\alpha=0$ , we recover the potential field (PF) case, which is the minimum energy solution,

$$(\nabla \times \mathbf{B})_x = 0, \quad (\nabla \times \mathbf{B})_y = 0, \quad (\nabla \times \mathbf{B})_z = 0, \quad \nabla \cdot \mathbf{B} = 0. \quad (1.12)$$

However, when  $\alpha$  is constant along a field line and also along the electric current lines, the constructed full magnetic field is called the *linear force-free field extrapolation model* (LFFF), e.g.

$$\begin{aligned} (\nabla \times \mathbf{B} - \alpha \mathbf{B})_x &= 0, & (\nabla \times \mathbf{B} - \alpha \mathbf{B})_y &= 0, & (\nabla \times \mathbf{B} - \alpha \mathbf{B})_z &= 0, \\ \nabla \cdot \mathbf{B} &= 0. \end{aligned} \quad (1.13)$$

Otherwise, when  $\alpha$  is non-constant, it is called a *non-linear force-free field extrapolation model* (NLFFF), described by

$$\begin{aligned} (\nabla \times \mathbf{B} - \alpha \mathbf{B})_x &= 0, & (\nabla \times \mathbf{B} - \alpha \mathbf{B})_y &= 0, & (\nabla \times \mathbf{B} - \alpha \mathbf{B})_z &= 0, \\ \nabla \cdot \mathbf{B} &= 0, & \nabla \alpha \cdot \mathbf{B} &= 0. \end{aligned} \quad (1.14)$$

An important point in the FFF extrapolation model is that the magnetic field energy is bounded from below by a PF, and at the upper boundary by the *Aly - Sturrock conjecture* [Aly, 1984, 1988].

The Aly-Sturrock conjecture states that the maximum magnetic energy is obtained when the magnetic field lines are fully open. This means that the lower boundary is a footpoint of the magnetic field on the Sun and the magnetic field lines reach up to infinity. If, on the other hand, the magnetic field is closed, then the magnetic loop contains electric currents, therefore, the energy is higher than that of associated with the PF, but lower than the open field [Aly, 1984, Yang et al., 1986, Sturrock, 1991]. This is an important result, as solar flares and CMEs derive their energy from electric currents that always flow along field lines. The vertical electric current density can be estimated from the measured photospheric magnetogram  $(B_{x0}, B_{y0})$ :

$$\mu j_{z0} = \frac{\partial B_{y0}}{\partial x} - \frac{\partial B_{x0}}{\partial y}, \quad (1.15)$$

and the force-free parameter can be calculated as

$$\alpha(x, y) = \mu_0 \frac{j_{z0}}{B_{z0}}. \quad (1.16)$$

Before we perform magnetic field extrapolation, we need to think about which approach is the most suitable model for our study. The PF condition is an instrument used by many computer extrapolation models because of the mathematical simplicity. This approach is very useful if we would like to reconstruct the 3D form of e.g. a coronal loop, the strength of the coronal magnetic field, or the global topology of the magnetic field. But, if we would like to calculate the free-energy of an AR, then we need to use at least one of the more complex FFF approaches. The LFFF is a simple, fast, and elegant method, but it requires the knowledge of the three components of the field at the photosphere. The LFFF model also has some difficulties. For example, the LFFF cannot be continued in a physically realistic manner to large distances, because the magnetic field decays so slowly that the magnetic energy diverges.

Next, the main problem which the NLFFF approach is that no widely accepted solution exists, but the literature distinguishes two different types of popular NLFFF codes [Aschwanden, 2016]. The first one is the traditional NLFFF code, which uses the 3D vector field from a vector magnetograph as input for the photospheric boundary. The second type uses only a LOS magnetogram to constrain the PF, while the forward-fitting of an analytical approximation of the NLFFF solution in terms of vertical currents to coronal field coordinates is carried out in order to determine the  $\alpha$  parameter. The truth is, we do not know yet which extrapolation model yields the picture to be closest to reality. To demonstrate this, let us take a closer look at Fig. 1.6a-d. There, we are not fully sure whether the PF or the NLFFF extrapolation is more similar to the AIA 171 Å observation outlining the magnetic field lines at coronal temperatures.

To process with the coronal field extrapolation by means of PF, LFFF or NLFFF we use two main techniques. One is the *Green's function* [Schmidt, 1964], and another one is *Fourier expansion* [Alissandrakis, 1981]. The Green's function method is to place monopoles at  $(x', y', 0)$  with a magnetic flux  $B_n dx' dy'$  at the lower boundary. The magnetic potential at  $(x, y, z)$  due to the normal magnetic field  $B_n(x', y')$  on  $z = 0$  is

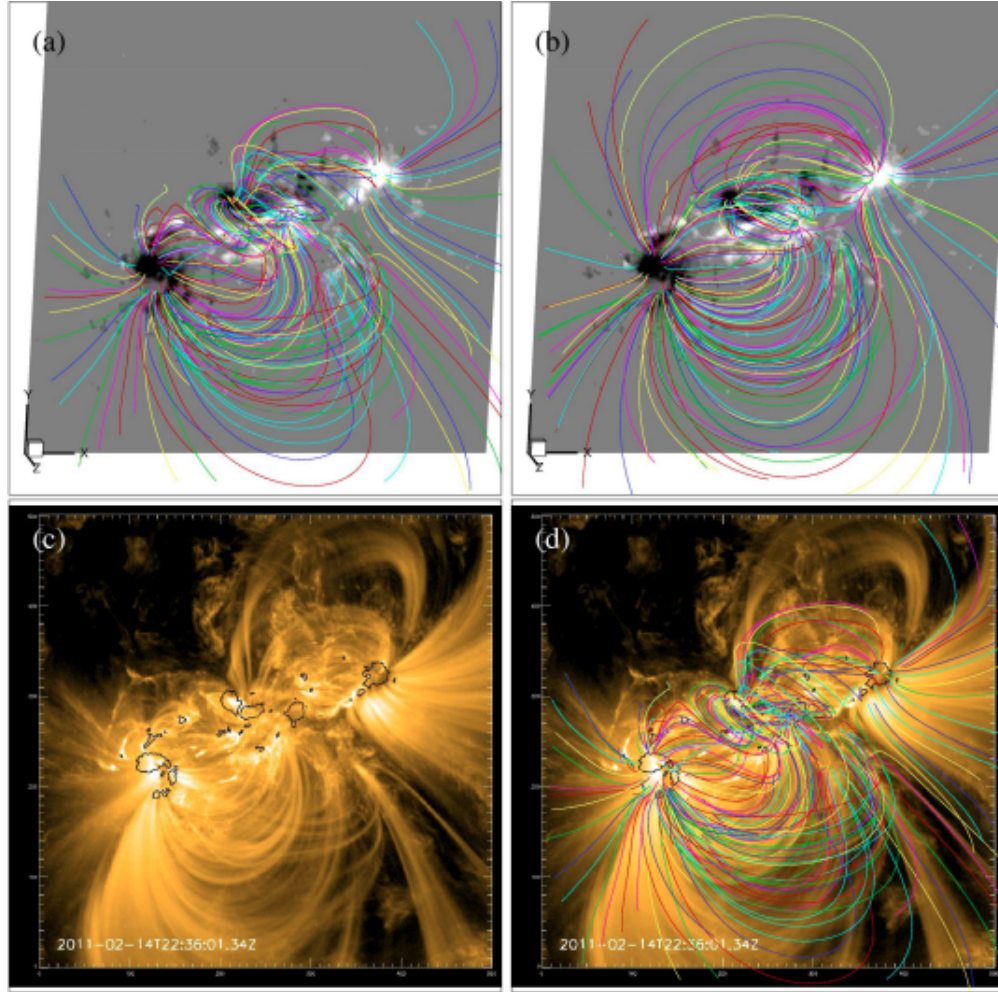


Figure 1.6: Comparison of extrapolated field lines with AIA 171 Å coronal loops for AR 11158: (a) the NLFFF extrapolation, (b) the PF extrapolation, (c) the AIA 171 Å image and (d) field lines of NLFFF extrapolation overlaying the AIA image. The black contour lines indicate the  $\pm 1000$  G of LOS photospheric field [Fig. 5 of Jiang and Feng, 2013].

$$\psi(x, y, z) = \int B_n(x', y') G_n(x, y, z, x', y') dx' dy', \quad (1.17)$$

$$G_n(x, y, z, x', y') = \frac{-1}{\phi |\mathbf{r} - \mathbf{r}'|} \quad (1.18)$$

where  $|\mathbf{r} - \mathbf{r}'|$  is the distance from  $(x, y, z)$  to  $(x', y', 0)$ , and  $G_n$  is the Green's function.

The Fourier method expands the boundary value in Fourier components over the corresponding values of  $k_x, k_y$ , namely,

$$B_n(x, y) = B_0 + \sum_k B_k e^{ik_x x + ik_y y}. \quad (1.19)$$

The Fourier solution is written as

$$\psi(x, y, z) = B_0 z - \sum_k \frac{B_k}{k} e^{ik_x x + ik_y y - kz}. \quad (1.20)$$

The Fourier expansion is a much faster computational method than the Green's function, therefore, the Fourier procedure is a popular magnetic field extrapolation technique.

## 1.4 Energy Build-up before Flares and CMEs

Whichever way we choose to reconstruct the 3D skeleton of the magnetic mapping of flaring ARs, this could help us better understand the magnetic build-up before the flare and CME eruptions. Flare and CME evolution basically starts when new magnetic flux is pushed up through the solar surface and an AR is born. The emerging magnetic flux carries magnetic energy from the solar interior to the atmosphere. The differential rotation causes stretching this emerging field in a torus shape. Swirling motions of a convective plasma in helical turbulence lead to a locally stressed and twisted shape of magnetic flux tubes. Since the triggering mechanism for flux emergence is buoyancy, allowing the twisted magnetic flux tube to rise towards the solar surface, it is generally accepted that a minimum twist is necessary for flux tubes to conserve their integrity [Emonet and Moreno-Insertis, 1998, Cheung et al., 2006, Fan, 2008]. The buoyancy instability takes place in the mechanical equilibrium with the environment of flux tubes, inside which the magnetic pressure is large, but the plasma density is low [Zwaan, 1985].

The level of twist in the emerging flux is quantified by the magnetic helicity, defined as

$$H_M(t) = \int_{z \geq 0} \mathbf{A}(t) \cdot \mathbf{B}(t) dV. \quad (1.21)$$

Here,  $\mathbf{B}$  is the magnetic field, and  $\mathbf{A}$  is the vector potential for  $\mathbf{B}$ . We can consider the sheared, twisted flux tubes, and derive the connection between the magnetic helicity and the  $\alpha$  parameter. If the magnetic energy is minimised with a specified value of  $H_M$ , then we obtain the LFFF. At first, the LFFF could be a minimum energy state, but later, it will be unstable. Next, if the magnetic energy is minimised by fixing the connectivity of the magnetic structure, then we obtain the NLFFF, which might be dynamically stable or unstable. We can conclude that  $\alpha$  is uniquely related to the number of twists, which is a measure of helicity.  $H_M$  is conserved for the LFFF of an expanding flux tube.

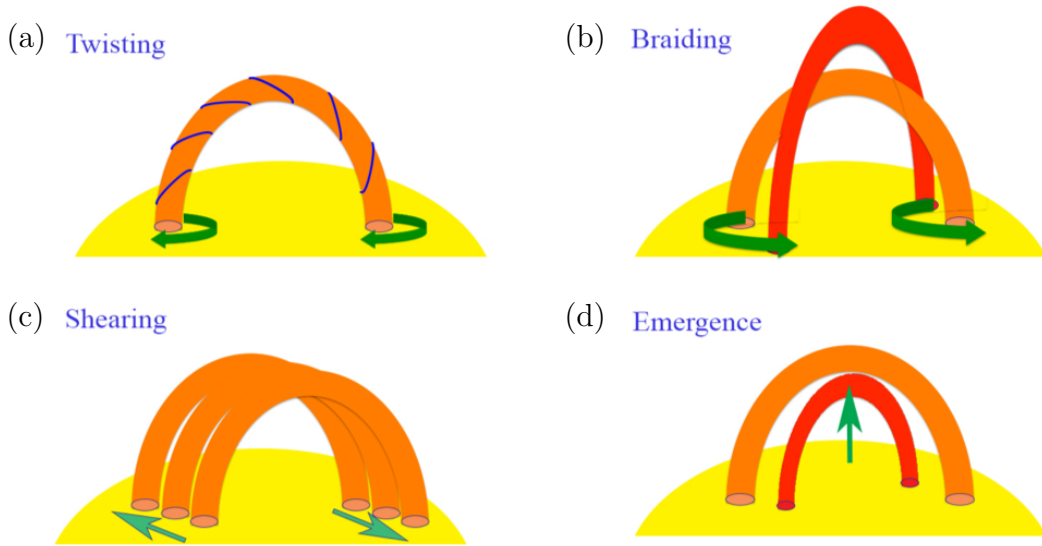


Figure 1.7: The upper chromospheric/coronal magnetic field lines become shuffled by (a) twisted, (b) braiding, (c) shearing or (d) new emerging magnetic flux and the build-up of free magnetic energy of the system.

The NLFFF state of an AR can become unstable due to efficient driver mechanisms that generate the geometry favourable for the release of free-energy from the system, see Fig. 1.7. One such driver could be the twisting or shearing motion of the two opposite polarity magnetic fields along the polarity inversion line (PIL). Alternately, new emerging magnetic flux may be pushed towards the

pre-existing flux, and result in the favourable geometry for the energy release. An additional possibility is that, two magnetic field lines start braiding with each other, and, at some point the AR becomes unstable.

## 1.5 Energy Release - Magnetic Reconnection

When the favourable geometry for the energy release arises, then flare and/or CME occurrences are irreversible. The phenomenon of the free-energy release is called the magnetic reconnection [Parker, 1979, Kulsrud, 1998, Biskamp, 2000, Priest and Forbes, 2000]. Magnetic reconnection is the name given to the magnetic topology change of a set of field lines, which guides them to a new equilibrium configuration with lower magnetic energy. Reconnection is a small-scale phenomenon that is generated in some region, such that there the constraint of ideal dynamics is broken. The cause of the magnetic reconnection effect is found in Ohmic dissipation of electric current, which takes place in current sheets (regions where an intensive electric current flows). Sweet [1958] suggested that places where the magnetic field vanishes, namely, at null-points, e.g. X-points, are potential weak spots in the sense that current sheets tend to be formed at them. During this process, magnetic energy is converted into kinetic energy, thermal energy, and particle acceleration.

The formal description of reconnection requires the modelling framework of resistive magnetohydrodynamics (MHD). In this case, the fluid may move separately from the field, and the field lines can slip across the fluid. In resistive MHD, Faraday's, Ampère's and Ohm's laws may be combined to obtain four basic equations detailed below, which describe plasma and magnetic field evolution. They are:

Conservation of mass:

$$\frac{\partial \varrho}{\partial t} = -\nabla \cdot (\varrho \mathbf{v}), \quad (1.22)$$

where  $\varrho(\mathbf{r}, t)$  is density and  $\mathbf{v}(\mathbf{r}, t)$  is velocity;

Conservation of momentum:

$$\varrho \left( \frac{\partial}{\partial t} + \mathbf{v} \cdot \nabla \right) \mathbf{v} = -\nabla p + \varrho \cdot \mathbf{g} + \frac{1}{\mu_0} (\nabla \times \mathbf{B}) \times \mathbf{B}. \quad (1.23)$$

Here,  $p(\mathbf{r}, t)$  is pressure;  $\mathbf{g}(\mathbf{r}, t)$  is gravitational acceleration;  $\mathbf{B}(\mathbf{r}, t)$  is magnetic field and  $\mu_0$  is a magnetic permeability of free space;

Conservation of entropy:

$$\left(\frac{\partial}{\partial t} + \mathbf{v} \cdot \nabla\right)p = -\gamma p \nabla \cdot \mathbf{v} + (\gamma - 1) \frac{\eta}{\mu_0^2} (\nabla \times \mathbf{B})^2, \quad (1.24)$$

where  $\eta$  is magnetic diffusivity and  $\gamma$  is normally taken as 5/3; and

Conservation of magnetic flux:

$$\frac{\partial \mathbf{B}}{\partial t} = \nabla \times (\mathbf{v} \times \mathbf{B}) - \frac{1}{\mu_0} \nabla \times (\eta \nabla \times \mathbf{B}), \quad (1.25)$$

$$\nabla \cdot \mathbf{B} = 0. \quad (1.26)$$

where  $\eta/\mu_0$  (m/s<sup>2</sup>) is the diffusion coefficient, which determines the diffusion of the magnetic field. When  $\eta=0$ , then the ideal MHD equations are obtained from Eqs. (1.22) - (1.26). The ratio of the resistive and ideal MHD time scales is called the Lundquist number:

$$S = \frac{\tau_r}{\tau_A} = \mu_0 \frac{L v_A}{\eta}, \quad (1.27)$$

where  $v_A$  is the Alfvén velocity.  $\tau_r$  and  $\tau_A$  are the characteristic time scales for the diffusive/ideal structures with length scale  $L$ . Alternatively, we also use the magnetic Reynolds number,

$$R_m = \mu_0 \frac{L v}{\eta}. \quad (1.28)$$

Here, the Alfvén speed is replaced by a typical plasma velocity  $v$ , and  $L$  is a characteristic length. The magnetic Reynolds number is relevant in turbulence problems that are flow-dominated. The Lundquist number is significant in resistive instabilities. The ratio of these two numbers gives the Alfvén Mach number, which determines the reconnection rate:

$$\frac{R_m}{S} = \frac{v}{v_A} = M_A. \quad (1.29)$$

The reconnection time in a current sheet of length  $L$  is

$$t_{rec} = \frac{L}{v} = \frac{t_A}{M_A}, \quad (1.30)$$

where  $t_A$  is the Alfvén transit time. The value of  $t_A$  is from 10 to 100 s if we estimate the length of e.g. a coronal magnetic structure as  $10^4$ - $10^5$  km. In the literature, two basic 2D reconnection models are widely known: the Sweet-Parker and the Petschek model. Fig. 1.8a-b demonstrates these two basic 2D reconnection models, where the diffusion region is the grey area, and the opposite field lines are illustrated with red and blue colours.

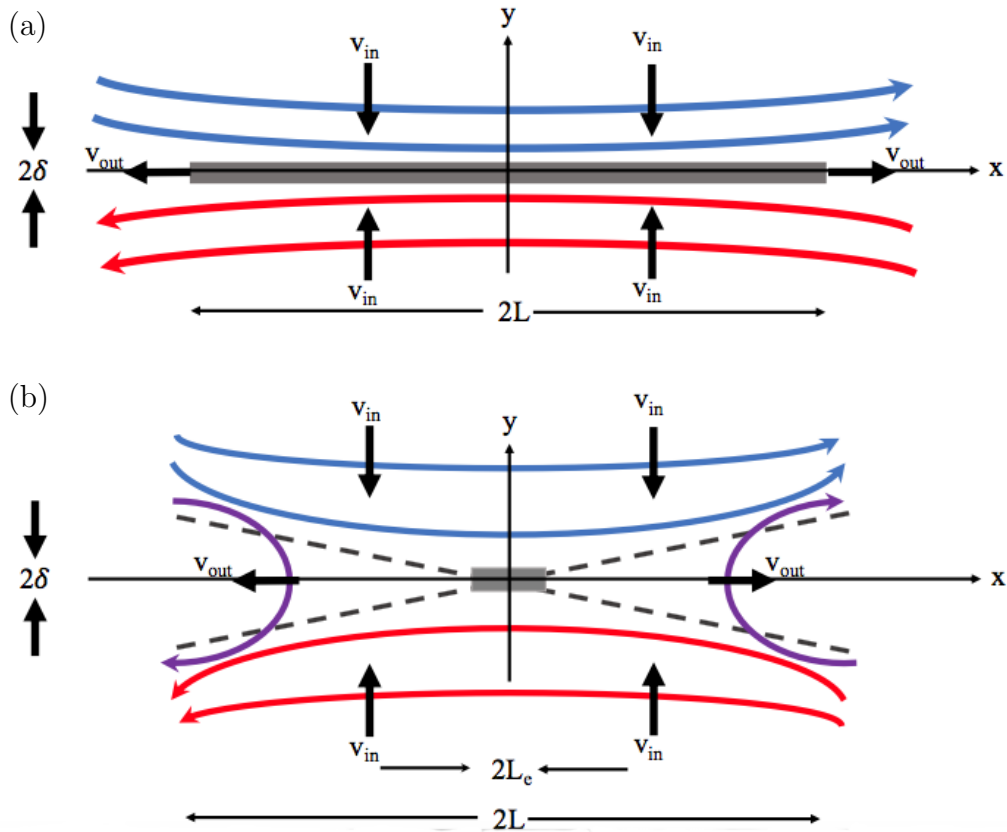


Figure 1.8: (a) Sweet-Parker reconnection model; (b) Petschek reconnection model.

## 1. Sweet-Parker model

In Fig 1.8a, Sweet and Parker determined [Sweet, 1958, Parker, 1957] the speed with which field lines are carried into a steady diffusion region of length  $2L$  and width  $2\delta$ . The reconnection rate from this model is given by

$$M_A \simeq R_m^{-1/2}. \quad (1.31)$$

In the corona, if we calculate the reconnection time using  $R_m = 10^{14}$  and  $M_A \sim 10^{-7}$  then  $t_{rec} \sim 10^8 - 10^9$  s. This reconnection time is much longer than the typical value of  $t_{rec}$  for flares. Later, Parker [1963] claimed that this model cannot explain the rapid energy release in a flare.

## 2. Petschek model

Petschek [1964] suggested that the Sweet-Parker diffusion region is limited to a small segment (of length  $L \ll L_e$ ) of the boundary between opposing magnetic fields (see Fig. 1.8b). The diffusion region is thinner, and so reconnection can take place faster. Petschek realised that a slow-mode shock (purple lines) provides another way of converting magnetic energy into heat and kinetic energy. He suggested that shocks would stand in the flow when a steady state is reached. In this model, the reconnection rate is given by

$$M_A \simeq \frac{\pi}{8 \ln R_m}. \quad (1.32)$$

The value of the  $M_A$  is between 0.01 and 0.1 in the corona. The Petschek model provides a time scale similar to that of flare occurrences. Forbes and Priest [1987] extended this investigation, and they found that the magnetic reconnection speed is controlled by the spatial pattern of flow in the inflow region. The model put forward by Forbes and Priest [1987] is very similar to the Petschek model, because the inflow causes a flux pileup around the diffusion region.

Our understanding of magnetic reconnection is still limited. Our current knowledge comes from theoretical studies, computer models, and laboratory experiments. These all support the basic Petschek model and most of the solar eruption models are based on this simple but powerful approach.

## 1.6 Standard solar flare and CME occurrence model

The magnetic reconnection process for the energy release during flares and CMEs has been widely adopted by many theories. These theories also have been put forward to account for the initial conditions of solar flare and CME occurrence. Based on Aschwanden [2005], we can categorise the basic flare and CME models according to their driver mechanisms and dimensionality of the magnetic reconnection geometry listed in Table 1.2. The basic models are separated by the locations of the drivers: above and below the flare site. Above the flare site, drivers could be rising filaments or a prominence. Drivers below the flare site, i.e. in the photosphere, can be flux emergence, converging flows and shear flows closer to the PIL.

Driving mechanism	2D model	3D model
Rising filament or prominence	X-type reconnection Hirayama [1974] Kopp and Pneuman [1976]	
Photospheric flux emergence	Emerging flux model Heyvaerts et al. [1977]	Quadropolar flux transfer Melrose [1995]
Photospheric converging flows	Equilibrium loss model Forbes and Priest [1995] Quadrupolar double-arcade Uchida [1980]	
Photospheric shear motions		Magnetic breakout Sturrock [1966] Tether-cutting model Antiochos et al. [1999] Shearing motions to create current sheets Somov et al. [1998]

Table 1.2: Summary of basic flare/CME models according to the driver mechanisms and dimensionality. Credits: [Table 10.1 of Aschwanden, 2005]

Table 1.2 is not a complete list of flare and CME models, but multiple scenarios out of them could lead to a relatively useful flare and CME model, like the well-known CSHKP model (see Fig. 1.9a). The 2D CSHKP model is, at the moment of writing, the most widely accepted standard flare description because this model capture well a lot of observational features found in hard and soft



Mikic and Linker, 1994]. The current sheet is typically located between the anti-parallel field lines providing ideal circumstances for magnetic reconnection below the rising filament. The constantly rising filament stretches the current sheet above the PIL. In the stretched current sheet the field lines become close to each other, and potential weak X-point starts to form. In the X-point, magnetic flux is lost from the structure on the inflow sides, and the new structure, built up by the reconnection, finally, grows on the outflow sides. Magnetic reconnection taps into the stored energy of the magnetic field, converting it into heat and kinetic energy that sends particles streaming out along the field lines. The heated plasma, together with the newly formed magnetic field line creates a pair of slow and fast shocks above and below the reconnection site. The hot plasma becomes subtended in the loop from the chromosphere to the corona.

Below the reconnection site, the new field lines with the heated plasma occupy the denser soft X-ray flare loops which are filled with chromospheric evaporated plasma and newly reconnected relaxing field lines. The fast shocks in the reconnection outflow collide with the previously reconnected field lines and produce hot thermal hard X-ray sources above the flare loops. The particles race along the field lines and interact with the chromosphere, also causing the evaporation up-flows of the plasma. Post-flare loops are formed over the PIL and slowly cool down by radiation. The reconnection region keeps continually rising, reaching magnetic field line even further from the magnetic inversion line, so more field lines reconnect and form new post-flare loops above the newly created hotter ones. A new arcade includes both the older cooler loops, and above, new hotter loops. Above the reconnection site, the reconnection outflows propagate upward, and bright flare loops are visible in soft X-ray and EUV wavelengths.

During flare occurrences, we can observe the cooler loop in the  $H\alpha$  line, while the hotter loops are seen in soft X-ray. Neupert [1968] noted that the cumulative time integral of the soft and hard X-ray flux are the same, therefore, the source of hard X-rays ( $< 25$  keV) are foot-points of the loop, which are also emitting soft X-rays. Masuda et al. [1994] investigated that soft X-ray loops are underneath and found the coronal hard X-ray source on the top of coronal loops. The coronal hard X-ray is softer than the foot-point's hard X-ray, because the bremsstrahlung emission suggests that accelerated particles lose kinetic energy closer to chromosphere. When the high-energy particles are trapped, they produce intensive emissions in the radio band.

The flare process traditionally is divided into three phases: (i) The pre-flare phase is when the flare trigger is leading to the major energy release. It shows a slow increase of soft X-ray flux. (ii) The impulsive phase is the main energy release phase. The soft X-ray flux rises rapidly during this phase, and the hard X-ray,  $\gamma$ -ray, and radio microwave emissions also appear. (iii) In the gradual phase, we cannot observe further emission in hard X-ray and the soft X-ray flux begins to decrease gradually.

The filament or CME from the inner part of the AR lifts off slowly, and the flux rope is stretched upward. This imposes an ever stronger magnetic tension force hindering the flux rope from further ascension. At some point, the flux rope then breaks away from the surface and moves into the interplanetary space. The outward motion of the magnetic flux form coronal streamers, which expand like balloon-shaped bursts released into the solar wind. They contain a billion tons of matter threaded with magnetic field lines. Electrons, protons, and heavy nuclei are accelerated along the magnetic field lines to near the speed of light, which is much faster than the solar wind can flow.

The CME/filament eruption has a classic three-part structure, which consists of a bright front, a cavity, and a core (Fig. 1.9b). The bright front is a shell of dense coronal plasma bounding a darker region, and it has been interpreted as material swept up by the erupting flux rope. The darker region is formed due to the presence of a flux rope. The innermost bright feature, the so-called core is also seen to be emitting in the  $H\alpha$  line of neutral hydrogen, indicating the presence of much cooler plasma. However, when a CME occurs at the outer part of an AR, then the whole process can be mild. The magnetic field is weak and the linear velocity of the eruption is small.

After the flare and CME/filament eruption, we can observe many different types of waves. For example:

1. Moreton waves are very fast, high-speed waves (1000 km/s) in the chromosphere. This type of waves can be detected in different wavelengths. They were discovered by Athay and Moreton [1961] in  $H\alpha$  line.
2. EIT waves are the “little brothers” of Moreton waves. The propagation speed of the EIT waves have a wide spectrum, from 10 to a few 100 km/s.
3. Aschwanden et al. [1999a] found that coronal loops of ARs oscillate after the eruption.

4. Helioseismic so-called solar quakes could penetrate deeper into the solar interior, and they may be reflected back up to the surface after a white light flare occurs [Kosovichev and Zharkova, 1998].
5. The outward propagation of coronal shock waves, as a part of CMEs, may cause Type II radio bursts.

## 1.7 The classification of solar eruptions

Solar flares and CMEs exhibit diverse phenomena that may reflect how they were initiated. Flares and CMEs often even accompany each other, but not always. Smaller populations of non-flaring filaments can lead to CME occurrences [Gosling et al., 1976, Harrison, 1995, Bein et al., 2012]. Yashiro et al. [2006] found that the probability of a low energetic flare joint with CME occurrence is much smaller than an intensive flare being associated with a large CME. If these two phenomena do occur together, then the pre-, rise- or decay-phase of a flare is temporally associated with the initial-, impulsive acceleration- or propagation-phase of a CME [Zhang et al., 2001].

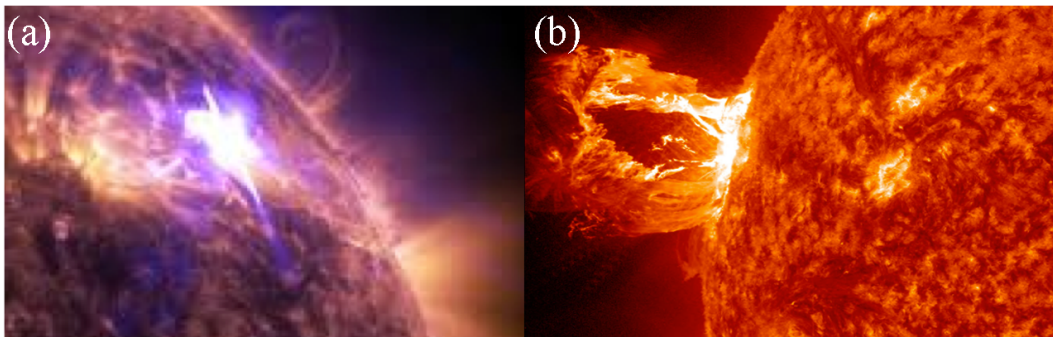


Figure 1.10: Eruptive events on the Sun:(a) flare and (b) CME occurrences.

Actually, a main difference between solar flares and CMEs is the scale on which they occur. A flare is small and more local, when compared to a CME (see Fig. 1.10). Flares happen mainly in the lower solar atmosphere, where the magnetic field lines of an AR are highly concentrated. A CME is, however, an absolutely massive eruption that may occur on very large scales. A CME, in terms of its developed size, can be even bigger than the Sun itself. Solar flares and CMEs are classified according to their strength.

The above introduced impulsive events have classification system that is based on their observable features. Here, we give a brief summary of this classification.

### 1.7.1 Flare classification

Before the space age, flares were observed using  $H\alpha$  filters. Since the 1930s,  $H\alpha$  flare classification is based on the visible red spectral line of wavelength 656.28 nm (emitted by H atoms) and ranks flares according to their appearance area in square degrees of heliocentric latitude. The observed flares are classified as "S" for a small flare and by adding the number 1, 2, 3, or 4 for flares of different sizes, where the number 4 means that the visible area of flare is large (see Table 1.3). Furthermore, this flare classification is subdivided into flares as: 'f' for faint, 'n' for normal, or 'b' for brilliant.

Classification	Corrected Area ( $10^{-6}$ solar disk)
S	< 100
1	100 – 250
2	250 – 600
3	600 – 1200
4	> 1200

Table 1.3:  $H\alpha$  flare classification.

Recently, in the space age, the most widely known flare classification system is currently based on data available from the Geostationary Operational Environmental Satellite (GOES) system (see later Sec. 2.2.2). Near-Earth measurements of the maximum X-ray flux at wavelengths from 0.1 to 0.8 nm, as detected by the XRS instrument on-board the GOES-15 satellite, are classed as A, B, C, M, or X type flares (see Table 2.8) since 1970s. These five flare intensity class categories are broken down into a logarithmic scale from 1 to 9. The A-, B- and C-classes are the lower energetic class of solar flares, and they are very abundant. The A-, B- and C-class range have almost no(t yet known) effect on Earth. Sometimes the C-class solar flares, which are long enough in duration, might produce a CME. These CMEs are in general slow and weak, therefore, they do not seem to cause significant geomagnetic disturbances here on Earth.

M-class flares are of medium strength, while X-class flares are the strongest out of all the intensity flare classes. An M-class flare may cause weaker or stronger radio blackouts, but the X intensity flares give rise to strong to extreme radio blackouts on the daylight side of the Earth. If the solar flare is eruptive, with a large coronal mass ejection near the centre of the Sun, it could cause a strong and long-lasting solar radiation storm with extreme geomagnetic storming at Earth.

Classification	Peak Flux Range (Watts/ $m^2$ )
A	$< 10^{-7}$
B	$10^{-7}$ - $10^{-6}$
C	$10^{-6}$ - $10^{-5}$
M	$10^{-5}$ - $10^{-4}$
X	$> 10^{-4}$

Table 1.4: GOES measurements of the maximum X-ray flux at wavelengths from 0.1 to 0.8 nm near Earth.

### 1.7.2 Coronal Mass Ejection (CME) classification

Before we classify the CMEs, we have to take into account the plane of the sky effect. CMEs have many different shapes, however, fundamental differences can be found between narrow CMEs and normal CMEs [Schwenn et al., 2006]. A narrow CME is a jet-like occurrence along open magnetic field lines, usually originating from a coronal hole. Normal CMEs are characterised by a closed coronal loop, see, for example, in the CSHKP model in Fig. 1.9b. The angular width of CMEs projected in the plane of the sky ranges between 2 and 360 degrees. If the angular width of a CME is smaller than  $10^\circ$ , we call it a narrow CME, however, if it is larger than  $10^\circ$ , we call it a normal CME. When the apparent angular width is close to  $360^\circ$ , the phenomenon is referred to as a halo CME. These events own their appearance to the fact that they are directed towards the Earth.

We can examine CMEs, e.g., in white-light, H Lyman- $\alpha$ , soft X-rays, radio, UV, and EUV wavelengths and so on. During an observation, the start time of the CME is associated with the pre-flare state, when the soft X-ray

radiation dominates. Most of the acceleration of the CME occurs within  $2R_{\odot}$ . Their speed could be constant, or it might increase or decrease slightly between 2 and  $6R_{\odot}$ . Furthermore, the projected speeds have a wide range. The measured velocity of a CME is generally the radial (linear) propagation speed of the upper part of a CME frontal loop. Depending on the value of the linear speed of a CME, if the speed is smaller/larger than the velocity of the solar wind, we call it a slow (500-800 km/s)/fast (over 800 km/s) CME [Webb and Howard, 2012]. There is, however, a third type of CME: the stealth CME. This name refers to a CME with no apparent solar surface association, therefore, it has no easily identifiable source region on the Sun. The velocity of this type of CME is smaller than 300 km/s according to Howard and Harrison [2013]. The estimated mass of a CME falls in the range of  $10^{11}$ -  $10^{13}$  kg, which is about ten times the mass of a prominence. These latter CMEs are the events whose occurrence is absolutely vital to predict.

Evans [2013] introduced a more elaborate CME classification, which is based on the transient speed of the CMEs from the SOHO/LASCO (Solar and Heliospheric Observatory/ Large Angle Spectrometric Coronagraph<sup>1</sup>) catalogue. Detailed in Fig. 1.11, the five classes are based on the rate of occurrence of CMEs, and they provide indication about the frequency of such an event per year.

## 1.8 Space Weather

The continuous flux of solar particles suddenly increases in the Earth's upper atmosphere when a high-intensity (e.g. above M5-class) solar flare or a massive CME reaches the Earth. The frequency of these most energetic eruptions of the entire Solar System follows the 11-year solar cycle, hinting towards their magnetic solar origin.

At the peak of the solar activity cycle, several dangerously high-intensity class flares and CMEs may occur (i.e. around monthly 2-3). A flare event produces radiation at various wavelengths, which may have unfortunate consequences. The high-energy solar flares affect the ionosphere immediately, with adverse effects upon communications and radio navigation. Solar energetic particles can reach the Earth in about 20 minutes to several hours, threatening

---

<sup>1</sup>[http://cdaw.gsfc.nasa.gov/CME\\_list/](http://cdaw.gsfc.nasa.gov/CME_list/)

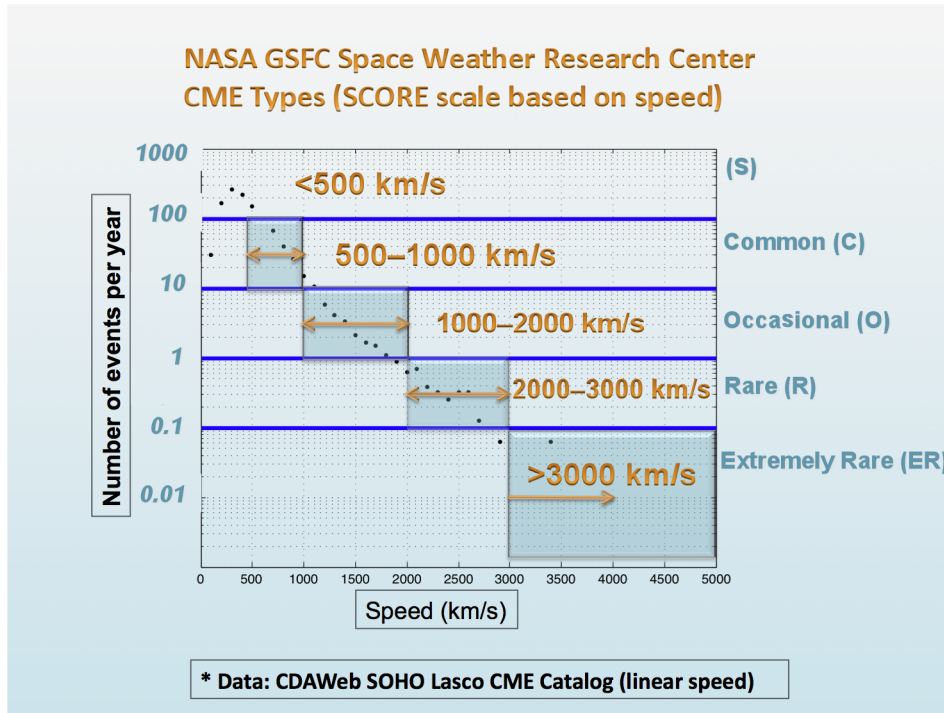


Figure 1.11: The types of the detected CME based on the transient speed  
Credit:NASA.

the electronics of spacecraft and unprotected astronauts, as they rise to 10.000 times the quiet background flux. However, if the flare is further associated with CME, which has a large amount southward directed magnetic field and hits the Earth's upper atmosphere, then this interaction can result in additional dramatic consequences for a number of ground-based (pipelines, power lines) and space-based infrastructures (telecommunication, GPS) (see. Fig. 1.14). A strong magnetic storm could cause over-voltage in integrated circuit chips of computers, television sets, microwave ovens, telephones and so on. These societal assets and services are vital for the economic welfare and security of every citizen, but may be subject to failure due to solar activity, as it has indeed happened in the past.

The interaction of solar activity with the Earth's upper atmosphere occurs

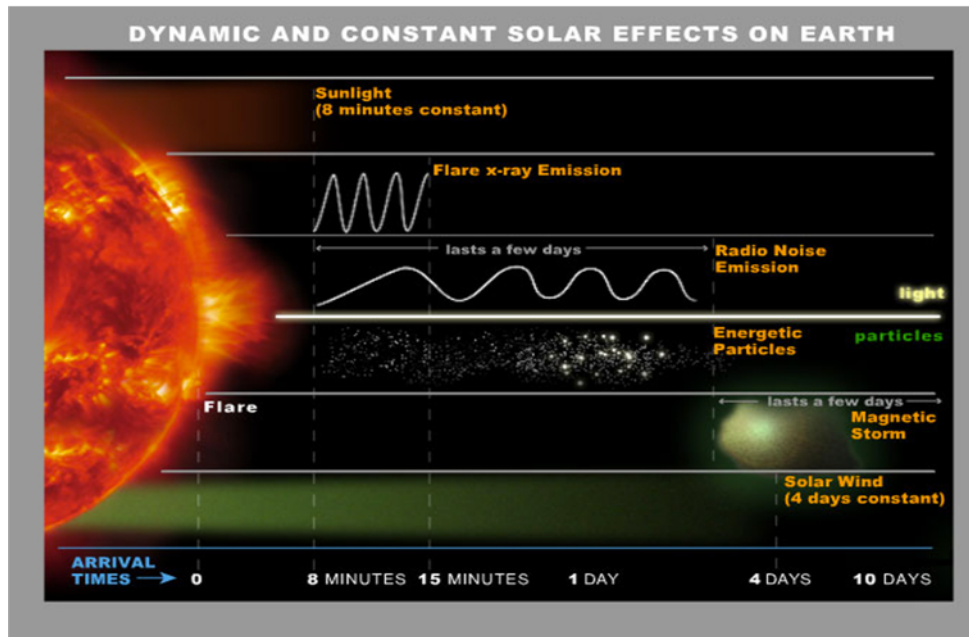


Figure 1.12: Demonstration of the various eruptive and dynamic effects of solar phenomena on the Earth as a function of time. (Credit: NASA/Berkley).

through a complex series of events often referred to as Space Weather. Space Weather was born as a concept thanks to the so-called Carrington event. On 1st of September in 1859, R.C. Carrington and R. Hodgson while carrying out routine sunspot observations at different locations, both witnessed a major optical (i.e. white light) flare. Carrington reported [Carrington, 1859] that the huge solar event caused a strong geomagnetic storm only 17 hours and 40 minutes later. Auroras were sighted up to as low as  $20^\circ$  geomagnetic latitudes, and electric surges occurred from ground-induced currents in telegraph wires, both in Europe and the U.S. Tsurutani et al. [2005a,c,b] have newly calibrated the ground-based magnetometer data of the Carrington flare geomagnetic storm that can be compared with those strongest events in the past 150 years.

Let us briefly summarise a few major examples. One of the most famous cases in the past 150 years is the geomagnetic disturbance during which Quebec (Canada), suffered an electrical power blackout in 1989 [Cid et al., 2014]. A powerful explosion happened on the Sun on March 10, 1989. The solar flare immediately caused short-wave radio interference on the dayside of the Earth. The accompanying billion-ton plasma CME rushed straight towards Earth. On



Figure 1.13: Large solar eruption can damage satellites, electrical grids, pipelines and radio communication. Credit: nasa.gov

the evening of March 12, the vast cloud of solar plasma finally hits our planet's upper atmosphere, and caused colourful Northern Lights that could be seen as far south as Florida and Cuba. The interaction of the solar plasma with our ground-based facilities actually created electrical currents in this facilities, across much of North America. Later the currents found a weakness in the electrical power grid of Quebec. The solar storm have caused blackouts that effected millions of people.

In the 23rd Solar Cycle lasting from 1996 to 2008, huge flares with CME



Figure 1.14: Transformer severe internal damage caused by the space storm of March 13 1989 in Quebec, Canada. The local population suffered an electrical power blackout in 1989. Credit: nasa.gov

occurrence took place [Cid et al., 2014]. More than 10 years ago, on April 2, 2001, an X20 flare with the accompanying CME left the Sun from the NOAA (National Oceanic and Atmospheric Administration) 9393 Active Region (AR) on the west solar limb. Additionally, the largest solar flare ever recorded since the beginning of the satellite measurements was estimated to be an X28 solar flare with CME that occurred on November 4th, 2003. Fortunately, the NOAA 10486 sunspot group that was the cradle of this solar eruption had already rotated largely to the west solar limb.

The most important recent event out of all the extreme events was a CME that erupted from the Sun on July 23, 2012. The velocity of the CME was as large as 3000 km/s, which is over four times faster than a typical fast CME velocity. Fortunately, Earth was not in the path of this CME, but, the plasmoid hit the STEREO-A spacecraft that could measure the parameters of such an event. Researchers concluded that the storm was one of the strongest in recorded history, some had the view that it might be even stronger than the Carrington flare [Russell et al., 2013, Patsourakos et al., 2013].

In September 2017, space storms disrupted shortwave radios for hours preventing emergency responses to hurricanes that were about to tear apart the Caribbean <sup>2</sup>.

---

<sup>2</sup><https://agupubs.onlinelibrary.wiley.com/doi/full/10.1029/2018SW001897>

In the UK Government’s National Risk Registry, hazards from Space Weather are listed as high as number 2 as of writing. Major international funding bodies, e.g. NASA, NSF or the EU’s Horizon 2020, all consider it a high priority issue in their research strategy agenda to reliably and accurately predict and protect from Space Weather events in our era of human space exploration. A crucial difference between today’s world and the one from the many centuries ago is that we are now substantially more reliant upon computers and communications to run our commerce, work facilities, and even our forms of entertainment and recreation. The initial 15 communication satellites in space in 1989 nowadays have been joined by more than further 500 satellites. Mobile phones, computers, and the internet have become an industry worth several billions of pound that are all vulnerable to space storms. Actually, we need even more satellites, more electricity flowing in our power grid systems, which will have to work under loads, originating from Space, unheard of in the past. It is now believed that one of the biggest threat of civilisation may breakdown come from Space Weather. The question is not anymore ”whether it will occur”, but when.

Nowadays, one of the burning questions of solar activity research is to understand clearly the causes and dynamics of Space Weather phenomena. Furthermore, the goal is to develop a reliable flare and CME prediction method in order to protect mankind, as well as our sophisticated technological systems that might be at considerable risk from high-speed charged particles blowing often abruptly off the Sun. With this Thesis we will make a step in the direction to develop a method of Space Weather predicting, in particular, to improve flare prediction.

## 1.9 Thesis Aims

We have already developed a flare prediction method. The method is based on tracking changes of the magnetic configuration of  $\delta$ -spots of the ARs in the photosphere, as flare pre-cursors, with about an hourly temporal resolution, for predicting flares above M5-class [Korsós et al., 2015]. Our method employs the weighted horizontal gradient of the magnetic field ( $WG_M$ ). The  $WG_M$  proxy is defined between two spot-groups with opposite polarities in the entire  $\delta$ -spot. In all the observed flare cases, two typical pre-cursor patterns were discovered with the  $WG_M$  method:

1. The pre-flare behavior of the  $WG_M$  quantity itself exhibits characteristic patterns: faster increase phase with a maximum value at its peak. After reaching the maximum value, the  $WG_M$  shows a gradual decrease prior to flaring.
2. The pre-flare behavior pattern of the distance parameter is based on the converging-diverging motion between the area-weighted barycentres of the positive and negative polarities of the AR prior to a flare. We found that flare occurs when the distance between the barycenters is approximately equal to the corresponding distance at the beginning of the converging phase.

These two pre-flare behaviors allowed us to elaborate on some of the most important properties of an imminent flare:

- The first one is the estimation of the expected flare intensity. This is based on the relationship between the values of the maxima of the  $WG_M$  ( $WG_M^{max}$ ) and the highest associated GOES flare intensity class of ARs.
- Next is the estimation of the flare onset time. The estimate is based on the relationship found between the duration of the receding motion of the opposite polarities until the flare onset, and the duration of the approaching motion of the opposite polarities.
- The last feature is the percentage difference ( $WG_M^{\%}$ ) calculated between the values of pre-flare  $WG_M^{max}$  and the values of the  $WG_M$  at the moment of flare onset ( $WG_M^{flare}$ ). If  $WG_M^{\%}$  is over 54%, no further flare of the same class or above would be expected; but, if  $WG_M^{\%}$  is less than  $\sim 42\%$ , further flares of the same class could be probable within about an 18 hour window.

The aim of this Thesis is to further develop the  $WG_M$  method for a more accurate flare prediction. The overall research goal is to address three questions in a series of studies:

- *Are the two typical pre-flare patterns valid across the entire GOES flare spectrum, or not?* In 61 flare cases, Korsós et al. [2015] demonstrated that the  $WG_M$  could be successfully applied to help identify typical features

preceding flares with classes above M5. Later, in Zheng et al. [2015] and in Korsós and Ruderman [2016], the  $WG_M$  method was applied to case studies of lower than M5 flare cases. Here, we extend the previous analysis of high-energy flares to include both medium (M) and low-energy (C and B) flares to find the answer to the question raised above.

- *Can we reproduce our observational findings by a simulated flaring AR?* We have also further probed and tested the flare prediction capability of the  $WG_M$  method, by applying it to MHD simulations generating solar-like flares. Four flares emanated from a  $\delta$ -type AR, according to the energy released, two of them can be classed as GOES B-type and the remaining two as C-type. In order to develop a reliable prediction method, we also propose to extend our investigations from the photosphere into chromosphere and the low corona. The concept is that flares actually occur higher up in the solar atmosphere and not in the photosphere. We followed the pre-flare evolution of the  $WG_M$  and the behavior of the distance parameter at various heights in the solar atmosphere to increase the application capability of the  $WG_M$  method.
- *Is it possible to increase the flare prediction capability of our method if we extend our investigations in 3D embracing an observed solar atmospheric region?* Based on the underlying ideas of the previous question, and to make a leap forward in developing SW forecast capability (and capacity), we generalise our forecast method, by applying it to 3D ARs in the lower solar atmosphere, in order to identify the optimum height for flare prediction. Here, we expect to increase the forecasting capability, with having important practical implications relevant to flare prediction. Specifically, we (i) investigate the pre-flare dynamics and the related physical processes in the 3D solar atmosphere by constructing the magnetic topology above ARs and (ii) track their temporal evolution by applying the  $WG_M$  method. Our aims are realised by the objectives of (a) acquiring knowledge to implement potential and non-linear magnetic field exploration techniques and (b) creating a data catalogue of 3D magnetic mapping of the AR(s).

The remainder of this thesis is organised as follows. The sources of the observations, data catalogues and applied methods for our studies are described in Chapter 2.

In Chapter 3, we briefly introduce and apply the  $WG_M$  method to the different kinds of energetic flares, i.e. between class B and X flares. Furthermore, we present an extended statistical analysis of AR cases and summarise our findings.

In Chapter 4, to test the reliability of the  $WG_M$  method, we perform a detailed analysis of the flaring regions of the carried out test simulation in terms of Ohmic heating and temperature increase, in order to compare the findings with those reached by applying the  $WG_M$  method.

In Chapter 5, a significant number of the 3D investigations for developing a reliable flare prediction method are described. We examine the pre-flare dynamics of 13 ARs in the lower solar atmosphere by constructing 3D magnetic skeletons. Furthermore, we perform a detailed comparative analysis between potential field (PF) and non-linear force free field (NLFFF) extrapolations in three flaring AR cases. At the end of Chapter 5, we conclude our findings about the increased prediction capability of the method.

Finally, the main results and conclusions of the studies, including prospects for future work, are summarised in Chapter 6.

# Chapter 2

## Data initialisation and database

In the course of this thesis numerous data products from ground- and space-based observatories were used to analyse solar active regions before the flare occurrences. Here, we give a short description of the data and their preprocessing in Sec. 2.1. Next, we introduce the concept of pre-flare dynamic analysis of a flaring AR in Sec. 2.2.1. Furthermore, the presented method in Sec. 2.2.1 uses several numerical codes and different solar data catalogues, which are described in Sec. 2.2.2, Sec. 2.2.3 and Sec. 2.2.4.

## 2.1 Data source

One of the most fascinating characteristics of the Sun is its magnetic field. The magnetic field itself is bringing order to the chaos of solar events and phenomena. Spectropolarimetric measurements allow to deduce the magnetic field strength and its orientation by means of the Zeeman effect. In this section, the Zeeman effect and the instruments of the magnetic field measurements are discussed briefly in view of how to image the LOS and the full vector magnetic field components. At the end of this section, we introduce briefly how we can obtain the heliographic coordinates of a sunspot from space-based observations.

### 2.1.1 Zeeman effect

It is well known that the energy states of atoms are characterised by discrete energy levels. When an electron is excited by e.g. photon absorption or collision, the electron state makes transitions between the allowed energy levels. The associated emitted light forms a discrete spectrum, reflecting the quantised nature of energy levels. In the presence of magnetic field, these energy levels can shift [Herzberg, 1950]. This is called the Zeeman effect.

The basic principle of magnetic field measurement is to employ the Zeeman effect. The polarisation of the splitting components refers to the direction of the magnetic field, as demonstrated in Fig. 2.1. The spectral lines split into linearly and circularly polarised components, depending on the LOS with respect to the magnetic field direction (longitudinal field or transverse field). So, for example, when we observe along the magnetic field then we detect only two opposite circular polarisation  $\sigma$ -components (middle panel of Fig. 2.1). But, if we observe perpendicular to the field we detect one  $\Pi$ -linearly polarised component and the two  $\sigma$ -components linearly polarised in the perpendicular direction (bottom panel of Fig. 2.1).

Once, we know the direction of the magnetic field then we also would like to measure the strength of this magnetic field, which can be obtained by the spectral line shifts or polarisation. The magnitude of polarisation is given in wavelength by

$$\Delta\lambda = 4.7 \cdot 10^{-13} g \lambda^2 B, \quad (2.1)$$

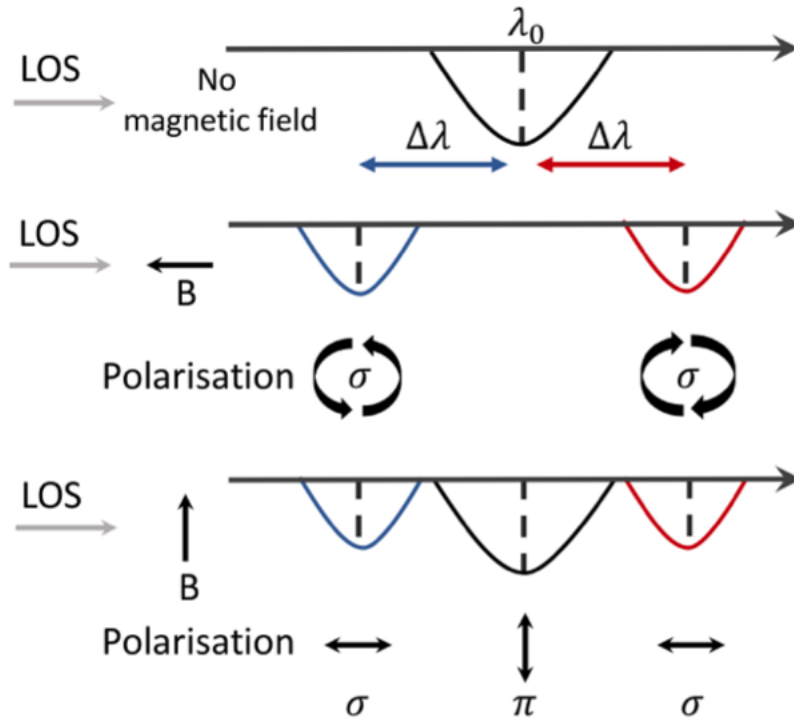


Figure 2.1: On the top, the observed line is not split up because there is no magnetic field. In the middle, a LOS magnetic field causes circularly polarised split components of the spectral line. At the bottom, the transverse field causes linearly polarised split components of the spectral line.

where  $\lambda$  is the wavelength in  $\text{\AA}$ ,  $B$  refers to the magnetic field strength in Gauss and the  $g$  is a so-called Landé factor (a spectroscopic parameter). To measure the strength of magnetic field, the best choice seems to be spectral line with  $g=3$ , e.g. the Fe I or Ni I lines. If  $g=3$  then the separation of quantum states into three different energy levels results in three different excitation states with slightly different energies that give rise to three spectral lines of slightly different energy upon relaxation of the atom. This is the simplest case of the Zeeman effect, known as the normal Zeeman effect.

If the magnetic field is strong (above 1000 G) then the splitting components by the normal Zeeman effect are very sharp and well separated. However, when the solar magnetic field is weak, therefore the splitting of spectral line is not clearly separated. In this case, we can observe only the polarisation of

the line profile, because the Zeeman splitting  $\Delta\lambda$  becomes smaller than the line width. To accomplish a longitudinal field map from measurements of weak magnetic fields, one needs two narrow-band images, each displaced by  $\pm\Delta\lambda$  from the nominal line position. One of the most common tools used to obtain two narrow-band images is the so-called Michelson interferometer.

### 2.1.2 Michelson interferometer

The Michelson interferometer is a popular device mounted on solar space telescopes, because for observations from a space-based platform one needs a compact and reliable instrument, in general with 2D imaging. This has led to designs in which the spectrograph is replaced by a tunable narrowband filter with a bandwidth of typically  $0.1 \text{ \AA}$ , which can isolate the wing of a spectral line to be used for Doppler and Zeeman measurements. The Michelson interferometer is an optical interferometry, which produces interference between two beams of light, as demonstrated by Figure 2.2.

First, as Figure 2.2 presents, a monochromatic beam light enters the Michelson interferometer cube and it splits this light into two beams by a polarising beam splitter. One beam polarisation is reflected by the beam splitter and enters the air arm. The other, orthogonally polarised beam, is transmitted and goes to the glass arm. The two beams travel through quarter-wave plates placed in each arm and are reflected back from the arm ends. After that the reflected beams are passing through, again, the quarter-wave plate. Then the beams are combined at the beam splitter, forming interference fringes and exit through the quarter-wave plate towards the CCD. The combined beam is leaving the Michelson cube with an elliptical polarisation, which depends on the wavelength, as in the case of a birefringent filter. The phase of the emerged orthogonally polarised light depends on the angle of the rotating half-wave plate. At the end, the phase of the modulation is related to the Doppler shift of the solar spectral line. Also, the outgoing monochromatic light can be described by the so-called Stokes-parameters to derive information about the solar magnetic field.

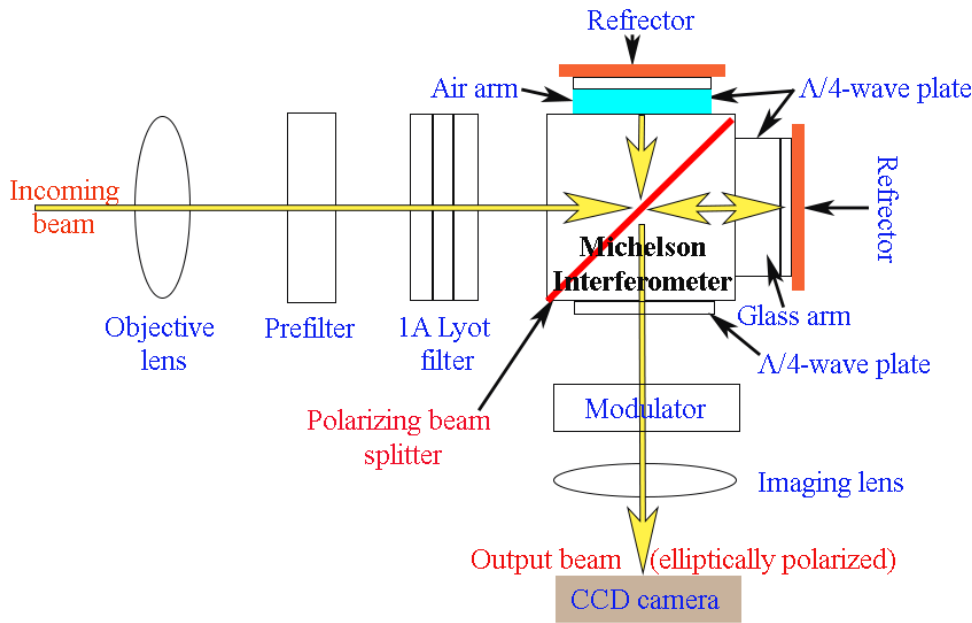


Figure 2.2: The Michelson interferometer used as narrow-band filter.

### 2.1.3 Stokes-parameters

In 1856, Stokes showed that a general elliptically polarised beam of light can be described by four parameters. For example, the size and shape of the ellipse, its orientation with respect to some fixed spatial axes, and the direction of rotation of the ellipse could be a choice of these parameters. The four parameters are not a preferred coordinate system of the space, but they can be (easily) measured. They provide an alternative description of the polarisation state which is experimentally convenient because each parameter corresponds to a sum or difference of measurable intensities.

The four Stokes parameters are labelled as  $I$ ,  $Q$ ,  $U$ ,  $V$ , where the first parameter,  $I$ , is total intensity and sum of any two orthogonal polarisations. The second one,  $Q$ , is the radiance linearly polarised in the direction parallel or perpendicular to the reference plane, while  $U$  is the radiance linearly polarised in the directions  $45^\circ$  to the reference plane. Last but not least,  $V$  is the radiance circularly polarised component.

However, in general, light is only just partially polarised that is why the

degree and direction of polarisation are also important from an observational point of view. The degree and direction of polarisation can be determined also by the measured Stokes parameters. Firstly, the degree of light polarisation,  $P$ , is given by

$$P = \frac{\sqrt{Q^2 + U^2 + V^2}}{I} \quad (2.2)$$

and, next, the direction angle,  $\chi$ , is obtained by

$$\tan 2\chi = \frac{U}{Q}. \quad (2.3)$$

However, to determine the components of the vector magnetic field we have to process these data iteratively, i.e. with a so-called inversion code [see, e.g. the VFISV Milne-Eddington Inversions, NICOL, HAZEL and etc. Asensio Ramos and de la Cruz Rodríguez, 2015]. An inversion code is a computer program, which provides information about the magnetic properties of different regions from the interpretation of the Stokes parameters, like in Fig. 2.3. Fig. 2.3 itself demonstrates how the inverted vector magnetic field components correspond to the measured Stokes parameters in the case of an AR. Fig. 2.3a shows the measured Stokes parameters  $I/Q/U/V$  which are inverted to determine the continuum intensity and the three vector magnetic field components  $B_{los}/B_{trans}/B_{azim}$  of an AR, respectively.

#### 2.1.4 Magnetic field measurements in space

The Michelson interferometer is one of the popular mounted instruments on the solar space telescopes to obtain magnetic field measurements, as we mentioned before. There are a number of successful space missions providing continuously and routinely photospheric magnetic field measurements and continuum images, e.g. SOHO (Solar and Heliospheric Observatory) and SDO (Solar Dynamics Observatory). SOHO and SDO carry synoptic instruments with full-disk capability intended for precision Doppler velocity measurements for helioseismology in addition to sensing the surface magnetic field. The magnetic field observations of the SOHO and SDO satellites are based on the principles outlined in Sections 2.1.1- 2.1.3.

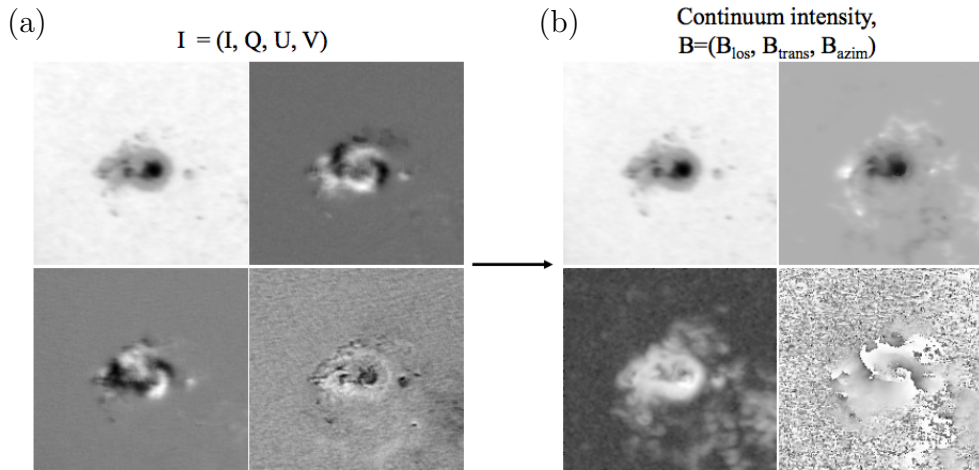


Figure 2.3: Example of inverting the vector magnetic field components. Credit: Stéphane Régnier (website: <http://www.astro.gla.ac.uk>)

### SOHO - The Michelson Doppler Imager (MDI)

The SOHO/Michelson Doppler Imager (MDI) is one of the leading producers of solar magnetic data by a satellite. MDI measures velocity and magnetic fields in the photosphere to learn about the physical conditions in the convection zone and about the magnetic fields which control the structures of the corona. The SOHO satellite is constructed and operated under the joint auspices of the European Space Agency (ESA) and the National Aeronautics and Space Administration (NASA). SOHO was launched on December 2, 1995 and is located in a halo orbit close to the Earth-Sun L1 Lagrange point. The choice of halo orbits around L1 is a result of the interaction between the gravitational pull of the Earth-Sun system, and, the Coriolis and centrifugal accelerations on the SOHO spacecraft. SOHO is stabilised by three axes: to control the pointing, roll angle and orbital motion. SOHO's optical axis is pointing at the center of the Sun and the roll of the spacecraft is aligned to the Sun's axis of rotation that is always contained in the spacecraft's XZ plane.

The setup of MDI is based on a modification of the Fourier Tachometer technique [Brown and Evans Dunn, 1981]. The telescope collects the sunlight through a series of filters onto a 1024x1024 pixels charge-coupled device (CCD) camera and it measures the Doppler velocity and LOS magnetic field with 96 seconds sequence. The spatial resolution of MDI is better than 10 arcseconds for



Nickel (Ni) absorption line at  $6768 \text{ \AA}$  with a full width at half maximum of  $50 \text{ \AA}$ . This normal Zeeman triplet absorption line develops near the middle of the photosphere. The next element is the blocker and it has an  $8 \text{ \AA}$  bandpass. The third element is the Lyot-filter with a  $465 \text{ m\AA}$  bandpass which is a wide-field and temperature-compensated device. The transmission bandpass of the fixed filters system is  $454 \text{ m\AA}$ . The two tuneable Michelson interferometers are the last elements and they are also the heart of the filter system. The two Michelson Doppler imagers have sinusoidal bandpasses with periods of  $377 \text{ m\AA}$  and  $189 \text{ m\AA}$  and can be tuned simply by rotation of half-wave plates. The Michelson interferometers give the opportunity to make filtergrams in a narrow ( $94 \text{ m\AA}$ ) bandpass anywhere in the vicinity of the Ni line [Scherrer et al., 1995].

### SDO - Helioseismic and Magnetic Imager (HMI)

SDO is, in some aspects, a further developed and upgraded version of the SOHO satellite. SDO was launched on February 11, 2010 on its board with the Helioseismic and Magnetic Imager (MDI) instrument [Schou et al., 2012, Scherrer et al., 2012] constructed as a lead by NASA's Goddard Space Flight Center in Greenbelt. The HMI instrument is similar in design to the MDI but it does not have an optical layout of the system. This instrument incorporates a number of features that represent significant upgrades from MDI. The goal of SDO is to understand the influence of the Sun on Earth and the near-Earth space by studying the solar atmosphere on small scales of space and time observable in many wavelengths. SDO is also a 3-axis stabilised spacecraft, with two solar arrays and two high-gain antennas in an inclined geosynchronous orbit around Earth.

HMI observes the full solar disk in the neutral Iron absorption line at  $6173 \text{ \AA}$  (Fe I) because this line has a normal Zeeman triplet with high magnetic sensitivity. The polarisation techniques of HMI are much more sophisticated than that of the MDI. Here, the polarisation analysis is carried out with rotating retarders mounted permanently in the beam. The filter system includes the blocking filter, a five-elements Lyot filter and two Michelson interferometers as we can see in Fig. 2.4b. The last three filters can be tuned by rotating retarder waveplates in a  $76 \text{ m\AA}$  bandpass to over  $680 \text{ m\AA}$ . Furthermore, the instrument is capable of vector magnetometry because these waveplates give all the different polarisation Stokes vectors. The angular resolution of the instrument is  $0.1$  arcsecond, with the field-of-view covering the entire solar disk. Two  $4096 \times 4096$

pixels CCD cameras are used separately. Images are made in a sequence of tuning and polarisations at every 4 second cadence for each camera. One camera is dedicated to a 45 s Doppler and LOS field sequence while the other to a 90 s vector field sequence. Therefore, not only the resolution is better but also the data rates are with a higher cadence than MDI.

### 2.1.5 Transformation of sunspot coordinates

For our aim to study the pre-flare kinetics and evolution of a sunspot, the appropriate coordinates of an AR are indispensable to be established. The employed SOHO/MDI and SDO/HMI satellite data are stored in a so-called FITS (Flexible Image Transport System) file format, which includes many provisions for describing photometric, temporal and spatial information, together with a metadata image. The FITS files have optional features for the MDI and HMI data, what are available from the e.g. <http://sdac.virtualsolar.org/cgi/search> website.

For our study, the most practical coordinate system is the heliographic one because it is easy to measure and follow the position of sunspots on the Sun. This coordinate system was developed by Richard Carrington in the 1850s. Carrington determined the solar rotation rate by studying sunspots on the solar disk. Carrington [1863] defined a fixed coordinate system, called today as the Carrington-coordinate system, with five heliographic coordinates ( $L$ ,  $L_0$ ,  $B$ ,  $B_0$  and  $P$  as in Fig. 2.5b) that rotates around in a sidereal frame every 25.38 days. For this purpose, an internationally agreed reference point meridian  $L_0=0$  is defined as the central meridian which passed through the apparent centre of the disk on 1st of January in 1854 at Greenwich 12:00. This reference meridian is called the Carrington meridian. Every synodic Carrington rotation (27.27 days) is counted from this reference time with the central meridian longitude decreasing from  $360^\circ$  to  $0^\circ$  during each full rotation. The 27.27 days is a mean synodic rotation rate because of the eccentricity of the Earth's orbit, therefore, it varies a little during the year. The heliographic latitude of the solar disk center,  $B_0$ , varies  $\pm 7.25^\circ$  because the Sun's rotational axis is inclined to the ecliptic plane by this angle. In June and December, when  $B_0=0$ , the sunspots travel transverse through the disk. The position angle,  $P$ , superimposes the Earth's equator on to the ecliptic. The inclination of the superimposing effect changes between  $\pm 23.37^\circ$  within a year.  $P$  also varies between  $\pm 26.37^\circ$  due to the combination effect of  $B_0$  and  $P$ . Additionally, the actual values of  $P$ ,  $B_0$  and



is expedient to measure the position of sunspots. Therefore, we need to convert the Cartesian coordinates into polar ( $r$ ,  $\theta$ ) coordinates by using

$$r = \sqrt{x^2 + y^2}, \quad \theta = \arctan y/x. \quad (2.4)$$

Next, the angular distance ( $\rho$ ) of a sunspot from the solar disk center is obtained from:

$$\sin \rho = \frac{r}{R}, \quad (2.5)$$

where  $R$  is the radius of the projected image and  $r$  is the distance of the feature from the disk center.  $R$  is also stored in the FITS header file and  $r$  can be determined from Eq. (2.4).

Next, to calculate  $B$  and the heliographic distance ( $l$ ) from the central meridian, the following equations are required:

$$\sin B = \cos \varrho \sin B_0 + \sin \varrho \cos B_0 \sin \theta \quad (2.6)$$

and

$$\sin l = \frac{\cos \theta \sin \varrho}{\cos B}. \quad (2.7)$$

Eq. (2.6) gives directly the true heliographic latitude ( $B$ ) of the sunspot but Eq. (2.7) does not provide the true heliographic longitude ( $L$ ). To calculate  $L$  from the measured  $l$  the following equation is necessary to employ:

$$L = L_0 + l. \quad (2.8)$$

When we obtained the  $B$  and  $L$  coordinates of a sunspot, then it is now possible to follow the evolution of it before flare occurrences.

## 2.2 Preparation of the pre-flare dynamic evolution study of flaring ARs

In this section, we introduce and discuss the relevant data catalogues and application tools for the pre-flare tracking of ARs by employing the *weighted horizontal magnetic gradient* ( $WG_M$ ) method [developed and introduced originally by

Korsós et al., 2015] across a range of heights from the photosphere throughout the chromosphere, transition region and low corona.

First, let us briefly introduce the  $WG_M$  method itself and the GOES (Geostationary Operational Environmental Satellites) flare catalogue which are used for both the photospheric and 3D (i.e. cross-atmospheric) pre-flare tracking studies. Later, in Sections 2.2.3- 2.2.4, we also introduce some further catalogues and tools what are individually used in two different studies.

### 2.2.1 The $WG_M$ method

Firstly, let us outline the key points of the main method of tracking the pre-flare evolution of ARs, as this method plays the central role throughout the whole thesis. In Korsós et al. [2015] (K15 thereafter, respectively), we presented the concept of the weighted horizontal magnetic gradient method, often briefly referred to as the  $WG_M$  method. The  $WG_M$  quantity itself is defined as a proxy to measure the magnetic non-potentiality:

$$WG_M = \left| \frac{\sum_i B_{p,i} \cdot A_{p,i} - \sum_j B_{n,j} \cdot A_{n,j}}{D_{pn}} \right| = \frac{\Phi}{D_{pn}}, \quad (2.9)$$

where  $B$  is the magnetic field and  $A$  is the umbra area. The indices  $p$  and  $n$  denote positive and negative polarities,  $i$  and  $j$  are their running indices in the selected spot cluster.  $\Phi$  is the unsigned magnetic flux.  $D_{pn}$  is the distance between the area-weighted centers of the positive and negative polarities (barycenters) in this cluster, see Fig. 2.6. Figure 2.7 is an example that serves to illustrate the methodological framework of the  $WG_M$  method used in this thesis.

The  $WG_M$  method was applied to 61 ARs, which produced stronger than M5-class flares, based on the GOES flare classification system. The pre-flare dynamics and the related physical processes at the solar surface were investigated using data with an hourly temporal resolution from joint SDD ground- (Debrecen Heliophysical Observatory, DHO) and space-based (Solar and Heliospheric Observatory, SOHO) sunspot data catalogues [see, e.g. Baranyi et al., 2016] from 1996 to 2010. The  $WG_M$  analyses focussed on the vicinity of polarity inversion line(s) (PILs), which is illustrated with red ellipse(s) in Fig. 2.7b. This is the area where the indicative characteristic features of the imminent flaring behaviour appear up to two-three days prior to the actual flare onset.

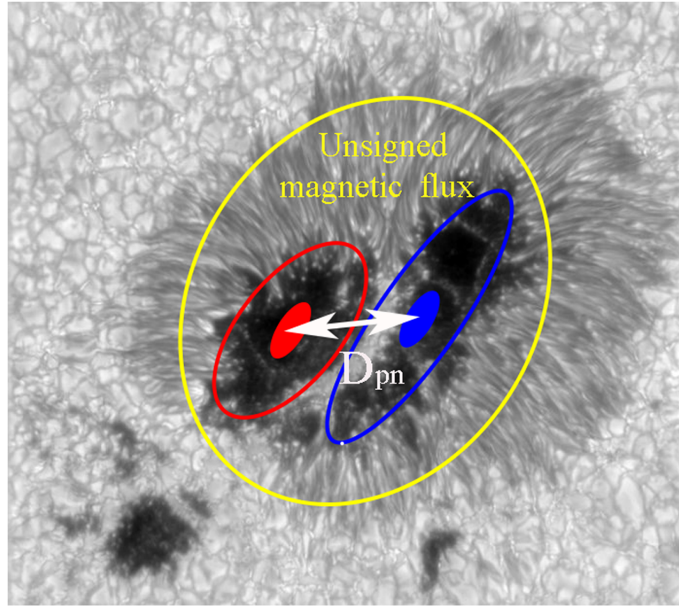


Figure 2.6: Illustration for the  $WG_M$  proxy. The blue/red colour indicates the negative/positive polarity. The ellipses are the considered fluxes within the umbra. The filled ellipses are the barycenters of the positive and negative umbrae. The white double-arrow marks the distance parameter ( $D_{pn}$ ). The yellow ellipse outlines the common penumbra of the opposite polarity umbrae, where the unsigned magnetic flux ( $\Phi$ ) is calculated.

First, K15 identified prominent and characteristic pre-flare patterns of the  $WG_M$  proxy quantity: increasing phase, maximum and gradual decrease prior to flaring. The overall pre-flare behaviour of the  $WG_M$  parameter is approximated by aqua "inverted V-shape" on the top panel of Fig. 2.7a. From this characteristic pre-flare behaviour a linear relationship was found between the pre-flare  $WG_M$  maximum ( $WG_M^{max}$ ) and the largest flare intensity class of the AR investigated. This relationship yields as a tool to estimate the expected flare intensity following the preceding maximum of  $WG_M$ .

Furthermore, the introduction of  $WG_M$  enabled to discover a second flare precursor. Namely, the two barycenters of opposite polarities display a pattern of converging and diverging motions prior to the flare, which is illustrated with a red parabolic curve in the middle panel of Fig. 2.7a.

In the case of 61 flare events, we found that the flare occurs when the

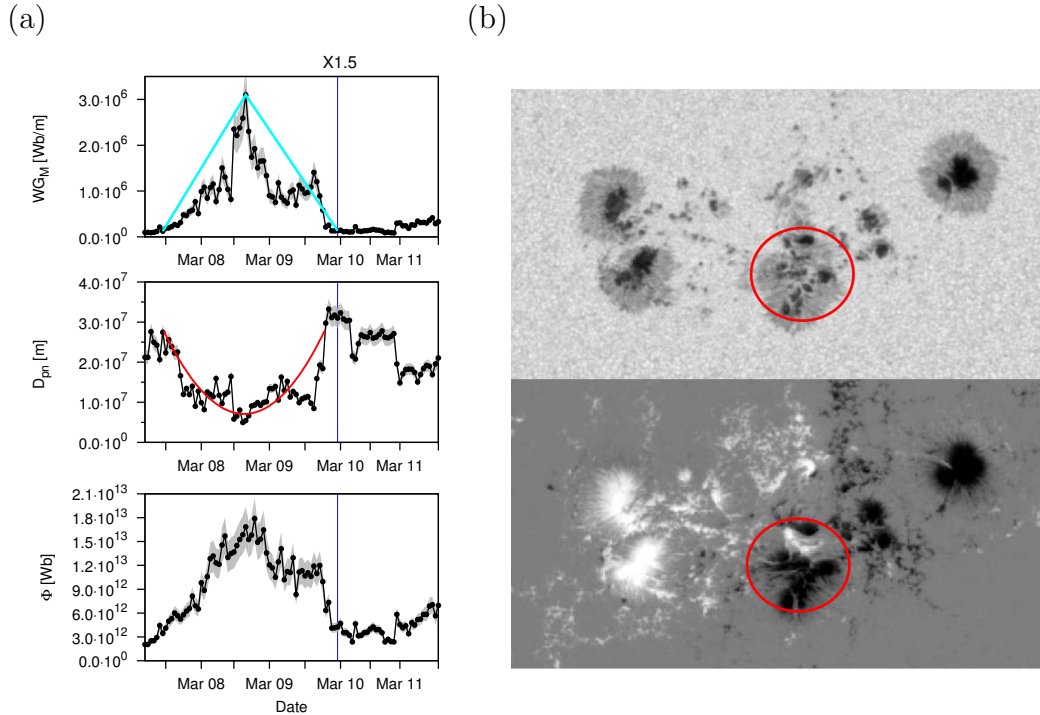


Figure 2.7: (a): The top panel shows the  $WG_M$ , the middle panel plots the distance parameter between the barycentres ( $D_{pn}$ ), and the bottom panel is a plot of the associated unsigned magnetic flux ( $\Phi$ ) as a function of time. The investigated flare onset is indicated by (blue) vertical lines. In the upper panel, the pre-flare behaviour of the  $WG_M$  parameter is highlighted by an aqua ”inverted V-shape”. In the middle panel, the red parabola indicates the pre-flare behaviour of the  $D_{pn}$  parameter. The error is marked with shaded grey. (b): Top panel: Intensity snapshot at 07:59 on 9 March 2011 of AR 11166. Bottom panel: Magnetogram at 07:59 on 9 March 2011.

distance between the barycenters is approximately equal to the corresponding distance at the beginning of the converging phase. With other words, we found that the barycenters would be bouncing back from their closest position and flaring take place only around the moment of time when these barycenters reach their position they had before the approaching phase. This precursor has the capability for a more accurate flare onset time estimation, which is based on the relationship between the duration of the diverging ( $T_{D+F}$ ) and converging ( $T_C$ ) phases of the barycenters of the opposite polarity regions.

Also, K15 investigated separately the i) single-flare case when only one energetic flare took place after  $WG_M^{max}$  and ii) cases when multiple flares erupted after reaching  $WG_M^{max}$ . In the 61 flare cases, the longest study period was 48 hrs from the moment of reaching  $WG_M^{max}$  to the moment of the first flare. The percentage difference ( $WG_M^{\%}$ ) was calculated between the values of  $WG_M^{max}$  and the values of the  $WG_M$  at the moment of flare onset time ( $WG_M^{flare}$ ). In brief, we found the following: if  $WG_M^{\%}$  is over 54%, no further flare of the same GOES class or above would be expected; but, if  $WG_M^{\%}$  is less than  $\sim 42\%$ , further flare(s) of the same GOES class is probable within about an 18-hour window. The longest time interval of a subsequent flare to occur was 18 hrs in the study samples. K15 suggested that these latter features may serve as practical additional flare alert tools.

### 2.2.2 Geostationary Operational Environmental Satellites - GOES flare list

We apply the GOES solar flare event catalogue to select potential flare events for the  $WG_M$  analyses. Actually, nowadays, the GOES catalogue is a standard reference catalogue for most of the space weather research. The GOES program began in 1975 with the launch of the first operational spacecraft. A number of satellites from the GOES spacecraft series provide data through its Space Environment Monitor (SEM) system. The three main components of the space weather monitoring program are the X-rays, energetic particles and the magnetic field. In our work, we use the X-ray measurement of GOES-15. The X-ray sensor of the spacecraft is an ion chamber that yields whole-Sun X-ray fluxes in the 1-8 Å wavelength band. These measurements enable a sensitive means of detecting the start and evolution of solar flares (see Fig. 2.8a).

The GOES daily flare lists<sup>1</sup> are the flare eruption events registered by GOES satellite. In the catalogue, we can find information about the moments of beginning, maximum and end-time of flares. Also, this catalogue includes the flare energy (A1.0,...,9.9; B1.0,...,9.9; C1.0,...,9.9; M1.0,...,9.9 or X1.0-), the position and the NOAA number of the host AR of the X-ray event (see Fig. 2.8b). The kick-off time of a flare is defined as the first minute, in a sequence of 4 minutes, of steep monotonic increase in the 1-8 Å X-ray flux. The

<sup>1</sup><https://www.ngdc.noaa.gov/stp/space-weather/solar-data/solar-features/solar-flares/x-rays/goes/xrs/>

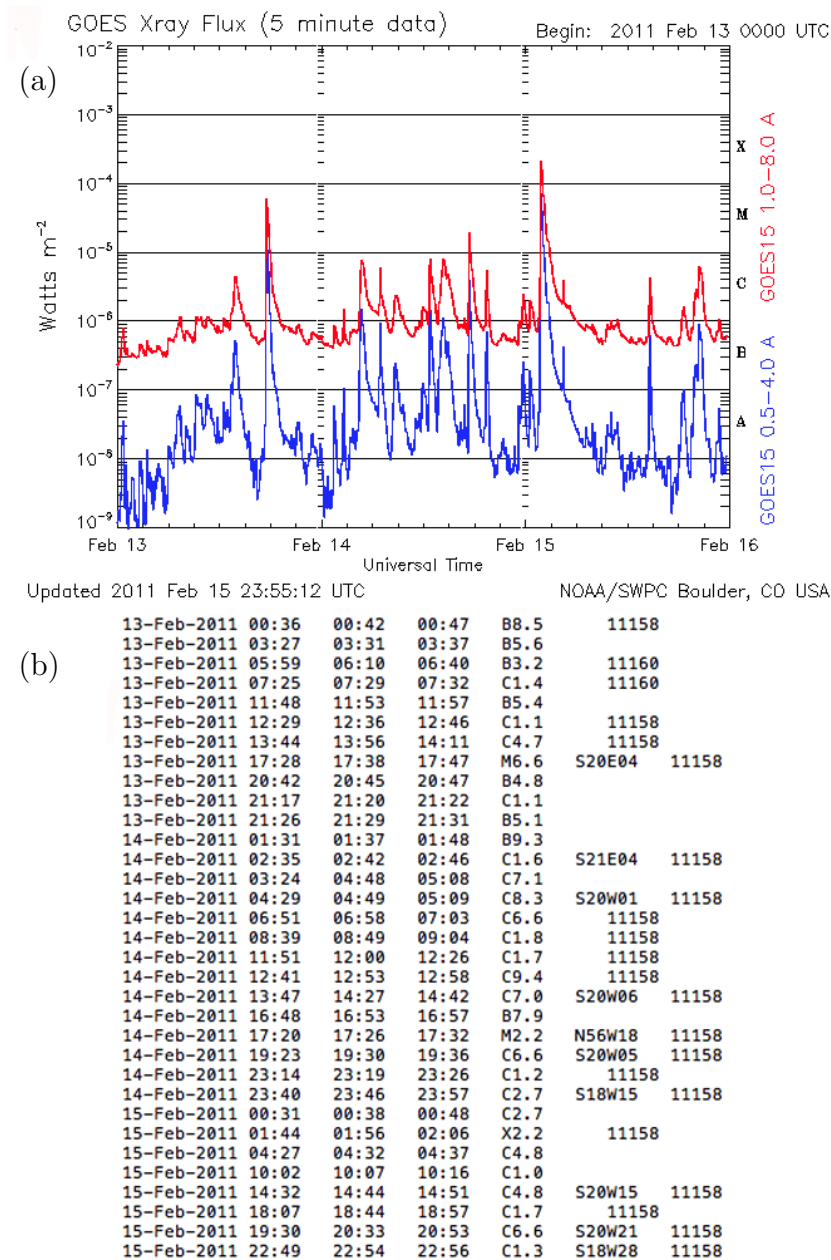


Figure 2.8: (a) Plot of the GOES soft X-ray time profile during February 13th and February 15th of 2011. (b) The corresponding GOES flare list of (a).

maximum time is taken as the minute of the peak X-ray flux. The end time is the time when the flux level decays to a point halfway between the maximum flux and the pre-flare background level. From this catalogue, we employ data at the peak time, the flare energy, the position and the name of host AR of the selected flare events for  $WG_M$  analyses. Actually, we use these data as event reference to search for typical dynamic pre-flare behavior pattern(s) of the host AR taking place days before the flare onset.

### 2.2.3 Photospheric investigation

First, we apply the  $WG_M$  method only in the photosphere to establish whether the two typical pre-flare patterns are detectable across the entire GOES flare spectrum (from B-class to the X-class), or not. For the analyses of photospheric data, we employ the Debrecen Data Sunspot catalogue [Baranyi et al., 2016]. The Debrecen Heliophysical Observatory (DHO) has the most detailed documentation of the sunspots since 1958. The DHO has constructed various solar catalogues<sup>2</sup> based on both ground-based and space-borne observations. We apply catalogues of space-borne observations for our study, namely the SOHO/MDI-Debrecen Data (SDD) and SDO/HMI- Debrecen Data (HMIDD) catalogues. These two catalogues provide accurate and detailed position, area, and mean estimated magnetic field information for all observable sunspots and sunspot groups from 1996 to the end of 2014. The SDD and HMIDD catalogues are based on the SOHO/MDI and SDO/HMI continuum intensity images and magnetogram observations. The two catalogues were produced by the Sunspot Automatic Measurement (SAM) program packages [Győri, 1998, 2015]. SAM automatically finds the sunspots on a solar disk image and determines their parameters. These two catalogues contain the following data for each observed umbra and penumbra of a given sunspot:

- time of observation
- NOAA number of sunspot's group
- the number of the sunspot. The sunspots are sequentially numbered within the sunspot group on the basis of the sunspot's longitude.
- projected and the corrected areas of umbrae

---

<sup>2</sup>Debrecen Sunspot Data Catalogue available at <http://fenyi.solarobs.csfk.mta.hu/>

- Carrington latitude,  $B$
- Carrington longitude,  $L$
- distance in longitude from the central meridian of the Sun,  $LCM$
- position angle,  $P$
- distance from the centre of Sun in terms of Sun's radius,  $r$
- mean magnetic field within the umbra,  $MU$
- mean magnetic field within the penumbra,  $MP$

In the data catalogue, if there is more than one umbra within a penumbra, this fact is identified with a negative number. The negative number is corresponding to the first identified umbra in the common penumbra. If the common penumbra contains positive and negative umbrae then it is considered as a  $\delta$ -spot.

Figure 2.9 demonstrates the online form of the Debrecen Data catalogue with the case of NOAA 11429 on 09/03/2012 at 18:58:59 UT<sup>3</sup>.

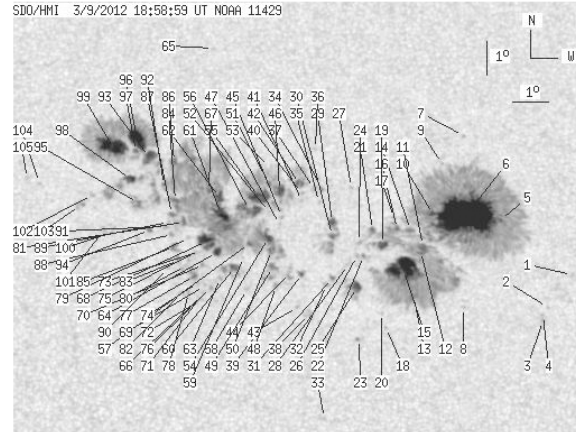
In the SDD and HMIDD catalogues, the uncertainty of position measurements is 0.1 heliographic degree, while measuring the area has an error about 10% [Győri et al., 2011]. It is also worth mentioning that, we do not use the value of  $MU$  because often the observation time of the continuum image and the assigned magnetograms are different and it causes the value of the  $MU$  becoming smaller than the surround  $MP$ . Therefore, carrying out our studies in the photospheric, we determine  $B$  from the umbra area  $A$  by

$$B = f(A) = 265[G] \cdot \ln(A) + 1067[G]. \quad (2.10)$$

Actually, this equation determines the relationship between the mean magnetic field and the umbra area within  $\pm 10^\circ$  from the  $LCM$  with an error of 15% [Korsós et al., 2014]. Furthermore, we need to note that the temporal and spatial resolutions are different of the SDD and HMIDD catalogues. The cadence of the SDD is about one and half hour depending on the availability of the MDI observations. The HMIDD cadence is an hour, also depending on HMI

---

<sup>3</sup>Source: [http://fenyi.solarobs.csfk.mta.hu/ESA/2012/20120309-185859.90/20120309-185859.90\\_11429.html](http://fenyi.solarobs.csfk.mta.hu/ESA/2012/20120309-185859.90/20120309-185859.90_11429.html)



spot	Proj. U	Proj. WS	Corr. U	Corr. WS	B	L	LCM	Pos. angle	r	MU	MP
1	0.00	1.56	0.00	0.87	16.34	306.90	15.02	327.87	0.4694	724.0	598.2
2	0.00	1.04	0.00	0.58	15.38	306.13	14.24	328.08	0.4505	608.0	445.4
3	0.00	1.13	0.00	0.62	14.99	305.97	14.09	327.88	0.4441	972.0	852.2
4	0.00	1.04	0.00	0.57	15.15	305.98	14.10	328.06	0.4463	781.0	692.4
5	1.13	925.49	0.63	515.78	17.88	304.97	13.08	332.92	0.4751	883.9	114.3

Figure 2.9: Example of the online Debrecen Data catalogue. The numbered spots in the continuum intensity image of the NOAA 11429 sunspot group are shown. All the corresponding measured data of the numbered spots of the sunspot group can be seen in the associated table under the image.

observations. The spatial resolution of HMIDD is larger than SDD's because of the differences in the spatial resolution between the HMI (4096 x 4096 pixels) and MDI (1024 x 1024 pixels).

Let us now outline how we apply the  $WG_M$  method successfully to data from the photosphere. Here, we use the following five steps to successfully identify the pre-flare dynamics of a flaring AR:

1. During the entire investigated period it is required that the AR is located between  $-70^\circ$  and  $+70^\circ$  ( $+75^\circ$ ) from the central meridian of the Sun (blue line in Fig. 2.10).
2. During the AR's disk passage, the largest intensity flare-class event of the AR is selected from the GOES flare catalogue.
3. In order to acquire enough preceding data to identify the precursors, the

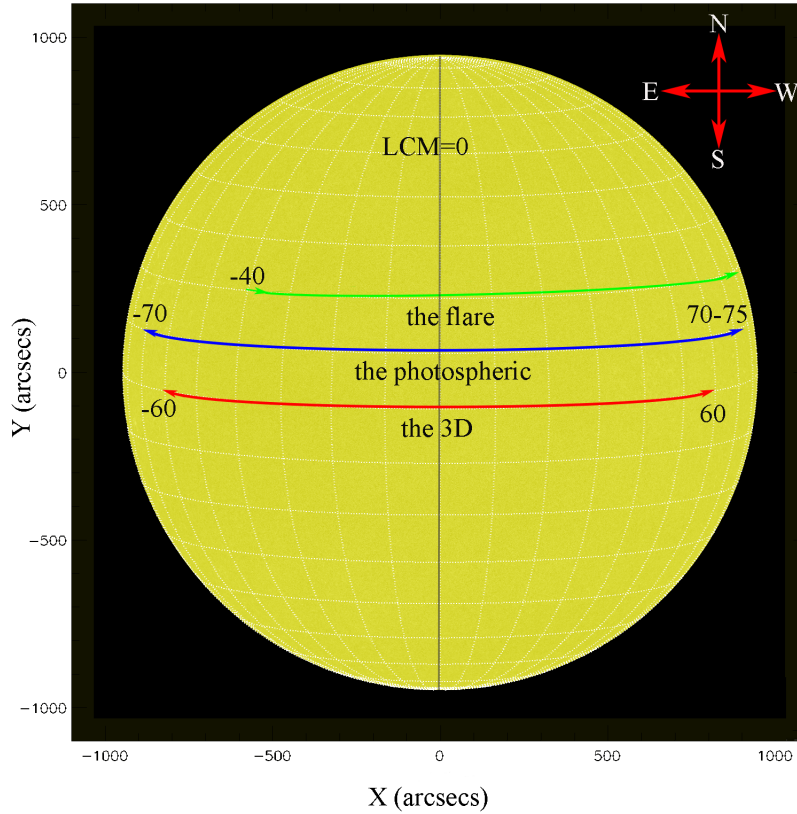


Figure 2.10: Location boundaries of applying the  $WG_M$  method in the photosphere (blue line, refer to Sec. 2.2.3) and for 3D (red line, refer to Sec. 2.2.4) studies are shown. The green line demonstrates the location passage of the investigated flare with  $WG_M$ .

occurrence of the associated strongest flare class could be no further than  $\sim 40^\circ$  east of the central meridian (green line in Fig. 2.10).

4. The  $WG_M$  method is applied in a selected area of the AR. As an initial approach, the selected area is an entire  $\delta$ -spot of the AR where all umbrae are now taken into account for analysis. This assumption is based on the idea that the  $\delta$ -type sunspots themselves are observed and identified as the most probable places for the flare onset. A  $\delta$ -type spot contains opposite polarity umbrae surrounded by a common penumbra, therefore it has polarity inversion line(s) (PIL). It is also well known that solar flares

often are related to PILs [Schrijver, 2007, Louis et al., 2015]. Furthermore, the umbrae are loci of high flux densities, so they are presumably the dominant components of the flare processes. However, it should be noted that the Debrecen sunspot catalogue does not always indicate the two close opposite magnetic polarities as a  $\delta$ -type spot. In this case, the selected area is a circle with a radius of  $1.5^\circ \pm 0.5^\circ$  around the barycentrum of the two closest umbrae with opposite polarities. We have introduced this circle of interest in the studied samples of K15. The diameter of the circle is derived from the common amorphous shaped penumbra of the opposite polarity umbrae approximated by a circle with a radius of  $1.5^\circ \pm 0.5^\circ$  in Carrington heliographic coordinates. Finally, the selected area is tracked and the evolution (e.g., emergence of new flux or flux cancellation) of umbrae are monitored.

5. At the end, the  $WG_M$  method is applied to the selected area. The evolution of the unsigned magnetic flux, the distance between the area-weighted barycenters of opposite polarities and the  $WG_M$  are followed as outlined below:
  - (a) To establish that a behaviour is related to the upcoming flare rather than merely an insignificant fluctuation, (i) the relative gradient of the rising phase of  $WG_M$  is set at a minimum of 30% and (ii) the relative gradient of the distance parameter of the converging motion is greater than 10% for a period of at least 4 hrs. Furthermore, a maximum of 10% deviation is allowed as the distance increases back to its original value that it had at the moment when the converging phase started.
  - (b) When the relevant pre-flare behaviour of the  $WG_M$  proxy is identified as given in point a) above, then the  $WG_M^{max}$  and  $WG_M^{\%}$  can also be determined. The  $WG_M^{max}$  corresponds to the peak of the aqua "inverted V-shape", and, the  $WG_M^{\%}$  is the value taken at the end of the "inverted V-shape" in the top panel of Fig. 2.7a.
  - (c) Next, the applied parabolic curve, which illustrates the pre-flare behaviour of the distance parameter (middle panel of Fig. 2.7a), is fitted from the starting time of the converging phase to the end of the diverging phase. The minimum of the parabolic curve is the moment of reaching the closest position of the two barycenters. The parabolic

curve was fitted by the QtiPlot<sup>4</sup> tool, which is a cross platform data analysis and scientific visualisation program package.

Finally, let us comment on the errors and uncertainties of the  $WG_M$  method: The uncertainty in the distance parameter is 10% which originates from the error of position and area measurements. The mean error of the estimated magnetic field associated with a certain umbral area has an error of 15%. Therefore, the total calculated uncertainty of  $WG_M$  is 20%.

### 2.2.4 The 3D analyses

Secondly, in this thesis, we apply the  $WG_M$  method in the lower solar atmosphere to establish whether it is possible to increase the flare prediction capability of the method or not. The data processing and the construction of 3D magnetic field structure of ARs were carried out with the extensive use of the IDL program language employing the SolarSoftware general purpose and instrument-specific routines, see Fig. 5.1 as an example of a 3D magnetic skeleton. The SolarSoftware package<sup>5</sup> is a set of integrated software libraries, databases, and system utilities which are suitable for solar common programming and data analysis environment. Perhaps the most important virtue of the SolarSoftware is that we can easily use the FITS files of the MDI and HMI instrument for our analyses.

For our 3D analyses, SDO measurements are more applicable than those from SOHO, because SDO has more accurate and continuous LOS and vector magnetic field data products. Based on SDO measurements, we constructed a high spatial- and temporal-resolution 3D magnetic map data catalogue, which includes the area, mean magnetic field data and the location (Carrington coordinates,  $L$  and  $B$ ) of sunspots of ARs at every 45 km in height from the photosphere into the lower corona on an hourly bases for the selected ARs by the below listed methods.

But, before we construct a 3D magnetic structure of flaring ARs by e.g. PF or NLFFF extrapolations, the applicable ARs now have to satisfy the following criteria:

---

<sup>4</sup><https://www.qtiplot.com/>

<sup>5</sup>The SolarSoftware is downloaded from <https://sohowww.nascom.nasa.gov/solarsoft/>

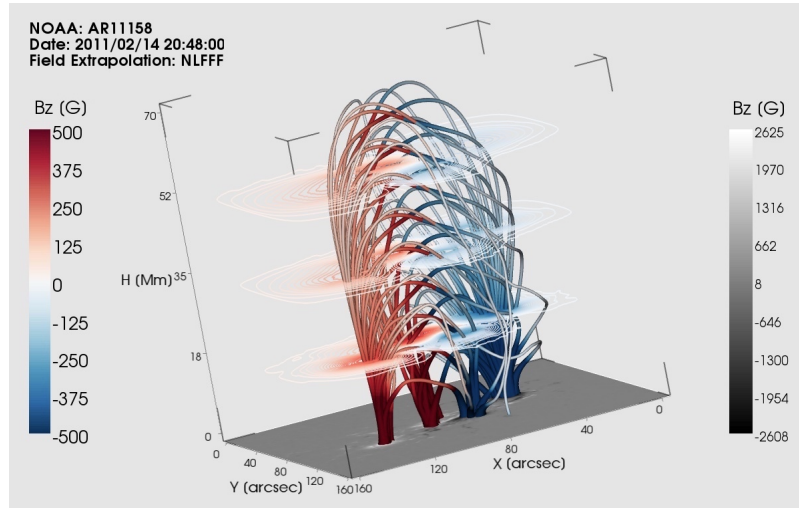


Figure 2.11: The figure illustrates the three-dimensional NLFFF magnetic field of AR 11158. The red-blue colour bar refer to the positive-negative polarity magnetic field values at the different heights in the solar atmosphere. The grey colour bar represents the photospheric  $B_z$  magnetic field measurements values. Credit: Norbert Gyenge

1. During the entire investigated period it is expected that the AR is taking place between  $-60^\circ$  and  $+60^\circ$  from  $LCM$  of the Sun (red line in Fig. 2.10).
2. The largest intensity flare-class of the AR has to be an X-class flare during their disk transit.
3. In order to be able to build up enough preceding data to identify the precursors, the X-class flare should be no further than  $40^\circ$  east of  $LCM$ .
4. The selected AR should have  $\delta$ -spot(s).

These four points are a little different from those when compared to the criteria of the photospheric event selection, which are listed in Sec. 2.2.3.

### PF extrapolation

Now, let us see first the PF extrapolation approaches. Here, we used the HMI LOS magnetograms as a photospheric lower boundary for constructing the magnetic skeleton of an AR embedded in a 3D box. First, we select the potential AR

in the first interested SDO/HMI LOS magnetogram and track it in the magnetogram time sequences. The tracking of magnetic features within these datasets is completed by using the Yet Another Feature Tracking Algorithm<sup>6</sup> [YAFTA; Welsch and Longcope, 2003, DeForest et al., 2007]. YAFTA is accessible from the Solarsoft IDL library. The detection algorithm is based on the clumping method, which enrolls together all contiguous like-polarity pixels with absolute flux densities within a specified threshold, and marks them as a unique element. For our study, we set up the minimum thresholding of both significance limits of the magnetic field contour and area as inputs. These thresholds were set at  $2\sigma$  and 30 pixels through a systematic testing of a variety of parameters with the aim of securing a successful and consistent identification of strong flux elements. The magnetic field strength, area, and cross-sectional diameter of all sunspots of AR could then be recorded for each relevant frame and saved in individual files for further PF extrapolation.

In the PF extrapolation approach, we use the method published by Gary [1989]. The method itself takes the curl of Eq. (1.11), whereas, we can obtain the so-called Helmholtz equation:

$$(\nabla^2 + \alpha^2)\mathbf{B} = 0, \quad (2.11)$$

where  $\mathbf{B}$  itself satisfies the Equation (2.11). This subset is very important because it can give us a general solution to understand the current in the solar atmosphere [Gary, 1989], either using Fourier series expansions or Green's functions for the magnetic field extrapolation.

To extrapolate the PF magnetic fields at every moment of time, we employed the LFFF IDL extrapolation code from [www.heliodocs.com](http://www.heliodocs.com)<sup>7</sup>, which is based on the paper of Gary [1989]. Actually, we set the  $\alpha$  parameter equal to zero, and, this is the way that we can apply the LFFF code as a PF extrapolation. The code itself uses Fourier series expansions.

### NLFFF extrapolation

In the past few decades, several methods have been developed to compute the NLFFF in the solar atmosphere. In this work, we apply the *direct boundary*

---

<sup>6</sup>YAFTA is available from <http://solarmuri.ssl.berkeley.edu/?welsch/public/software/YAFTA>

<sup>7</sup>[http://www.heliodocs.com/php/xdoc\\_print.php?file=SSW/packages/spvm/idl/bff/bff.pro](http://www.heliodocs.com/php/xdoc_print.php?file=SSW/packages/spvm/idl/bff/bff.pro)

*integral formulation for nonlinear force-free magnetic field* by Yan and Li [2006]. The predecessor of the applied NLFFF extrapolation was the so-called boundary integral method, which was developed first by Yan and Sakurai [2000].

The applied boundary element methods itself use the Green's function to reformulate the NLFFF problem. The nonlinear integral equations have to be carried out over the full domain, but the adopted NLFFF method allows to evaluate the magnetic field at every arbitrary point from the boundary data without having to compute it previously in the entire domain. The method itself is considering the half-space above the lower boundary with vanishing magnetic field at infinity. The solution can be obtained at a given point  $i$  inside the volume  $V$  and for the boundary magnetic field values ( $\mathbf{B}_0$ ) on  $\Gamma = \partial V$ , if we employ the following equation:

$$c_i \mathbf{B}_i = \oint_{\Gamma} \left( \mathbf{Y} \frac{\partial \mathbf{B}}{\partial n} - \frac{\partial \mathbf{Y}}{\partial n} \mathbf{B}_0 \right) d\Gamma \quad (2.12)$$

with  $c_i=1$  for points in the volume and  $c_i=1/2$  for boundary points. The  $\mathbf{Y}$ , in Eq. (2.12), is a kernel function which depends on  $\mathbf{B}$ .

Here, as a boundary condition in the photosphere, we use the Space Weather HMI Active Region Patches (SHARP) data [for details see Bobra et al., 2014] because the applied method requires the three vector magnetic field measurements at the boundary as input. The SHARP data are cut-outs from the HMI full-disk images with no coordinate change or interpolation. The SHARP data series provide maps in patches that encompass automatically tracked magnetic concentrations during their disk transit; map quantities include the photospheric vector magnetic field, Doppler velocity measurement, continuum intensity, and LOS magnetic field. SHARP data are available at [jsoc.stanford.edu](http://jsoc.stanford.edu).

### Identification of the $\delta$ -spot of an AR

After the magnetic field extrapolation steps are carried out, we need to identify the  $\delta$ -spot(s) of the selected ARs for the  $WG_M$  method. This step is based on the idea that the  $\delta$ -type sunspots themselves are well-identified and traceable. Also, they are the most probable places for the flare onsets as discussed in Sec. 1.3.

In order to find a  $\delta$ -spot, we adopt and apply the automatic PIL recognition program developed by Cui et al. [2006]. The program first computes

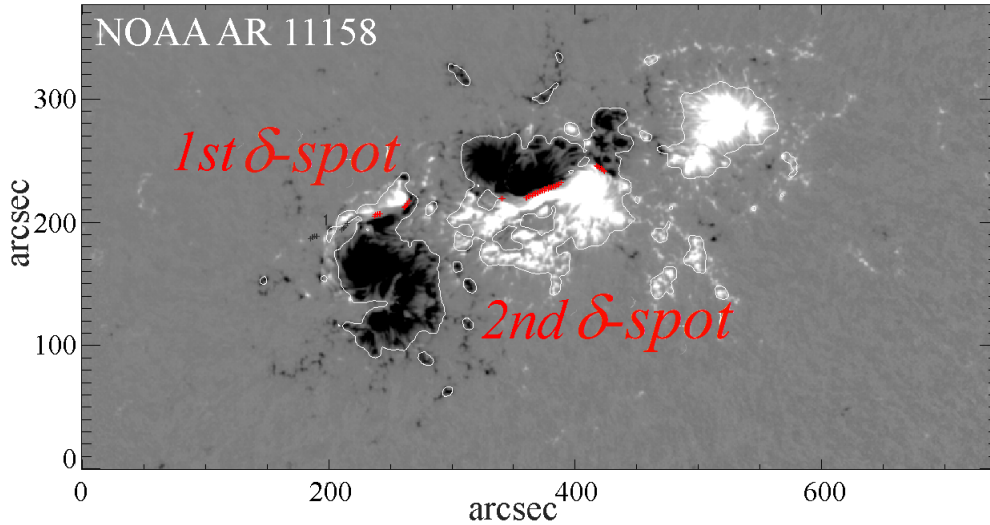


Figure 2.12: Snapshot showing the identified  $\delta$ -spots of NOAA 11158 with the associated the LOS magnetogram. The red-dotted lines are the automatically identified PILs of the AR. The white-counter areas show where the magnetic field is larger than  $|150|$  G.

the transverse component of the magnetic field deduced by the PF with the boundary condition of the LOS magnetic field. Next, the program select pixels, based on whether the strength of the deduced transverse component of the magnetic field is larger than  $|150|$  G. Also, the program identifies pixels where the horizontal gradient of the longitudinal magnetic field is larger than  $|50|$  G/Mm. Finally, the program contours up the area where the magnetic threshold value is greater than  $2\sigma$ . As we can see, e.g. in Fig. 2.12, the contoured area with PIL(s) become the so-called  $\delta$ -spot where, finally, the  $WG_M$  method is applicable for further analysis. In the 3D analyses, we work with 95% confidence interval to construct the necessary input data catalogue applicable for the  $WG_M$  method, therefore, the  $\pm 2.5\%$  error in the 3D studies is negligible when compared to the error of  $\pm 15\%$  in the photosphere.

At the end of this Chapter, we would like to mention that all the adopted numerical codes and the solar catalogues were written and developed by others, who shared these useful resources and assisted with their use. These codes

and programs were identified earlier in this chapter and credit or reference was clearly given. The  $WG_M$  method, which plays the central role throughout the whole thesis, was developed entirely by myself but occasionally improved with the help of my collaborators when applied to various specific solar data catalogues.

## Chapter 3

# Investigation of the pre-flare dynamics of ARs in the photosphere

There is a wide range of eruptions in the solar atmosphere which contribute to space weather, including the major explosions of radiation known as flares. Analysis of joint satellite and ground-based sunspot data allow us to develop reliable precursors to estimate flare onset time and expected flare intensity. This Chapter is a further development of Korsós et al. [2015]. In this work, we apply the  $WG_M$  method across the GOES flare intensity range, from the B-class to the X-class flares. First, we found a logarithmic relationship between the log value of highest flare class intensity (from B- to X-class) of an flaring AR and the maximum value of  $WG_M$  of the 127 ARs investigated. Also, we confirm that the converging-diverging motion of the barycenters of opposite polarities in the vicinity of the polarity inversion line (PIL) plays an important role prior to the flare occurrences at any flare energy scale. The extended statistical sample (i) reaffirms the linear connection between the duration of the converging-diverging motions of barycenters of opposite polarities up to flare onset and (ii) provides a geometric constraint for the location of flare formation around the PIL. These two latter properties may be applied for a better prediction of the flare onset time and location in an AR. Finally, (iii) the method provides a tool to estimate the likelihood of a following flare of the same or larger energy.

## 3.1 Introduction

The origin of the enormous released energy in solar flares was firstly recognised by Giovanelli [1946], Hoyle [1949] and later by Dungey [1953]. It was proposed at an early stage by Sweet [1958] and Parker [1963] that magnetic reconnection may be the underlying physical mechanism of the flare occurrences. A clear understanding of the dynamics and energetics of magnetic reconnection still remains an important goal of solar flare research. Nowadays, a number of specific mechanisms are proposed that may lead to the process of magnetic reconnection, e.g. sunspot rotation [Yan and Qu, 2007, Zhang et al., 2007, Yan et al., 2009, Chandra et al., 2011, Hardersen et al., 2011, Vemareddy et al., 2016] or the shearing motion of the sunspots in the photosphere [Vemareddy et al., 2012] which contribute to helicity and accumulation of magnetic energy of an AR [Török and Kliem, 2003, Démoulin, 2007, Démoulin and Pariat, 2009].

However, if we could determine one or more common reliable pre-flare pattern(s)/feature(s)/behaviour(s) then it would be a profitable way for a future accurate flare prediction method [see, e.g., Georgoulis, 2012, 2013, Barnes et al., 2016, and references therein]. One of a know flare pre-cursor of an AR is the magnetically complicated and highly dynamic  $\delta$ -spot. It is supported by so many observations that the  $\delta$ -type sunspot groups are more likely for flare genesis than bipolar ARs, see e.g. Künzel [1960], Sammis et al. [2000]. The other common feature associated with flaring is the polarity inversion line (PIL). Schrijver [2007] and Louis et al. [2015] observationally proved that the strength of solar flare eruptions is depending on the evolution of the PIL.

The aim of finding a potentially reliable pre-cursors was achieved by Korsós et al. [2015] (K15 therefore, respectively) with the introduction of the  $WG_M$  method (see Section 2.2.1). In this Chapter, we have generalised the application of the  $WG_M$  method in two main ways. First, we have expanded the number of investigated ARs by taking into account not only ARs observed by the SOHO satellite but also those detected by the higher spatial and temporal resolution SDO (Solar Dynamics Observatory) mission. Second, we have extended the analysis to encompass GOES flare classes from as low as B-class to as high as X-class flares. In Section 3.2, we briefly introduce and apply the  $WG_M$  method to the different energetic flares, i.e. between B- and X-class flares. In Section 3.3, we present an extended statistical analysis of these higher number of AR cases and summarise our findings. In Section 3.4, we introduce a simple visualisation of our observational experience of the pre-flare behaviour

of barycentric distance parameter. Finally, we provide discussions of our results and draw conclusions in Section 3.5.

## 3.2 Applying the $WG_M$ method

In 61 flare cases, K15 demonstrated that the  $WG_M$  method could be successfully implemented to help identify typical features preceding flares with classes above M5. Later, in Zheng et al. [2015] and Korsós and Ruderman [2016], the  $WG_M$  method was applied to case studies of lower than M5 flare cases employing the SDO/HMI-Debrecen Data (also known as HMIDD, the continuation of the SDD) catalogue. In the present work, we go now even further by enlarging the observational sample to include 6 ARs with B-class flares, 21 with C-class flares, 13 with M1-M5, and 30 additional ARs with flare events above M5 (see Appendix A.1).

The main reasons for the small number of the weaker than M5 flaring AR in the sample are as follows: (i) When the investigated strongest energetic flare class becomes lower and lower (e.g. it is below M5 or less) then there is an associated decreasing chance of having this low-energy flare class to be the largest flare class of an AR. (ii) In principle, the HMIDD (2011-2014) database would be slightly more suitable to investigate the lower than M5-class flares because the temporal and spatial resolutions of this catalogue are better than that of the SDD. However, in case of these weaker flares, often, we simply cannot identify the two nearby opposite polarities of the AR in the HMIDD catalogue, so, the  $WG_M$  method is not applicable.

By considering lower-energy flares, this expansion of the investigation of flare classes explores whether there could be a common physical mechanism underlying the flare process across all energy scales. However, it must be noted that our method does not give insight into which of the wide range of the proposed flare models available in the literature is applicable. Our method points merely towards the idea that, regardless of the model, there are common pre-flare features identified in photospheric level.

First, let us now demonstrate the technique of applying the  $WG_M$  method to five representative but still arbitrary examples where the flare classes are different. The examples for analysis discussed here are: AR 11429 with five above M5-class flares, AR 11504 produced two low M-class flares; and AR 11281

generated 3 C-class flares as the largest-class flare of the host AR. The 4th one is AR 11967. This AR is interesting because it hosted a known and identified microflare [Yang et al., 2015]. In Yang et al. [2015], observational evidence of X-shape magnetic reconnection before a microflare was introduced. The magnetic reconnection occurred at the topside edge of AR 11967 on February 3, 2014 07:15 UT. There, Yang et al. [2015] found that the X-shape reconnection process builds up of two types of reconnection: (i) First, two anti-parallel loops slowly reconnect, and, after the new loops were formed, they became stacked. This *slow reconnection* continued for several tens of minutes. (ii) The second type of reconnection, the *rapid reconnection*, took only about three minutes. During the *rapid reconnection*, the anti-parallel loops approached each other very quickly and reconnected. After the *rapid reconnection*, the former anti-parallel loops disappeared and new loops formed separately. Finally, AR 11495 is a typical example for the non-flaring AR.

The resulting diagrams of the  $WG_M$  analysis of ARs 11429, 11504, 11281, 11967 and 11495 are shown in Figs. 3.1, 3.2, 3.3, 3.4 and 3.5, respectively. In Figs. 3.1a– 3.5a, we depict the pre- and post-flare evolution of  $WG_M$  (top panel) and we also plot the distance ( $D_{pn}$ ) between the barycentres of opposite polarities as a function of time (middle panel). In the top panel of Figs. 3.1a– 3.5a, the corresponding pre-flare behaviour of the  $WG_M$  parameter is indicated by aqua "inverted V-shape", where a peak corresponds to a follow-up flare. In the middle panel of Figs. 3.1a– 3.5a, the relevant pre-flare behaviour of the  $D_{pn}$  parameter is marked with red parabolic curves. In the bottom panel of Figs. 3.1a– 3.5a, we show the temporal variation of the unsigned magnetic flux ( $\Phi$ ) in  $\delta$ -spot. Figures 3.1b– 3.3b and Fig. 3.5b show the investigated ARs in their white-light appearance (upper panel) and the corresponding magnetogram (bottom panel). The  $\delta$ -spot of each AR is encircled by the red ellipses indicating the region of interest where the  $WG_M$ ,  $D_{pn}$  and  $\Phi$  are also calculated by Equation (2.9) according to the Sec. 2.2.3. Furthermore, we also quantify the important data for the pre-flare analyses, as given in Table 3.1, accordingly to step 5 of Section 2.2.3.

### 3.2.1 Example for intensive X- and M-class flare case

Let us first investigate the case where the largest intensity flare class was a strong X- or M-class. AR 11429 produced three powerful X-class and two stronger M-class flares between from 4th to 12th of March, 2012. In Fig. 3.1a, we can

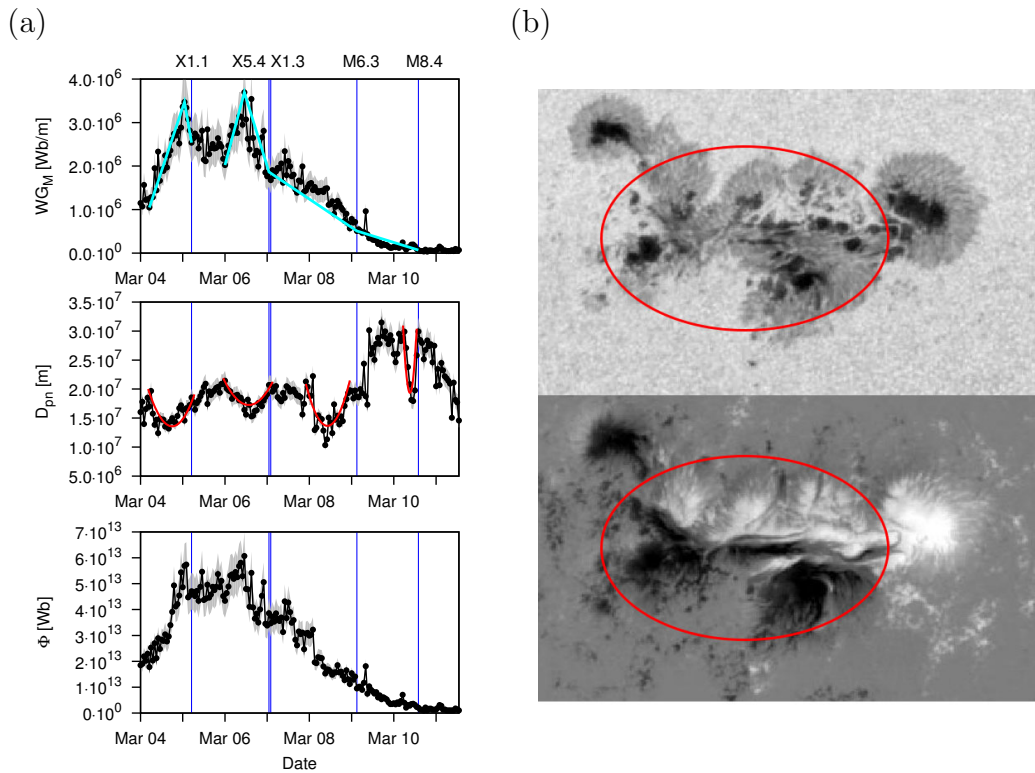


Figure 3.1: (a): The top panel shows the  $WG_M$ , the middle panel plots the distance parameter between the barycentres, and the bottom panel is a plot of the associated unsigned magnetic flux as a function of time. The investigated flare onsets are indicated by (blue) vertical lines. Note, the pre-flare behaviour of the  $WG_M$  parameter is indicated by aqua "inverted V-shape". The U-shapes (red parabolae) in the middle panel are another key flare precursors features of the  $WG_M$  method. The error is marked with shaded grey. (b): Top panel: Intensity snapshot at 10:58 on 7 March 2012. Bottom panel: Magnetogram at 10:58 on 7 March 2012.

observe firstly the rising phase of  $WG_M$  to its maximum value ( $WG_M^{max}=3.5\cdot 10^6$  Wb/m). After, the  $WG_M$  has a decreases phase where the X1.1-class flare occurs on 05/03/2012 at 04:30. Next, about 19 hrs later, after the first maximum value of the  $WG_M$ , one finds another rising phase and the associated  $WG_M^{max}$ , followed again, during the decreasing phase with the series of X5.4, X1.3, M6.3, and M8.4 energetic flares.

Furthermore, we note that as we track the evolution of the  $D_{pn}$  parameter in time, we can clearly see the duration of converging and diverging motion of the area-weighted barycenters of opposite polarities before the X1.1, and, the second duration of converging and diverging motion for the series of the subsequent X5.4 and X1.3 flares. Two further individual converging-diverging motions appear before the M6.3 and M8.4 intensity flares. In fact, all required pre-flare behaviours of  $WG_M$  and of the  $D_{pn}$  can be classified as true precursors because they all satisfied the given criteria in step 5a of Section 2.2.3, see Table 3.1.

Next, we investigate the percentage of the decrease of the  $WG_M$  to the flare onset. This percentage is a mere 27% when the X1.1-class flare occurred, so more flare(s) would be expected. In Figure 3.1a, we can see that after the second maximum of  $WG_M$  during the decreasing phase more X- and M-class flares happened indeed. After the second maximum value of the  $WG_M$ , in the case of the X5.4-class flare, the percentage decrease is 48% and, again, more flares occurred. An X1.6-class flare appears after the X5.4-flare and the associated percentage of decreasing is 52%. Based on the statistical investigation in K15, this is the percentage (see Section 2.2.3) whereupon we would not expect further X-class flare, which indeed did not happen. The remaining two observed stronger flares examined here were M-class (M6.3 and M8.4). Here, we also would like point out that each of these two M-class flares have a pre-flare converging-diverging motion. So, the converging-diverging motion could be a strong indicator for a flare occurrence.

### 3.2.2 Example for weak M-class flare case

Let us now investigate the case where the largest intensity flare class was a weak M-class. AR 11504 produced an M1.2 flare on June 13, 2012 13:17 UT and a further M1.9 flare on June 14, 2012 14:35 UT. In Figure 3.2a, we see that the  $WG_M$  increases to a maximum value ( $WG_M^{max}=0.55\cdot 10^6$  Wb/m), followed by a

less steep decrease which ends with an M1.2 ( $WG_M^{flare}=0.35\cdot 10^6$  Wb/m) flare and is succeeded by another M1.9 ( $WG_M^{flare}=0.23\cdot 10^6$  Wb/m) energetic flare (top panel). The conditions specified by step 5a of Section 2.2.3 are satisfied by the pre-flare behaviour of the  $WG_M$ , therefore we can dismiss the idea that this behaviour is unconnected to the flare. Moreover, the percentage difference ( $WG_M^{\%}$ ) is only 36% until the first flare, which is less than 42% (as defined by the criterion given by K15), therefore we do expect more flare(s) to follow, which did indeed happen. After the second flare,  $WG_M^{\%}$  is 58%, so further flares were not expected.

Regarding the  $D_{pn}$  parameter, the two converging-diverging phases are evident. The first one is before the M1.2 flare where  $T_C$  is 9 hrs and  $T_{D+F}$  is 25 hrs. The second one occurred before the M1.9 flare where  $T_C$  is 14 hrs and  $T_{D+F}$  is 19 hrs. It is worth mentioning that the two converging phases of the barycenters had a duration longer than 4 hrs; the relative gradient of the first decreasing phase is 39% and for the second one it is 44%.

### 3.2.3 Example for C-class flare case

Let us now introduce a representative example of the analysis of a C-class flare by investigating AR 11281. This AR was the cradle to the following 3 C-class flares: C1.8 on September 2, 2011 15:16 UT, C2.4 and C1.2 on September 3, 2011 07:56 and 20:10 UT, respectively.

In Fig. 3.3a, we recognise the following pre-flare properties of the  $WG_M$  and the distance: (i) The rising phase and a maximum value of the  $WG_M$  ( $WG_M^{max}=0.78\cdot 10^6$  Wb/m) is followed by a less steep decrease which ends with C1.8 ( $WG_M^{flare}=0.45\cdot 10^6$  Wb/m), C2.4 ( $WG_M^{flare}=0.51\cdot 10^6$  Wb/m) and after that with the C1.2 ( $WG_M^{flare}=0.36\cdot 10^6$  Wb/m) energetic flares. The conditions of point 5a of Section 2.2.3 are satisfied, therefore the pre-flare behaviour can be confidently attributed to the flare. (ii) The characteristic converging and the diverging features of the barycentric distance prior to the first C-class flare are also evident. The duration of the converging phase of the distance is 13 hrs and the gradient is 26%. The first flare occurred 30 hrs later, measured from the moment of the closest position of the two opposite polarity barycenters. The second C-class flare occurred approximately 17 hrs after the first C-class flare. The final C1.2 flare occurred 12 hrs after the second C2.4 flare.

Let us now briefly investigate the percentage difference in the magnitude

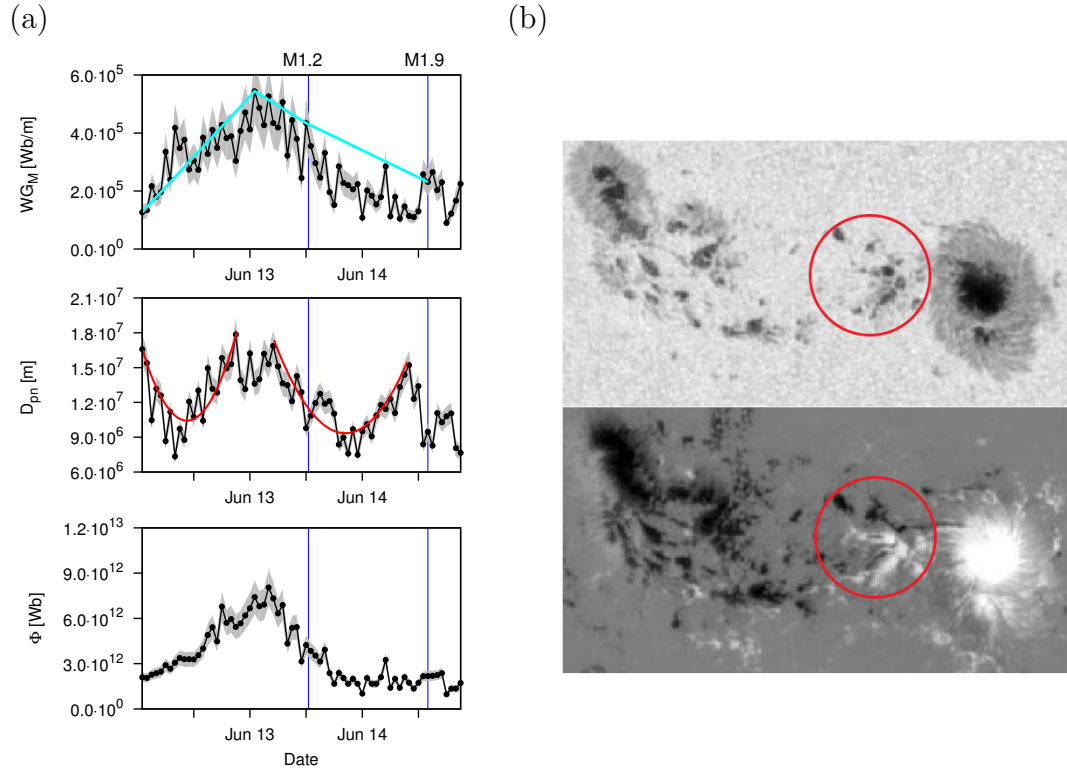


Figure 3.2: (a): Same as Fig. 3.1 but for AR 11504. (b): Top/Bottom panel is intensity/magnetogram at 01:59 on 13 June 2012.

of the  $WG_M$  after reaching its maximum during its descending phase, at the moment of onset of the different flares. The  $WG_M^{\%}$  is 42% at the first C-class flare (C1.8). The  $WG_M^{\%}$  is 35% at the onset of C2.4 and 54% at the last C-class occurrence from the previous  $WG_M^{max}$ . We conclude that one should indeed expect flare(s) after the first C1.8 flare, and that one should not expect further same class flare(s) after the last C-class, which is what happened. Because there was only one clear U-shape flare precursor, we could not say anything about how many same-class flares will follow the first C flare.

### 3.2.4 Example for microflare case

We analysed the same area in a part of the SDO/HMI line-of-sight magnetograms than that of Yang et al. [2015] (see Figure 3.4b). In Figure 3.4a, one

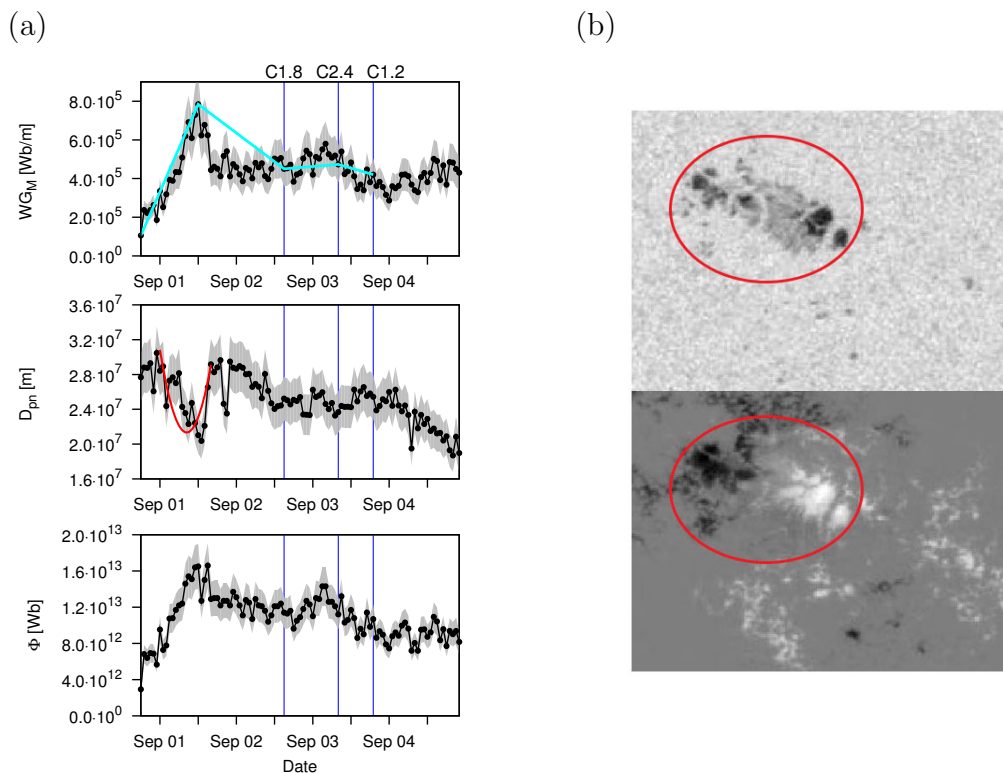


Figure 3.3: (a): Representative example for applying the  $WG_M$  method to GOES C-class flares in AR 11281. (b): Top/Bottom panel is intensity/magnetogram at 00:59 on 03 September 2011.

can indeed recognise the increasing and decreasing phase of the  $WG_M$  before the microflare. The maximum value of the  $WG_M$  is  $0.65 \cdot 10^6$  Wb/m and the value of the  $WG_M$  at flare onset is  $0.38 \cdot 10^6$  Wb/m. The  $WG_M^{\%}$  is 42% after the maximum of the  $WG_M$ . Unfortunately, we cannot say whether a further flare occurred because we do not have any later observations from this area. Next, the converging and diverging phases of the distance are also identifiable: we emphasise this with a red parabola in the middle panel of Fig. 3.4. Here, the duration of the observed  $T_C$  is 7 hrs, with 40% decreasing of the distance and  $T_{D+F}$  is 6 hrs. Based on the required conditions and steps outlined in 1-5 in Section 2.2.3, these two pre-flare behaviours can be classified as true precursors of the microflare.

Note that there may be another typical pre-flare behaviour of the  $WG_M$

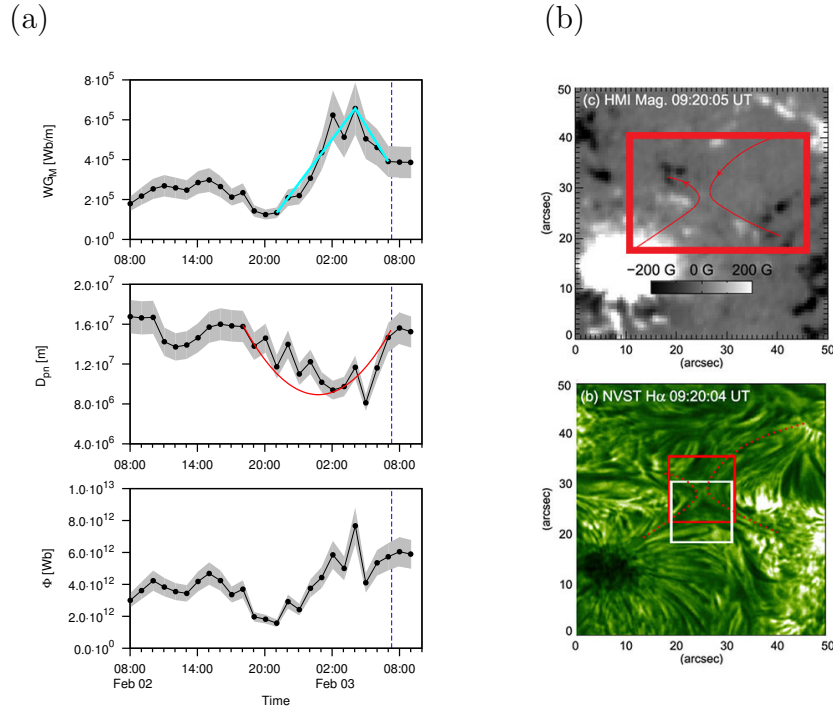


Figure 3.4: (a): Evolution of the pre-flare indicators of the  $WG_M$  method, similar to those of Fig. 3.1 but for a B-class flaring event in AR 11967. The estimated error is marked by the shaded grey envelope. (b): The magnetogram and the EUV pictures are courtesy of Yang et al. [2015].

and distance between 02/02 08:00 and 02/02 18:00. Although, based on 5a of Section 2.2.3, the pre-flare behaviour of the  $WG_M$  could be a precursor, but, the pre-flare behaviour of distance parameter does not qualify as a precursor because the decreasing time is only one hour. In summary, as Fig. 3.4a demonstrates, it is clear that even microflares seem to show the precursors of flaring identified by the horizontal magnetic gradient method.

### 3.2.5 Example for non-flaring case

Finally, there is the very important question: what does happen to  $WG_M$  in non-flaring spot groups? Here, we introduce briefly the non-flaring AR 12495, as an example. In Fig.3.5a, we can see that the  $WG_M$  shows rising and decreasing

phase(s). E.g. if we determine the relative gradient and the elapsed time of the first rising phase, which is highlighted by an aqua line, then we can say that the given limits in step 5a of Section 2.2.3 are satisfied. This is also true in the converging phase case of the  $D_{pn}$ . However, the opposite polarities in the selected cluster do not show any signs of the diverging motion which is necessary for the magnetic reconnection to produce a flare. Therefore there are no flares expected, just like it is confirmed by the observation.

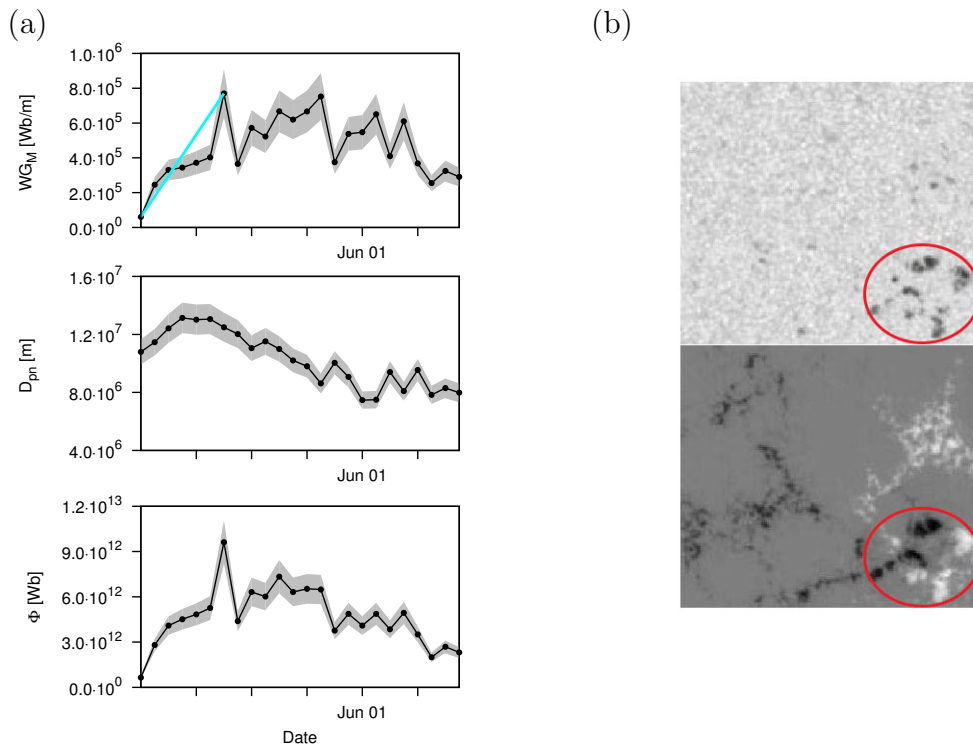


Figure 3.5: (a): Evolution of the pre-flare indicators of the  $WG_M$  method, similar to those of Fig. 3.1 but for a non-flaring event in AR 11495. The estimated error is marked by the shaded grey envelope. (b): Top/Bottom panel is intensity/magnetogram at 01:59 on 01 June 2012.

AR	Flare			$WG_M$			$D_{pn}$			$WG_M^{\%}$
	GOES-class	Date	Time	%	$T_{inc}$ [h]	$WG_M^{max}$ [Wb/m]	%	$T_{Dec}$ [h]	$T_{inc+flare}$ [h]	
11149	X1.1	05/03/2012	04:30	201%	26	$3.5 \cdot 10^6$	32%	10	11	27%
	X5.4	07/03/2012	00:02						7	48%
	X1.3	07/03/2012	01:14				23%	12	8	52%
	M6.3	09/03/2012	03:22	84%	13	$3.7 \cdot 10^6$	33%	11	13	86%
	M8.4	10/03/2012	17:15				37%	5	4	98%
11504	M1.2	13/06/2012	13:17				39%	9	25	36%
	M1.9	14/06/2012	14:35	333%	24	$0.55 \cdot 10^6$	44%	14	19	58%
11281	C1.8	02/09/2011	15:16						30	42%
	C2.4	03/09/2011	07:56	640%	19	$0.78 \cdot 10^6$	26%	13	47	35%
	C1.2	03/09/2011	20:10						59	54%
11967	Micro	03/02/2014	07:15	365%	7	$0.65 \cdot 10^6$	40%	7	6	42%
11495	No flare			780%	7	$0.76 \cdot 10^6$	38%	18		

Table 3.1: The Table includes the name of the AR; intensity and time of the hosted flares; the relative gradient and the elapse time of the rising phase of  $WG_M$ ; value of  $WG_M^{max}$ ; the relative gradient and the elapse time of the  $D_{pn}$  parameter of the converging motion; elapse time from end of the converging motion to the flare onset; and  $WG_M^{\%}$ .

### 3.3 Statistical analyses of $WG_M$ method on the extended data

From the above mentioned five different characteristic but arbitrary examples, we propose that the pre-flare behaviour of  $WG_M$  and the distance of the area-weighted barycentre of opposite polarities maybe present widely for flare classes ranging from B to X, and, may be indispensable before the associated reconnection and/or flaring process. If the conjecture of pre-flare behaviour is proven to even more solar data than the current ensemble of 127 AR cases, this will certainly give us a greater statistical significance for understanding the underlying physics.

Our aim is to analyse the photospheric precursors of flares of a 127 strong set of AR from SDD and HMIDD. First, let us focus on the relationship between the log value of largest intensity flare of an AR ( $\log(I)$ ) and the preceding maximum of the  $WG_M$  (see Fig. 3.6). We have found a logarithmic dependence between  $\log(I)$  and the  $WG_M^{max}$ , what we could use for the estimation of expected largest flare intensity ( $S_{flare}$ ) of the AR:

$$S_{flare} = \log I = a \cdot \log(WG_M^{max}) + b, \quad (3.1)$$

where  $a = 0.58 \text{ [W/m}^2\text{]}/\text{[Wb/m]}$  and  $b = -12.5 \text{ [W/m}^2\text{]}$ .

The correlation coefficient of the fitted logarithmic function is  $R^2 = 0.54$  and is an indicator for a reasonable functional fit to the data. The root mean square error (RMSE) of  $\log(I[\text{W/m}^2])$  is 0.51.

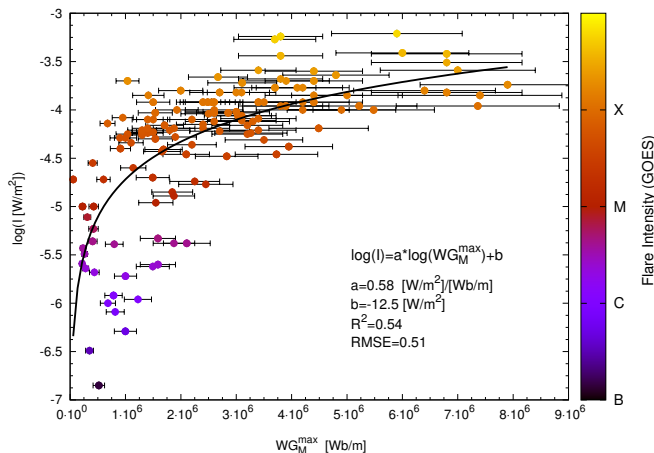


Figure 3.6: The log value of GOES flare intensity ( $\log(I)$ ) as function of the maximum  $WG_M$  ( $WG_M^{max}$ ). The estimated errors are also given in the lower right corner.

Next, the  $WG_M$  method reveals further important connections between the proposed precursors and the associated flare properties. K15 showed that, for large flares, there is a relationship between the duration of the converging motion ( $T_C$ ) and the sum of the duration of the diverging motion of the barycenters of opposite polarities together with the remaining time until flare onset ( $T_{D+F}$ ). The question is then whether this relationship is also valid in the extended data studied here. In other words, it is of interest to establish whether this relationship found for flares above M5 remains for less energetic flares, i.e. below M5 down to C-class or microflares.

Figure 3.7a gives a further insight into the relationship between these physical quantities by plotting the elapsed time between the start of the diverging phase and flare onset as a function of the duration of converging motion. The

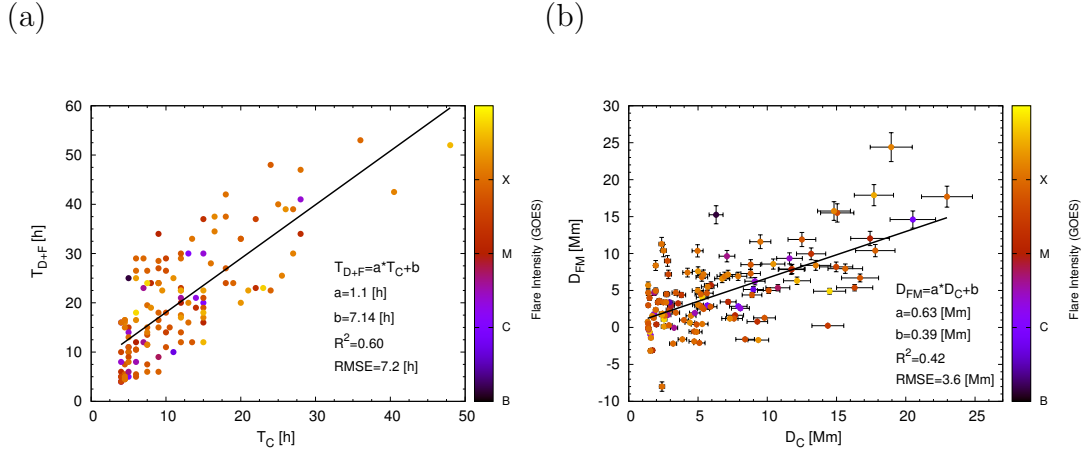


Figure 3.7: (a): Relationship between the durations of converging motion and the duration from the moment of time of closest position up to the first flare onset. (b): Relationship between difference of the distances between the barycenters at the start of the converging phases and at the closest approach ( $D_C$ ) and the distance between the point of closest approach to the position of first flare onset ( $D_{FM}$ ) in photospheric level. The estimated errors are given in the lower right corner.

linear relationship found may possess the capability to estimate an approximate onset time ( $T_{est}$ ) of the associated flare:

$$T_{est} = T_{D+F} = a \cdot T_C + b, \quad (3.2)$$

where  $a = 1.1$  [hr] and  $b = 7.14$  [hr].  $R^2$  of the fitted linear function is 0.60 indicating a moderate correlation. By identifying the start of the diverging phase of the barycenters of opposite polarity, one may predict the time of first flare onset with an estimated error of 7.2 hrs.

We also investigated whether there is a correlation between the duration of converging-diverging motion and the flare intensity, but we were unable to conclude any statistically significant relationship. Figure 3.7b shows the linear correlation between the distance from the starting point of the converging phase to the point of the closest approach ( $D_C$ ) and the distance between the point of closest approach to the position of the first flare onset ( $D_{FM}$ ). The linear fit between  $D_C$  and  $D_{FM}$  may provide another practical tool for estimating the

spatial location of the flare. Here, the  $R^2$  of the linear regression is only 0.42 which means that the correlation is moderate. The RMSE is 3.6 Mm. Again, we cannot report any statistically significant relationship between the distance values and flare intensity. However, it is worth mentioning that the expected onset time and estimated location could both reinforce the search for a more reliable flare forecast.

Last, but not least, we carried out an analysis similar to that of K15 to estimate the corresponding probability thresholds and have found reassuring results confirming the earlier findings. Namely, if the  $WG_M^{\%}$  is over 55%, no further energetic flares are expected; but, if the  $WG_M^{\%}$  is less than  $\sim 40\%$ , a further flare is probable within approximately 18 hrs. If the  $WG_M^{\%}$  is between 40% and 55%, one cannot make a reliable prediction of whether additional flares will/will not take place. In summary, therefore, these properties of the  $WG_M$  method may serve as practical flare watch alert tools across a wide range of the flare energies, the subject of course to the conditions outlined in Section 2.2.3.

### 3.4 Visualisation of pre-flare behaviour of the distance parameter

In this section, inspired by laboratory experiments, we introduce a simple visual interpretation of the observed pre-flare behaviour of the area-weighted barycenters of opposite polarities prior to the reconnection process. The process of magnetic reconnection in the solar atmosphere is mostly studied either using space-based observations or theoretical (e.g. numerical or analytical) modelling. However, laboratory experiments may also yield some interesting insight and impetus. A good example is the series of experimental studies by e.g. Yamada [1999] and Yamada et al. [2010]. Yamada [1999] investigating the physics of magnetic reconnection in a controlled laboratory environment. In these experiments, reconnection is driven by torus-shaped flux cores which contain toroidal and poloidal coil windings. Two types of reconnection modes were found, according to whether the poloidal field coil current increased or decreased. When the poloidal coil current increased then the poloidal fluxes increased as well and plasma was pushed toward the X-point. This reconnection process is called the *push mode*. On the other hand, when the poloidal current decreased, the associated decreasing poloidal flux in the common plasma was pulled back toward

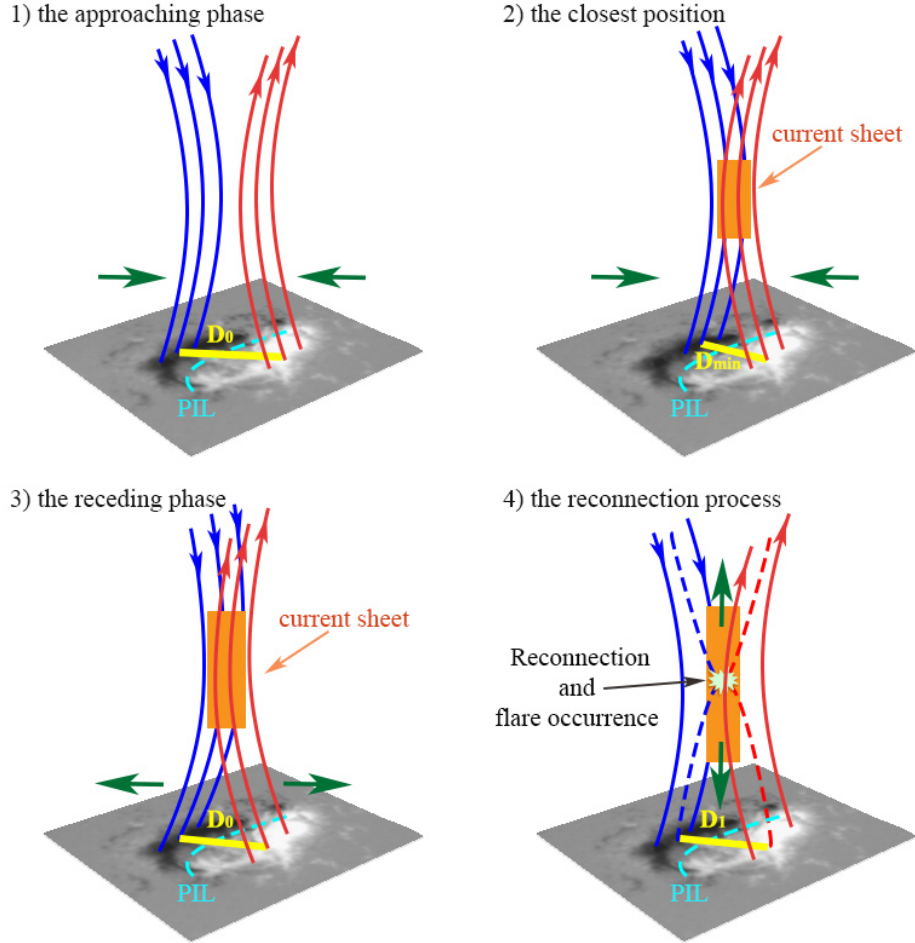


Figure 3.8: Figure demonstrating the process (1) when two opposite polarities of initial barycenter separation distance  $D_0$  are in converging; (2) the two opposite polarities are at their closest and a current sheet starts forming, where  $D_{Min}$  is the minimum distance, with  $D_0 > D_{Min}$ ; (3) the two opposite polarities are in diverging from their closest distance,  $D_{Min}$ , back to  $D_0$ , and the associated current sheet is still developing above the photosphere; (4) reconnection takes place and a flare occurs above the polarity inversion line (PIL). After the distance between the polarity barycentres returns to the initial separation,  $D_0$ , during a further evolution, this distance can now either decrease or increase (i.e.  $D_1 < D_0$  or  $D_1 > D_0$ ).  $D_C = D_0 - D_{Min}$  in Fig. 3.7 (right panel).

the X-point, a reconnection process known as the *pull mode*. They found that the *push mode* occurs more rapidly than the *pull mode*.

Besides the extensive modelling in the literature, the experiments by Yamada et al. [2010] have been a direct drive to solar observational studies of the process of magnetic reconnection. For example, in K15, it was found that the area-weighted barycentres of two opposite magnetic polarities of an AR in the investigated area first approach each other, reach their minimum distance followed by a diverging phase. Most surprisingly, the flare occurrence(s) takes place when the growth of the distance becomes large enough and it approaches the value it had at the beginning of the converging phase (for the actual details see their middle panel of Figs. 3.1–3.5). K15 have shown, using 61 samples from the SOHO (Solar and Heliospheric Observatory) era, that there is never a large flare occurrence when the barycenters are closest. Occasionally, though, smaller so-called precursor flares may take place. The diverging phase was found to continue until the distance increased back to about its original value, i.e. to the level of separation when the converging phase started. The most energetic flares were found to happen after the diverging phase, and for the flare onset time a statistical relationship was established in terms of the duration of the converging/diverging phases (see left-hand side of Fig. 3.7).

In Figure 3.8, we introduce a simple visualisation of the pre-flare behaviour. First, the two opposite magnetic polarities start to converge (panel 1), with an initial barycentric distance of  $D_0$ . When the barycentres reach their closest position (i.e. the separation is  $D_{min}$ ), a thin current sheet begins to form between the opposite polarity field lines (or sheets) but there is no reconnection yet (see panel 2). After the minimum distance stage, the two opposite polarities begin to recede from each other and the separation in photospheric level increases back to the about the same level of separation when the converging process started (see panel 3), with barycentric separation distance of  $\sim D_0$ . The current sheet is still forming during the diverging phase above the photosphere. Finally, reconnection takes place, however, well *after* the moment when the photospheric distance between the area-weighted centres of polarity is at about the same value of what it had at the beginning of the converging phase (see panel 4), with a barycentric distance  $D_1$ . During the process of magnetic reconnection, the magnetic field lines rearrange according to the yet unknown key principles of reconnection in the highly stratified lower solar atmosphere. This rearrangement is accompanied with a sudden energy release, e.g. flare eruption, where the energy of eruption was stored in the stressed magnetic fields.

It has to be noted that a further possible explanation of our empirical finding may be that the actual converging phase is caused by bipolar flux emergence between the two barycenters at the area of the PIL that eventually brings the barycenters closer. Next, the diverging may be caused by the strong shearing motion between the opposite polarities [Ye et al., 2018].

### 3.5 Conclusion

Most flare forecasting models attempt to predict flare probability [see, e.g., Georgoulis, 2012, 2013, Barnes et al., 2016, and references therein]. Many of these flare forecast studies focus on a predictive time window of 6, 12, 24 and 48 hrs [see, e.g., Al-Ghraibah et al., 2015, Benz, 2017, and references therein]. In K15, the concept of *the weighted horizontal magnetic gradient*,  $WG_M$ , was introduced where all umbrae were taken into account in the  $\delta$ -spot for analysis. Initially, the  $WG_M$  method was developed on samples which produced flares above M5-class. In this Chapter, we expanded the statistical sample of flares to be investigated below the M5-class down to B-class microflares, therefore offering an over-arching view of the applicability of the  $WG_M$  method for a wider energy spectrum of flares. An answer is searched for to the question: do smaller flares display the same predictive pre-flare features as their stronger cousins. In the present work, we have outlined the case for the affirmative answer.

Here, we have investigated a total number of 127 ARs which produced flares from as small as B-class energetic flares to the strongest X-class flares and found the two distinct pre-flare patterns regularly: (i) *the pre-flare behaviour pattern of  $WG_M$* : a rising phase, a maximum and a gradual decrease prior to flaring and (ii) *the pre-flare evolutionary pattern of the  $D_{pn}$*  during the converging and diverging motion from the minimum distance value of the area-weighted barycenters of opposite polarities until the flare onset. If one concurrently finds these two pre-flare behaviours, which we identified as useful practical characteristic markers before flare occurrence irrespective of flare class, associated flare(s) does seem to occur. However, if we cannot identify the pre-flare behaviour of the  $D_{pn}$  parameter or the pre-flare behaviour of  $WG_M$  then we could not expect a flare.

After identifying the pre-conditions, we have also investigated the previously discovered three flare prediction tools of K15 with the extended statistical

sample:

- First, we investigated the relationship between the intensity of flares in terms of the  $WG_M^{max}$ . We have always focussed on the largest intensity flare ( $I$ ) which has occurred in the given AR after reaching  $WG_M^{max}$ . By extending the flare samples down to B-class, we found a logarithmic relationship between the  $\log(I)$  of the ARs and  $WG_M^{max}$ . This relationship may provide a tool to estimate the  $\log(I)$  of an expected flare with  $\pm 0.51$  uncertainty from the measured  $WG_M^{max}$ .
- Next, our extended statistical sample confirmed the linear relationship between the duration of the converging motion and the time elapsed from the moment of minimum distance until the flare onset. Therefore, we propose that if one can reliably identify the moment when the barycenter distance begins to grow again then one is also able to estimate the onset time of the flare with  $\pm 7.2$  hrs of uncertainty.
- At the end, we have revisited the estimated probability of further flares during the descending phase of the  $WG_M$  after its maximum. We found encouraging results extending the initial findings of K15 to a wider flare energy range, namely: if the percentage difference ( $WG_M^{\%}$ ) is over 55%, no further energetic flare(s) may be expected; but, if  $WG_M^{\%}$  is less than  $\sim 40\%$ , further flaring is probable within about 18 hrs. The importance of this empirical result is that it could be a further auxiliary tool for indicating the properties of imminent flares.

## Chapter 4

# Applying the weighted horizontal magnetic gradient method to a simulated flaring Active Region

This Chapter is based on Korsós et al. [2018], where we test the  $WG_M$  method on data of a simulated flaring AR. The MHD simulation of solar-like flares was carried out by Chatterjee et al. [2016]. The pre-flare evolution of the  $WG_M$  and the behavior of the distance parameter between the area-weighted barycenters of opposite polarity sunspots at various heights is investigated in the simulated  $\delta$ -type sunspot. Four flares emanated from this sunspot. We found the optimum heights above the photosphere where the flare precursors of the  $WG_M$  method are identifiable prior to each flare. These optimum heights agree reasonably well with the heights of the occurrence of flares identified from the analysis of their thermal and Ohmic heating signatures in the simulation. We also estimate the expected time of the flare onsets from the duration of the approaching-receding motion of the barycenters of opposite polarities before every single flare. The estimated onset time and the actual time of occurrence of each flare are in good agreement at the corresponding optimum heights. This numerical experiment further supports the use of flare precursors based on the  $WG_M$  method.

## 4.1 Introduction of applied simulation

To examine the impact of the two characteristic pre-flare behaviors found by the  $WG_M$  method, we test now the concept of this method on data of a simulated flaring  $\delta$ -spot in 3D. The simulated  $\delta$ -type AR generates a series of flares. The simulation itself was made and published by Chatterjee et al. [2016]. They applied the Pencil MHD Code<sup>1</sup> to carry out the MHD modelling. The Pencil Code is highly modular and can easily be adapted to different types of computational MHD problems. The code itself is centered in a box, with horizontal extents of  $-18 \text{ Mm} < x, y < 18 \text{ Mm}$ , and vertical one of  $-8.5 \text{ Mm} < z < 16.5 \text{ Mm}$ , rotating with a solar-like angular velocity  $\Omega = 2.59 \times 10^{-6} \text{ s}^{-1}$ , making an angle of  $30^\circ$  with the vertical  $z$ -direction. A constant gravity,  $g_z$ , points in the negative  $z$ -direction. The box is resolved using an uniformly spaced grid with  $dx = dy = 96 \text{ km}$  and  $dz = 48 \text{ km}$ .

In the simulation box, the induction equation is solved for the magnetic vector potential,  $\mathbf{A}$ , using the uncurled induction equation,

$$\frac{\partial \mathbf{A}}{\partial t} = \mathbf{U} \times \mathbf{B} - \eta \mathbf{J} + \nabla \Psi, \quad (4.1)$$

where  $\nabla \times \mathbf{A} = \mathbf{B}$  and  $\eta$  denotes molecular magnetic diffusivity. The  $\Psi$  is equal to zero (Weyl gauge) at all times because of Gauge freedom. The initial expression for the components of  $\mathbf{A}$ , corresponding to a horizontal magnetic sheet at  $z_0 = -7.75 \text{ Mm}$  (shown by the white iso-surface in Fig. 4.1) with the magnetic field vector,  $\mathbf{B}$ , strongly oriented in the  $x$ -direction, are given by,

$$A_x = q\varpi\Phi; A_y = -(z - z_0)\Phi; A_z = y\Phi,$$

where,  $\Phi = B_0 R^2 [1 - \exp\{-\varpi^2/R^2\}]/\varpi$  with  $B_0 = 50 \text{ kG}$ ,  $\varpi^2 = (ay)^2 + (z - z_0)^2$  and  $a = 0.1$ . The horizontal extent of the sheet is about  $-3 \text{ Mm} < y < 3 \text{ Mm}$  and the maximum half-width,  $R$ , is  $0.3 \text{ Mm}$  at  $y = 0$ . With this value of  $R$ , the twist parameter,  $q$ , thus is  $0.1$  corresponding to an initially weak negative twist. The ambient magnetic field was introduced in the form of a potential field arcade at  $z > 0$ , also shown in Fig. 4.1. The lower boundary at  $z = -8.5 \text{ Mm}$  is closed and the top boundary at  $z = 16.5 \text{ Mm}$  is open. The  $x$ -boundaries are periodic whereas the  $y$ -boundaries are perfectly conducting walls. Finally, the last equation to close the system is the entropy with temperature  $T$ , height-dependent thermal conductivity  $K$ , and turbulent diffusion,  $\chi_t$ ,

<sup>1</sup><https://github.com/pencil-code/>

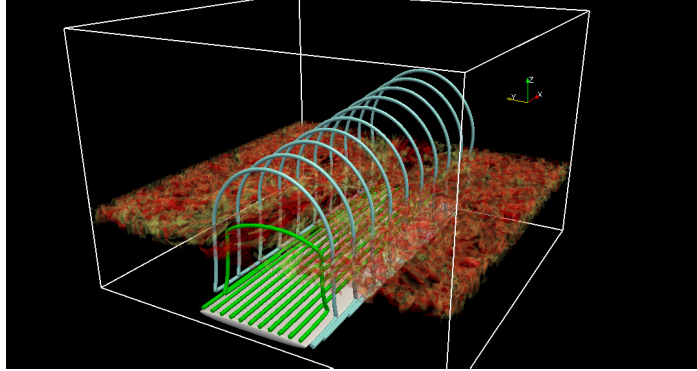


Figure 4.1: The initial state inside the box with a thin magnetic layer represented by the isosurface of  $B\rho^{-1/4}$  (white). Few field lines in this layer are shown in green. Additionally, the ambient (arcade shaped) magnetic field lines are shown in cyan. The location of the photosphere is marked by convective granules represented by isosurfaces of  $v_z$ , with red (yellow) representing upward (downward)  $v_z$ . Credit: Korsós et al. [2018]

$$\rho T \frac{Ds}{Dt} = \nabla \cdot (K \nabla T) + \nabla \cdot (\rho T \chi_t \nabla s) + \eta \mu_0 \mathbf{J}^2 + 2\rho \nu \mathbf{S}^2 - \rho^2 \Lambda(T) + Q_{Cor}, \quad (4.2)$$

where the temperature is related to the sound speed by  $c_s^2 = (c_p - c_v)\gamma T$ . The last two terms in Eq. (4.2) are the radiative cooling and coronal heating terms, respectively.

The height-dependent viscosity includes in the velocity equation,  $\nu/\nu_0 = 1 + f(1 + \tanh\{(z - z_1)/w\})$ , whereas magnetic diffusivity,  $\eta/\eta_0$ , and isotropic thermal conductivity,  $K/K_0$ , vary as  $(\rho_{in}/\rho_0)^{-1/2}$ , with,  $f = 150$ ,  $z_1 = 2$  Mm,  $w = 1.5$  Mm,  $\nu_0 = 2 \times 10^{10} \text{ cm}^2 \text{ s}^{-1}$ ,  $\eta_0 = 10^4 \text{ cm}^2 \text{ s}^{-1}$ ,  $K_0 = 5 \times 10^4 \text{ cm}^2 \text{ s}^{-1}$ , and  $\rho_{in}$  is the initial density. The turbulent diffusion,  $\chi_t = 10^{11} \text{ cm}^2 \text{ s}^{-1}$  for  $z < 0$  and tends to zero above that. Additionally, the hyper-dissipation and shock viscosity are proportional to positive flow convergence, has a maximum over three zones, and is smoothed to second order. A density diffusion of  $10^{11} \text{ cm}^2 \text{ s}^{-1}$  is also included throughout since the plasma- $\beta$  reaches values  $\sim 10^{-3}$ . After a time,  $t = 220$  min in the simulation, Chatterjee et al. [2016] increased the value of density diffusion to  $10^{12} \text{ cm}^2 \text{ s}^{-1}$  and  $f = 300$  to prevent the velocities from going to infinity in the code.

The simulation was ran for 263 min of solar time starting from the initial state shown in Fig. 4.1. It takes about 145 min from the start for the initial magnetic sheet to break up, rise and emerge through the surface like a newly emerging active region (AR). Afterwards, there were four eruptions identified as flares (referred to as  $B_1$ ,  $C_1$ ,  $B_2$  and  $C_2$ ) with magnetic energy released equal to  $3.3 \times 10^{29}$  ergs,  $1.7 \times 10^{30}$  ergs,  $2 \times 10^{29}$  ergs and  $2.3 \times 10^{30}$  ergs at simulation onset times  $t = 167.5$  mins ( $B_1$ ),  $t = 197.2$  min ( $C_1$ ),  $t = 215.03$  mins ( $B_2$ ), and  $t = 240.2$  mins ( $C_2$ ), respectively. Comparing with the estimates made by Isobe et al. [2005] for a C-class flare that occurred on November 16, 2000, Chatterjee et al. [2016] conclude that the first and the third flares can be categorised as GOES B-class, whereas the second and fourth as GOES C-class for the amount of X-ray flux emitted.

	$B_1$	$C_1$	$B_2$	$C_2$
$\delta\mathcal{E}_B$ ( $10^{29}$ ergs)	3.3	17.0	2.0	23.0
Onset time (min)	167.5	197.2	215.03	240.2
Duration (min)	5.0	25.0	13.0	> 23.0
Height range (Mm):				
$\Delta T/\bar{T}(z)$	> 0.6	< 3.24	< 1.28	$\leq 3.24$
Peak of $Q_{FL}$	0.4 – 1.5	2.5	0.3 – 0.5	3.0
$WG_M$	0.3 – 0.4	2.3 – 2.9	0.5	1.2 – 1.8

Table 4.1: Summary of the energy released, onset times, durations and estimated occurrence heights of the four flares.

Table 4.1 shows the onset times, the energy released and estimated reconnection height for each flare. The onset times of the flares are obtained from the temporal evolution of the magnetic energy, see in Fig. 4a of Chatterjee et al. [2016] and Fig. 2 of Korsós et al. [2018]. In order to differentiate the flare onset signal from other fluctuations, Chatterjee et al. [2016] combined the information of change of slope of energy versus time with the first appearance of the flashes of high temperature at three different heights. Also, they used the information available from the time of occurrence of the bipolar reconnection jets in Fig. 4b of Chatterjee et al. [2016] for the  $B_1$ ,  $C_1$  and  $C_2$  flares which match with the times from the energy curves in Fig 4a of the same paper. The

magnetic energy,  $\delta\mathcal{E}_B$ , released during the  $B_2$  flare is calculated to be  $2 \times 10^{29}$  ergs. The  $\delta\mathcal{E}_B$  values for the  $B_1$  flare and the  $C_1$  flare were given in Chatterjee et al. [2016] as well as in Table. 4.1 for completeness. The Poynting flux into the area surrounding the flare also decreases rapidly after  $t = 215.03$  min and becomes close to zero.

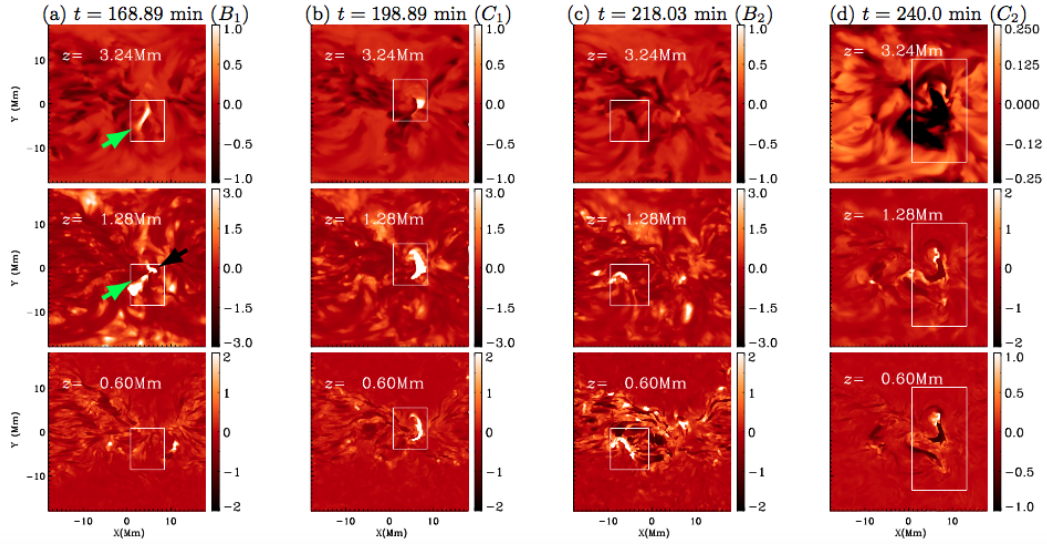


Figure 4.2: (a) The ratio of the local temperature anomaly,  $\Delta T$ , to the horizontal average temperature,  $\bar{T}(z)$ , during the  $B_1$  flare at three different heights as indicated. A value of  $\Delta T/\bar{T}(z) = s$  implies that the local temperature is  $(s + 1) \times \bar{T}(z)$ . The green arrow (left column, top and middle panels) denotes the outward reconnection jet while the black arrow (left column, middle panel) denotes the hot channel of the magnetic flux rope. (b), (c), (d) are similar to (a) but for the  $C_1$ ,  $B_2$  and  $C_2$  flares, respectively. White boxes demarcate the region surrounding the flares. Credit: Korsós et al. [2018]

Fig. 4.2 shows the contours of temperature anomaly, as  $\Delta T$ , relative to the horizontal average, denoted  $\bar{T}(z)$ , at three different heights,  $z = 0.59$  Mm,  $z = 1.28$  Mm and  $z = 3.24$  Mm for all the investigated flares in the simulation. A positive (negative)  $\Delta T$  implies that the local temperature is greater (less) than  $\bar{T}(z)$  of the horizontal layer. It is clear from the temperature indicator that the  $B_2$  flare occurred well below  $z = 3.24$  Mm, whereas some signatures of the  $B_1$  and  $C_1$  flare can still be detected at this height. Moreover, the  $B_2$ ,

$C_1$  and  $C_2$  flares can be detected much lower in the atmosphere, e.g. as low as at  $z = 0.59$  Mm, contrary to  $B_1$  which does not show any brightening at this height at  $t = 168.89$  min. However, from a later time, say  $t = 170.56$  min, the  $B_1$  flare became brighter at the height  $z = 0.59$  Mm. This means that the reconnection for flare  $B_1$  was actually initiated higher up and it took  $\sim 2$  min for the reconnection current sheet to stretch downwards, thus increasing the temperature of the lower layers. Similarly, after  $t = 167$  min, one can also spot the reconnection jet before the appearance of the bright inverse-shaped flux rope. This may mean that reconnection for the  $B_1$  flare was actually initiated somewhere between  $0.59 - 1.28$  Mm. In general, all flares appear bright in terms of  $\Delta T/\bar{T}(z)$  at  $z = 1.28$  Mm. The last flare,  $C_2$ , is most likely a filament eruption as evident from two neighbouring inverse-S shaped dark filamentary structures in the  $\Delta T/\bar{T}(z)$  contour plot at all heights. The evolution and eruption of this filament-like structure is shown in Fig. 6 of Chatterjee et al. [2016]. There, one sees some smaller bright regions surrounding the dark filaments at the heights  $z = 0.59, 1.28$  Mm. A corresponding bright region at  $z = 3.28$  Mm is not so prominent likely because of a large coronal conductivity used in the MHD equations after  $t = 220$  mins.

Chatterjee et al. [2016] used ideal gas thermodynamics in this simulation without solving for detailed radiative transfer and without taking into account the effects of ionisation. Also, in order to keep the simulation stable at low plasma- $\beta$ , they used higher dissipation. All these approximations can make the temperature in the simulation a less reliable indicator. Alternatively, they could estimate the Ohmic heating of field lines above the photospheric height in the simulation using a method similar to the one illustrated in Cheung and DeRosa [2012]. The Ohmic heating term in Eq. (4.2) is given by  $\eta\mu_0\mathbf{J}^2$ . If they wrote an equation for the temperature,  $T$ , instead of for entropy,  $s$ , the Ohmic heating term will be given by,  $\eta\mu_0\mathbf{J}^2/\rho C_v$ . Assuming that the thermal conductivity along magnetic field lines far exceeds the isotropic thermal conductivity in the solar corona they can assign a quantity,  $\tau_{\mathcal{L}}$ , to a line-tied field line  $\mathcal{L}$  where,

$$\tau_{\mathcal{F}} = \frac{\mu_0}{c_v \mathcal{L}} \int_{\mathcal{F}} \frac{\eta \mathbf{J}^2}{\rho} dl.$$

Here,  $c_v$  is the specific heat capacity at constant volume and  $dl$  is an infinitesimal distance along the field line  $\mathcal{F}$  of length  $\mathcal{L}$  between the line-tied ends at the photosphere. Chatterjee et al. [2016] trace about  $10^5$  field lines through all the points on the photosphere where  $B_z > 200$  G and assign a unique

$\tau_{\mathcal{F}}$  to all the field lines. If the field line crosses any of the side boundaries or the top boundary then they set  $\tau_{\mathcal{F}} = 0$  for that field line. Now, any magnetic field line will traverse through many grid cells in the computational domain. For, each grid cell the increment in the value of Ohmic heating denoted is defined,  $Q_{\text{FL}}(x, y, z)$ , by,

$$dQ_{\text{FL}} = \tau_{\mathcal{F}} dx dy.$$

Hence, the net heating due to field lines,  $Q_{\text{FL}}$ , for any grid cell can be the sum of  $\tau_{\mathcal{F}}$  for all field lines passing through that cell. A region like a current sheet or a flux rope can appear bright in  $Q_{\text{FL}}$  as all field lines passing through it carry large currents and so, have a large value of  $\tau_{\mathcal{F}}$ .

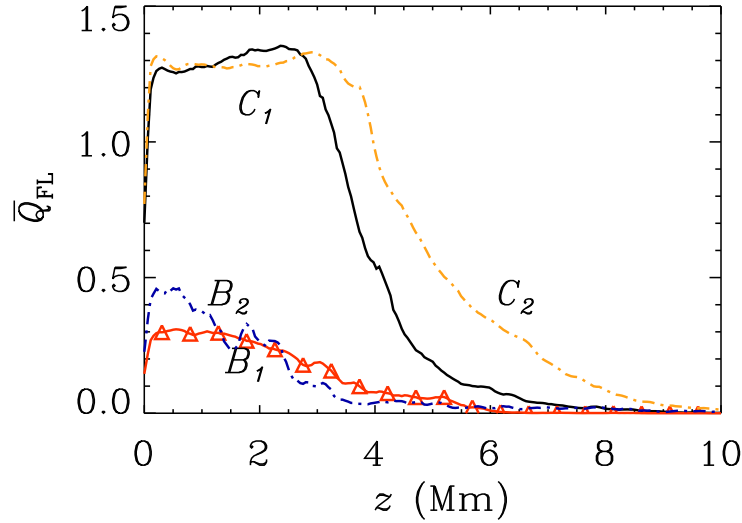


Figure 4.3:  $\bar{Q}_{\text{FL}}$  obtained by integrating the Ohmic heating,  $Q_{\text{FL}}$  for all the four flares. Credit: Korsós et al. [2018]

Fig. 4.3 shows the heating function,  $\bar{Q}_{\text{FL}}(z)$  as a function of  $z$ , obtained by averaging  $Q_{\text{FL}}$  for all the four flares. Moreover, the  $\bar{Q}_{\text{FL}}$  curves were temporally averaged for simulation snapshots between an interval  $\pm 2.8$  mins around the onset time. Just before the onset of any flare when the function  $\bar{Q}_{\text{FL}}$  peaks at a certain height where the flare was likely initiated at that height. For flare  $B_1$ ,

the  $\overline{Q}_{\text{FL}}$  shows a plateau between 0.1 – 2 Mm, whereas for flare  $B_2$ , the clear peak is at 0.5 Mm. Flares  $C_1$  and  $C_2$  also have plateaus between 0.1 – 3 and 0.1 – 4 Mm, respectively. Also, the peaks (of  $Q_{\text{FL}}$ ) for flares  $C_1$  and  $C_2$  appear at heights 2.6 and 3 Mm above the photosphere, respectively. From these results, the flare  $B_2$  was likely initiated at 0.5 Mm whereas flares  $C_1$  at  $\sim 2.6$  Mm and  $C_2$  at  $\sim 3$  Mm, respectively. For flare  $B_1$ , because of the flat plateau without any pronounced peaks, it suggested that it was initiated below the height of 1.5 Mm.

Next, the  $WG_M$  method will now be applied at different heights of the simulation, with the goal of understanding its behavior relative to the derived heights of the flare initiation using Ohmic heating as well as temperature signatures. This spatial information, gained from analysis of this simulation, will be compared with the output of the  $WG_M$  analysis as a function of height in the Sections 4.2– 4.8. Finally, we discuss our results and draw our conclusions in Section 4.4.

## 4.2 Investigation of pre-flare behavior at the different heights

We investigate the pre-flare behavior of the simulated 3D  $\delta$ -type sunspot by the tool put forward in Chapter 3. Before we apply the  $WG_M$  method to the simulation data, we need to appropriately re-scale the hours to minutes time scale. The eruptive events in the simulation happen much faster, i.e. on the time scale of minutes rather than hours like in the real Sun, that is partially a pragmatic approach due to the practical limiting reasons on CPU access. Now, given the linear structure of Equation (3.2), we use  $a = 1.1$  [min] and  $b = 7.14$  [min] for the onset time estimation. In Equation (3.1), we do not need to re-scale anything because the energy of the simulated four flares are comparable with the C and B GOES flare intensity classes.

Let us now apply the  $WG_M$  method to the numerically simulated flaring  $\delta$ -spot. We calculate the  $WG_M$  in the entire  $\delta$ -spot like in the case of real sunspot data. The investigation in terms of the pre-flare dynamics starts from  $t=145.22$  min, i.e. from the moment when the simulated AR finally emerged through the photosphere and developed into a complex set of loops. From the simulation data we know, e.g. from constructing the temperature contour and

$\overline{Q}_{\text{FL}}$  plots at various heights, that all the flares occurred between 0.3–3.25 Mm in height (see Fig. 4.2a–d and Fig. 4.3 for  $B_1$ ,  $C_1$ ,  $B_2$  and  $C_2$  flares). These inspire us to extend and apply the flare precursor identification analysis in the solar atmosphere *as a function of height*, from the photosphere to as high as  $z = 3.6$  Mm. The aim is now to demonstrate that the flare precursor patterns may appear earlier in time, when applied to data higher in the lower solar atmosphere, as compared to its counterpart from photospheric analysis.

Let us now track the temporal variation of  $WG_M$ , distance of the area-weighted barycentres of the opposite polarities ( $D_{pn}$ ) and the unsigned magnetic flux ( $\Phi$ ) at the different heights in the lower solar atmosphere similar to the analysis carried out earlier with observed data at the photosphere, demonstrated in Chapter 3. The aqua ”inverted V-shape” points out the pre-flare behavior of the  $WG_M$  in the top panels of Figs. 4.4–4.7. The duration of approaching-receding motion of the area-weighted barycenters of opposite polarities is highlighted by a red parabolic curve in the middle panels of Figs. 4.4–4.7.

### 4.2.1 At the photosphere

From inspecting Fig. 4.4, we recognise the pre-flare patterns of  $WG_M$  (aided by aqua ”inverted V-shape” in Fig. 4.4) as follows: a rising phase, a first maximum value of the flux gradient (at 158.89 min, i.e a peak in the aqua line preceding the first flare) that is followed by a gradual decrease which culminates in the  $B_1$  flare at  $t = 167.5$  min. About 8 mins later, after the first  $WG_M^{max}$ , one finds another (now a much more pronounced) steep rise and the associated high maximum value of the flux gradient (second aqua peak). This peak is followed, again, by a gradual decrease which ends with the  $C_1$  energy flare. Another 10 mins later, from the  $C_1$  flare, the  $WG_M$  shows again a pre-flare behavior before the  $C_2$  flare (i.e. third aqua peak). Unfortunately, in the case of the  $B_2$  event (for ease and convenience marked as vertical dashed line) we cannot observe the complete pre-flare behavior of the  $WG_M$ . All can be said about it is that the  $B_2$  flare happened during the rising phase of the  $WG_M$  before the  $C_2$  flare without precursor signature in the data.

Let us now follow the evolution of the  $D_{pn}$  parameter in time in the data at photospheric level (middle panel of Fig. 4.4). We can see the mark of approaching-receding motion of the  $D_{pn}$  before the  $B_1$  flare (indicated by the red parabola in Fig. 4.4). In the case of subsequent  $C_1$ ,  $B_2$  and  $C_2$  flares, however,

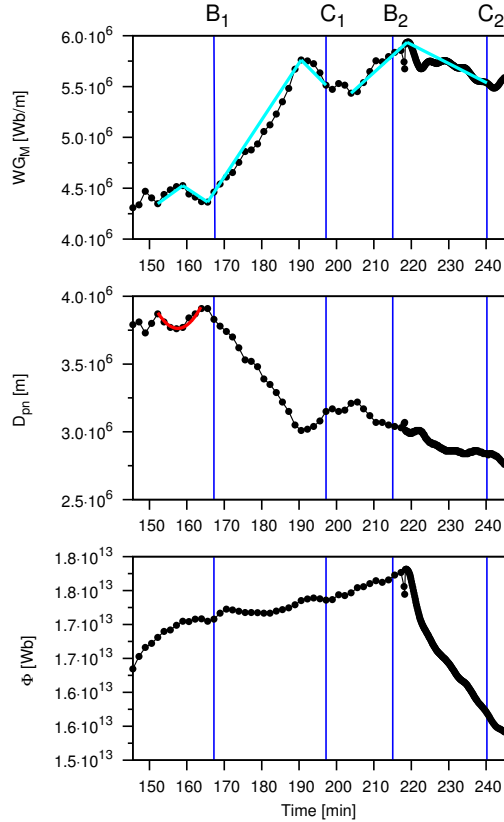


Figure 4.4: Evolution of various pre-flare indicators, applied to the simulation data. The  $x$ -axis is time [min]. (a) The upper panel shows the temporal variation of  $WG_M$ . The pre-flare behavior of the  $WG_M$  is indicated by aqua "inverted V-shape", where a peak corresponds to a follow-up flare. (b) Middle panel demonstrates the evolution of the  $D_{pn}$ . The red curve fit marks the full approaching-receding motion of  $D_{pn}$ . The vertical dashed lines indicate the moments when the flares occurred. Note, however, the flares do not occur at the photosphere (see e.g. Fig.4.3 to determine the height range for the flare location). (c) The bottom panel shows the evolution of the  $\Phi$ .

we cannot identify the complete pre-flare behaviors of the  $D_{pn}$  parameter using the simulation data available at photospheric level. For example, after reaching the minimum value during the approaching phase at  $\sim 190$  mins, the value of  $D_{pn}$  did not increase enough during the receding phase to regain its (about the same value) at the start of the approaching, which is a prerequisite for applying the  $WG_M$  method successfully.

We conclude, at this stage, that using the photospheric data, only the  $B_1$  flare had the required concurrent qualifying precursors for indicating the potential development of a flare. Although there are tempting precursors for the  $C_1$  flare, the  $D_{pn}$  parameter does not show the required full parabolic U-shape.

### 4.2.2 At 0.59 Mm level in the low chromosphere

In Fig. 4.5, we show the evolution of the three pre-flare parameters ( $WG_M$ ,  $D_{pn}$  and  $\Phi$ ) in the low chromosphere. Further, signatures of first point to note is that: one more increasing and decreasing phase of  $WG_M$  starts to appear before the  $B_2$  flare, starting from  $\sim 196$  mins. The two additional approaching and receding phases of the  $D_{pn}$  parameter become identifiable, before the  $B_2$  and  $C_2$  flares, respectively. At this level of height, we found (though with some level of fluctuations present) the characteristic increasing and decreasing phase of  $WG_M$  prior to each of these flares (see the aiding aqua lines for marking the four peaks). Also, we observe the signatures of the approaching-receding motion between the area-weighted barycenters of opposite polarities prior to  $B_1$ ,  $B_2$  and  $C_2$  flares (marked with three red U-shapes).

We conclude, at this stage using data at 0.59 Mm, that the precursors became more pronounced for the  $B_1$  flare; for  $B_2$  we still cannot be fully certain that a flare may develop as the  $D_{pn}$  parameter does not satisfy the minimum 4 mins decrease criteria of U-shape. Although there are tempting precursors for the  $C_1$  flare, the  $D_{pn}$  parameter does not show the required full parabolic U-shape.

### 4.2.3 At 1.28 Mm in middle chromosphere

When one ascends further up in the solar atmosphere and reaches the 1.28 Mm level, one sees changes in the evolution of the  $WG_M$ ,  $D_{pn}$  and the  $\Phi$ . It is found,

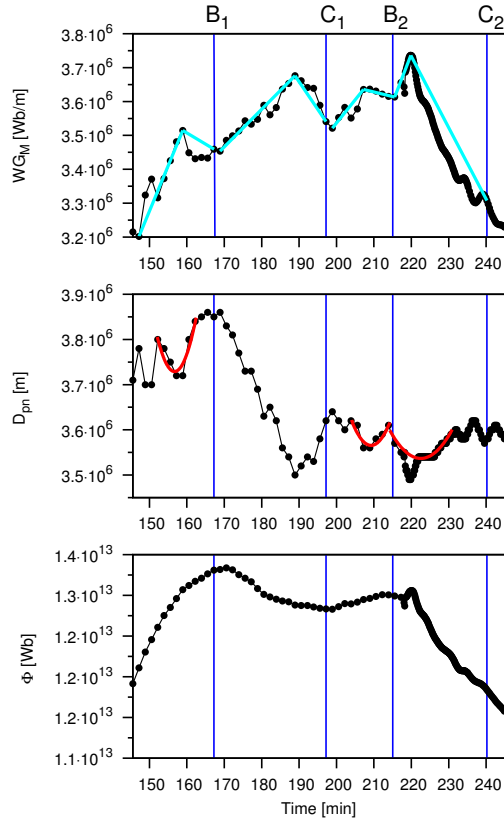


Figure 4.5: The diagrams show the evolution of the same physical parameters for the artificial AR as of Fig. 4.4 but at the height of 0.59 Mm above the photosphere.

at this height, that the pre-flare behaviour of  $WG_M$  is difficult to recognise prior to  $B_1$ ,  $C_1$ ,  $B_2$  and  $C_2$  flares but they are there and may qualify as precursors.

In Fig. 4.6, before the  $C_1$  flare, the duration of the approaching-receding motion of the  $D_{pm}$  starts to form between 170 and 184 min but this interval will become longer in the higher solar atmosphere. The two approaching-receding phases of the  $D_{pm}$  identified at the 0.59 Mm level (for  $B_2$ ,  $C_2$ ) merge when ascending further to 1.28 Mm. It is also found, at this height, that the indicator of approaching-receding motion of the  $B_1$  flare has actually started to disappear. The decrease is only 3.32 mins before the  $B_1$  which does not satisfy the threshold

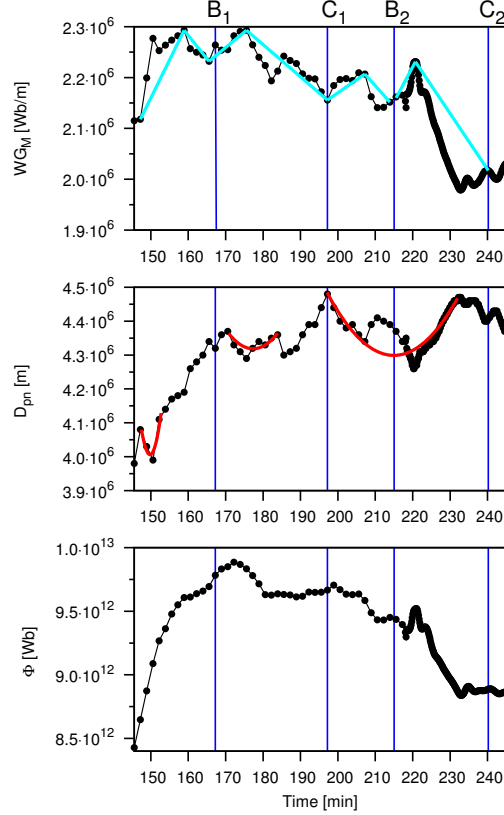


Figure 4.6: Same as Fig. 4.4 but at the height of 1.28 Mm above the photosphere. Here, the pre-flare evolution stages of  $WG_M$  for the first two flares are not visible, there is indication only for the second C-class flare.

criteria of minimum of 4 mins decrease.

#### 4.2.4 At 3.24 Mm above the photosphere

As one ascends even higher, one finds that the evolution of  $WG_M$  and  $D_{pm}$  changes remarkably (see Fig. 4.7) when compared to their behaviour at the photosphere (Fig. 4.4). Here, we also note that the pre-flare behaviour of  $WG_M$  is recognisable between 145.56 and 161 mins which could link to  $B_1$  but we avoid the analysis of B-class flares at this level based on the plateaus of

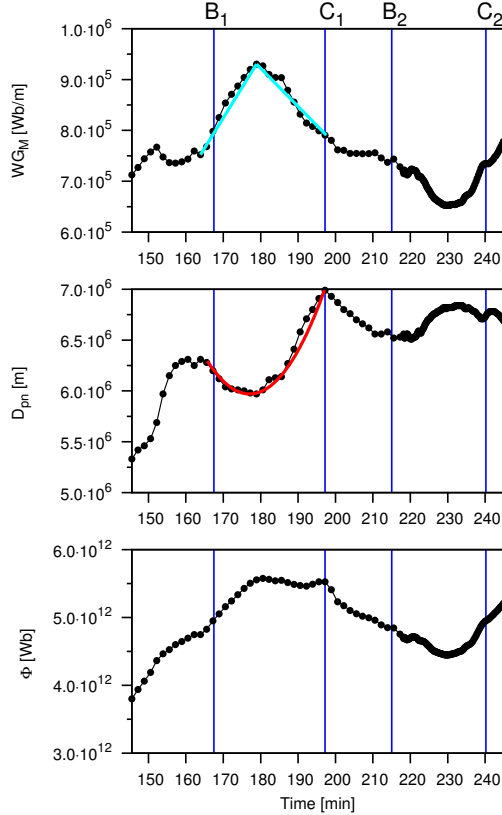


Figure 4.7: Same as Fig. 4.4 but at 3.24 Mm high in the solar atmosphere. The two B-class flares are only marked for completeness, they cannot be confidently identified.

the  $\bar{Q}_{FL}$  during flares shown in the simulations (see Fig. 4.3). We also cannot recognise anymore any meaningful characteristic pre-flare behaviors of the  $D_{pn}$  prior to these two small flares.

In the two C flare cases, when the transition region and the lower corona is reached at this height, we do recognise, however the following properties of the  $WG_M$  and the  $D_{pn}$ : (i) First of all, the steep rise from 164 mins and a high maximum value of the weighted horizontal gradient of the magnetic field is still followed by a less steep decrease prior to  $C_1$  flare (see the aqua, "inverted V-shape"). The  $WG_M$  has only rising phase before the  $C_2$  flare at this height.

(ii) The approaching and the receding characteristic features of the  $D_{pn}$  prior to  $C_1$  flare are also there, but the distance parameter does not comply to be a qualifying criteria before the  $C_2$  flare.

Based on the analysis of data available at the very high end of the lower solar atmosphere (i.e. at 3.24 Mm), we conclude that pre-flare signatures of  $C_1$  can be finally confirmed (as opposed to the cases at lower heights discussed earlier). Signatures of the small B-flares are not clear and neither are they for the  $C_2$  flare.

Finally, similar to observed data of real sunspots, the  $\Phi$  (lower panel Figs. 4.4-4.7) does not show any special behavior to be useful for flare precursor.

### 4.3 Optimum height(s) search for an earlier flare precursor identification

The evolution of the  $WG_M$  and the  $D_{pn}$  are different at various heights, as has been described above. In order to improve the flare precursor capability of the  $WG_M$  method, therefore, we try to identify optimum height(s) in the solar atmosphere. The investigated heights are where the precursor behaviours of the  $WG_M$  and  $D_{pn}$  parameters are identifiable prior to each flare. The optimum height(s) would be where the  $D_{pn}$  parameter would yield the earliest sign of pre-flare behavior in time. Table 4.2 summarises the key parameters for finding the optimum heights.

First, in Fig. 4.8 we plot the variation of the start time of the approaching phase (green lines), the moment of the closest approach (blue lines) and the estimated flare onset time (magenta lines) as a function of height. In Fig. 4.8, the filled square/triangle/circle/star symbols mark the calculated corresponding data of  $B_1/C_1/B_2/C_2$ -class flare. The black vertical lines indicate the onset time of the flares, where the strength of the flare ( $B_1/C_1/B_2/C_2$ ) is labelled on the top axis. The grey strips mark the vertical extent where ohmic heating of the "current carrying" field lines reach plateaus of the  $\bar{Q}_{FL}$  during flares in the simulations (see Fig. 4.3). Most noticeable is that, in general, there are certain heights above the photosphere, where the approaching motions begin earlier and reach the closest point of approach also earlier than at the photosphere or at other heights in the solar atmosphere.

In Fig. 4.8, the start time of the approaching phase (first green line with squares) of the  $B_1$  flare is sooner and it also reaches the moment of the closest approach sooner (first blue line with squares) between heights at 0.3-0.4 Mm than at the photosphere or at any other heights. In the case of the  $B_2$  flare, the optimum height, i.e. having the earliest time of beginning of approach, seems to be 0.5 Mm. Similarly, for the  $C_1$  flare the start time of the approaching phase and moment of the closest approach is earliest between heights 2.3 and 2.9 Mm above the photosphere. We can clearly see that the start time of the approaching phase and the moment of closest approach corresponding to the  $C_2$  flare is earliest between heights 1.2 and 1.8 Mm above the photosphere. This result is rather important: if we are able to identify the optimum height where the moment of start time of the approaching phase, as well as the moment of closest approach, is indeed earlier than at any other heights in the solar atmosphere, then the analysis carried out at this height may (hopefully considerably in practice) improve the capacity of flare precursor capability, e.g. yielding a more accurate flare onset time. Furthermore, it also seems that the optimum height may depend on the energetic flare class. This could be a significant progress if confirmed by observations on a larger database.

Flare	Interval	Optimum height [Mm]	$\overline{Q}_{FL}$ [Mm]	$WG_M^{max}$ $\cdot 10^6$ [Wb/m]	$WG_M^{flare}$ $\cdot 10^6$ [Wb/m]	$S_{flare}$ Class	$T_C$ [min]	$T_{D+F}$ [min]	$T_{est}$ [min]	$WG_M^{\%}$ [%]
$B_1$	Min	0.3	0.1	3.99	3.93	X	3.34	11.94	10.81	1.5%
	Max	0.4	2	3.87	3.80	X	3.34	11.94	10.81	2%
$C_1$	Min	2.3	0.1	1.36	1.18	M	11.60	19.98	19.96	13.2%
	Max	2.9	3	1.05	0.89	M	11.60	19.98	19.96	15.2%
$B_2$	Min	0.5	0.5	3.92	3.92	X	3.34	9.47	10.80	0.1%
	Max									
$C_2$	Min	1.2	0.1	2.23	2.01	M	15.70	25.70	23.64	9.5%
	Max	1.8	4	1.54	1.39	M	16.70	24.70	25.47	10%

Table 4.2: Summary table of the investigated properties of the two B- and two C-class flares at their optimum heights.

In Table 4.2, we list some properties of the flares determined at the minimum and maximum value of their optimum heights and the minimum and maximum height values corresponding the plateaus of the  $\overline{Q}_{FL}$ . Table 4.2 includes the maximum value of the  $WG_M$  ( $WG_M^{max}$ ), value of  $WG_M$  at the flare onset ( $WG_M^{flare}$ ) and the estimated flare GOES-class ( $S_{flare}$ ), duration of the simulated compressing phase ( $T_C$ ) and receding motion until flare onset ( $T_{D+F}$ ),

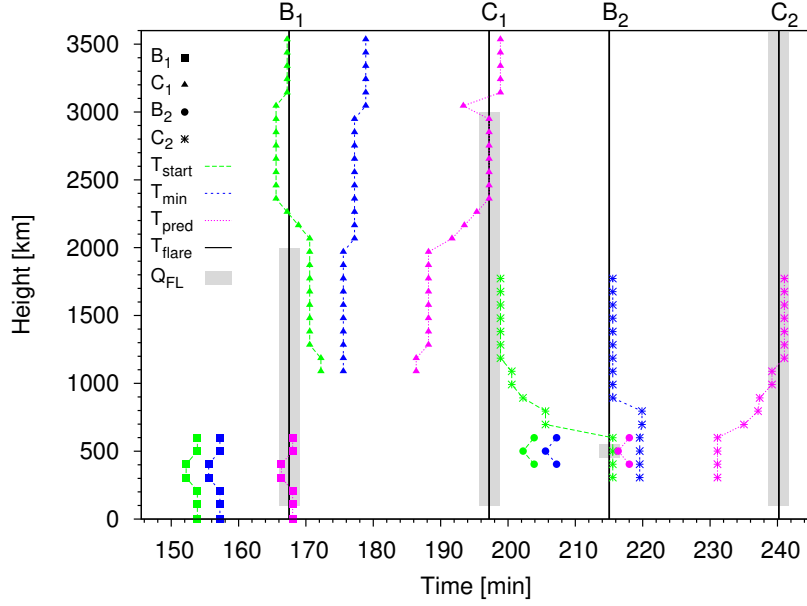


Figure 4.8: The filled square/triangle/circle/stars symbols are associated with  $B_1/C_1/B_2/C_2$ -class flares, respectively. The actual moment of start times of approaching (green lines), times of momentum of the closest approaching point between two barycenters (blue lines) and the estimated flare onset time by Equation (3.2) (magenta lines) are plotted as a function of height. The black vertical lines denote the two B-class and two C-class flares (at 167.5, 215.03, 197.2 and 240.2 min). The grey areas demonstrate the height extent where the ohmic heating of their "current carrying" field lines reach more than 95% of the maximum ( $Q_{FL}$ ) near the onset time of the two B-class and the two C-class flares, respectively.

the estimated flare onset time ( $T_{est}$ ) elapsed from the moment of reaching the closest point during the approaching-receding motion to the flare (computed from Eq. 3.2) and the ratio of maximum value of the  $WG_M$  to the value of the  $WG_M$  at flare onset ( $WG_M^{\%}$ ).

From Table 4.2, we can see that the estimated onset time ( $T_{est}$ ) and the elapsed time of simulated receding motion until flare onset ( $T_{D+F}$ ) are close to each other for the two B- and C-class flares at the optimum heights. First, if we apply  $T_C$  obtained from the first approaching-receding motion of the barycentric distances before the  $B_1$  flare between heights of 0.3 and 0.4 Mm then the time

difference is 1.1 min between  $T_{est}$  and  $T_{D+F}$  (see the values in Table 4.2). The  $C_1$  flare occurred only 0.02 min later than the expected onset time. For the  $B_2$  flare the time difference between the estimated and the observed onset time is 1.33 minutes. The difference between the onset time and the estimated onset time of  $C_2$  is only 1.02-2.06 min depending on the optimum heights. Also, the minimum and maximum values of the optimum heights of  $B_1$ ,  $C_1$ ,  $B_2$  and  $C_2$  flares are in the plateau ranges of the  $\bar{Q}_{FL}$  (see the values in Table 4.2). However, the expected intensity flare classes are over-estimated by the Eq. (3.1). This could be caused by the small number of lower energetic flare class sample in Chapter 3, therefore, Eq. (3.1) does not seem to be applicable to the simulation data.

Last, we investigate the percentage difference ( $WG_M^{\%}$ ) at identified optimum heights. The  $WG_M^{\%}$  does not seem to be applicable to the simulation data, unlike to observational data. The values of  $WG_M^{\%}$  are small which means that one may expect further flare(s) during the decreasing phase of  $WG_M$ , but this is not taking place. So, further investigation may be needed to exploit the applicability of this parameter.

## 4.4 Conclusions

Chatterjee et al. [2016] modelled a  $\delta$ -sunspot feature formed due to the collision of two magnetic regions with opposite polarity arising from the interaction of emerging magnetic flux with stratified convection. The two opposite polarities of the magnetic field are part of the same initial subsurface structure and their collision causes recurring flaring; two B- ( $B_1$  and  $B_2$ ) and two C- ( $C_1$  and  $C_2$ ) classes.

In this core of a flaring simulated AR, we applied the  $WG_M$  method, put forward in Chapter 3 in the context of identifying the introduced flare precursors, tracked the temporal evolution of the  $WG_M$ , the variation of  $D_{pn}$  and  $\Phi$  at different heights in the model solar atmosphere from photosphere up to 3.6 Mm, at stepping intervals of 100 km in height. During the analyses, we found that the  $WG_M$  method does seem to work for the simulated low energy flare events, as seen in this case study mimicking the evolution of an AR. Our initial results are encouraging because we do observe very similar pre-flare behavior of the  $WG_M$  and the  $D_{pn}$  parameter between the polarity barycenters in real sunspot data discussed in Chapter 3 as well, indicating that the predictive temporal

behavior of these parameters may indeed be an intrinsic feature of the physical processes preceding flare onset. The fact, that the application of the  $WG_M$  method gives similar precursors for observed (GOES B- C-, M- and X-class) flares as well as the simulated (B- and C-class) flares also gives us confidence that a basic physical mechanism of flare initiation has been *phenomenologically* captured reasonably well in the flare simulation reported in Chatterjee et al. [2016].

The other interesting aspect was that the flare precursors are height- and flare strength-dependent. Therefore, we mainly focused on the variation of the moment of start time of the approaching phase, and, the moment of the closest approach and estimated flare onset time as a function of height. This investigation was carried out by searching for specific heights at which the approaching motion of  $D_{pn}$  corresponding to a flare event would start earlier and reach its closest position earlier than at any other level (well, at least photospheric level) in the solar atmosphere, so that we may estimate the flare onset earlier in time.

It was found that for the two B-class flares, the most promising levels for flare finding the precursors of the  $WG_M$  method for an eruption are at about 0.3-0.5 Mm above the photosphere. The optimum height for the first C-class flare is between 2.2-2.7 Mm and for the last C-class flare is above 1.3 Mm. These loci in height, found for being most optimal for predicting flares, agree reasonably well with the heights of the occurrence of flares themselves as identified from the analysis of their thermal and Ohmic heating signatures in the simulation. We also estimated the expected time of the flare onsets from the duration of the converging-receding motion of  $D_{pn}$  before each flare. The estimated onset time and the actual time of occurrence for each flare are in good agreement at the corresponding optimum heights. Therefore, we suggest that our numerical experiment serves as a further mounting evidence towards confirming the underlying assumed principles, which we have put forward for potential flare predicting, based on the  $WG_M$  method.

## Chapter 5

# On the evolution of pre-flare patterns in 3-dimensional solar Active Regions

Here, we present the application of our  $WG_M$  method to the lower solar atmosphere where we focus on the pre-flare evolution deduced from 3D magnetic field skeletons of flaring ARs. The construction of 3D magnetic structures is based on PF and NLFFF extrapolations encompassing a vertical range from the photosphere through the chromosphere and transition region into the low corona. The evolution of (i) the  $WG_M$  proxy, (ii) the distance between the area-weighted barycenters of opposite polarities ( $D_{pn}$ ) and (iii) the unsigned magnetic flux ( $\Phi$ ) were all followed, step-by-step at each 45 km in height, from the photosphere up to a few thousand km in the identified  $\delta$ -spots of 13 ARs. In all the investigated  $\delta$ -spots, we found that the evolution of these three components change as a function of height, just like in the case of the simulated flaring AR presented in Chapter 4. Furthermore, we found that the starting and the finishing time of the converging phase change as a function of height, qualitatively also similarly to the MHD case study discussed in Chapter 4. Therefore, here, by applying the  $WG_M$  method we present a tool and recipe to improve flare prediction. Overall, we may summarise that on at average around 1000-1800 km, there is an optimum height range for flare prognosis in the solar atmosphere enabling us to improve by, on average, 3.2 hrs  $\pm$ 2.5 hours our flare prediction capability and capacity.

## 5.1 Introduction

One of the main questions in the research area of solar eruptions is to understand the process of flare occurrence as the removal of free (i.e. non-potential) energy from the solar atmosphere. The free magnetic energy represents the maximum energy that can be dissipated during magnetic reconnection that is driving the intense solar flare occurrences (see Section 1.8). The detailed measurements and modelling of the 3D magnetic field structure of an AR would be important to obtain more accurate information about the pre-flare evolution of a flaring in the solar atmosphere. However, the direct observation of the 3D coronal magnetic field is still elusive. Therefore, today, we still use approximate tools for modelling the solar magnetic field structure in the solar atmosphere. The construction of magnetic field has evolved from routine potential field (PF) to complex and elaborated nonlinear force free field (NLFFF) extrapolations. In practice, to construct the accurate 3D magnetic skeleton of an AR from photospheric measurements is still a challenging task, see e.g. Wiegelmann and Sakurai [2012].

In this Chapter, we focus on the 3D evolution of ARs before intense flare occurrences where the 3D information is obtained by the PF and NLFFF extrapolation techniques. In Figs. 5.1-5.3, we show 3D views of three flaring ARs (AR 11158, 11166 and 11283), as examples, to give an impression about the topic of this chapter. These three figures are snapshots from NLFFF extrapolations. The field lines are coloured according to the blue-red scale of vertical magnetic field ( $B_z$ ), respectively. The  $B_z$  components of the measured photospheric magnetograms are displayed via grey scale images in full resampling resolution, where white represents positive polarity, black represents negative polarity. We also illustrate the identified “sunspots” of the ARs at two different layers further up in the lower solar atmosphere. The identified sunspots are also coloured by blue-red colour scale of  $B_z$ , respectively. Here, we emphasise that these are the sunspots what we adopt for the  $WG_M$  method across the lower solar atmosphere. Furthermore, based on Chapters 3 and 4, our motivation is to identify an optimum height with the  $WG_M$  method, in the lower solar atmosphere, where we could estimate the onset time of an intense flare earlier than only using data available from observing the photosphere.

In this Chapter, we introduce and analyse 13 intense flaring ARs which satisfy the selection criteria given in Sec. 2.2.4. Based on Section 2.2.4, first, we construct the hourly low corona magnetic field structure of the selected ARs in

3D, in the given time period as in Table A.16. Secondly, we perform a detailed comparison analysis between PF [Gary, 1989] and NLFFF [Yan and Sakurai, 2000] extrapolations in the identified  $\delta$ -sunspot(s) of three flaring AR cases in Section 5.2. In the next step, we only apply the PF extrapolation to further 10 flaring AR cases and analyse our findings in Sec. 5.3. At the end of this Chapter, we discuss our results and draw our conclusions in Section 5.4.

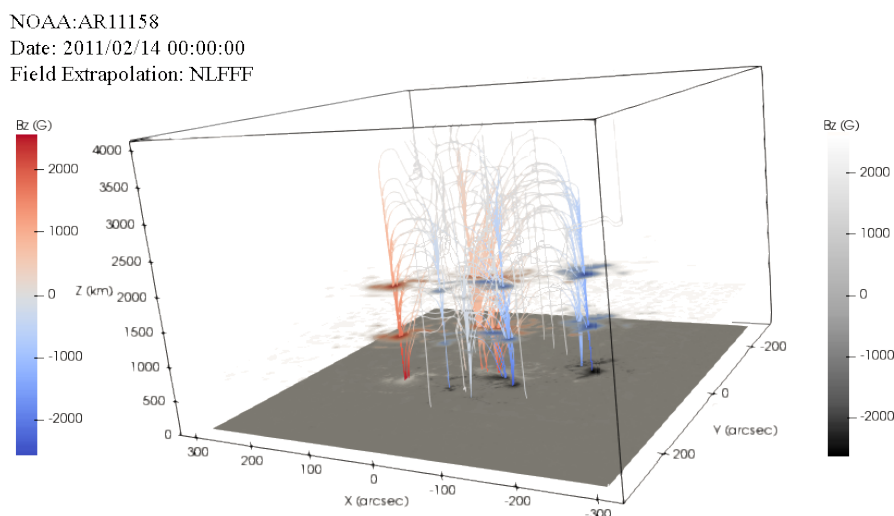


Figure 5.1: The figure illustrates the three-dimensional NLFFF extrapolation of AR 11158. The red-blue colour bar refer to the positive and negative polarity magnetic field values at different heights in the solar atmosphere. The grey colour bar represents the photospheric  $B_z$  magnetic field values. The two horizontal slices, at the 720 and 1485 km levels from the photosphere, represent the identified “sunspots” in the lower solar atmosphere.

## 5.2 Comparison analyses of pre-flare behaviour based on PF and NLFFF extrapolations

In this section, we apply the PF and NLFFF extrapolations in the case of three flaring ARs in order to determine the possible optimum heights for applying

NOAA:AR11166  
 Date: 2011/03/09 00:00:00  
 Field Extrapolation: NLFFF

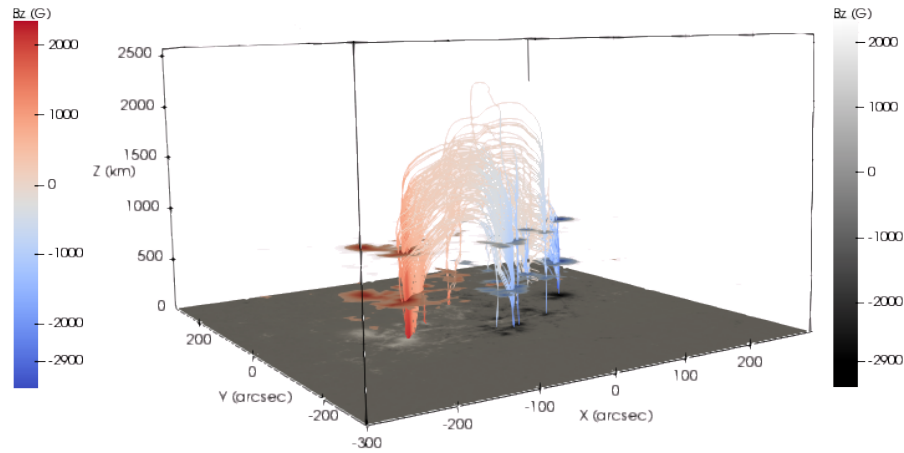


Figure 5.2: Same as Fig. 5.1 but for AR 11166. The identified sunspots are at the 315 and 810 km levels measured from the photosphere.

NOAA:AR11283  
 Date: 2011/09/06 12:00:00  
 Field Extrapolation: NLFFF

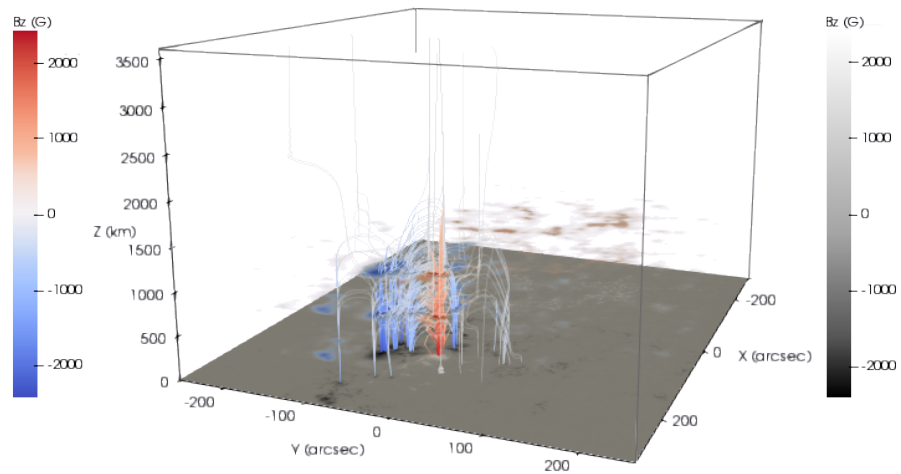


Figure 5.3: Same as Fig. 5.1 but for AR 11283. The two slices with the identified sunspots are the 495 and 990 km levels.

the  $WG_M$  prediction method. We consider a height optimum, as in Chapter 4, where the  $D_{pn}$  parameter would yield the earliest sign of converging phase behavior in time.

In Chapter 4, we found that the optimum heights for best prediction agreed reasonably well with the heights of the occurrence of flares identified from the analysis of their thermal and Ohmic heating signatures in the associated MHD simulation of flare evolution. We were able to successfully determine the two flare precursors of the  $WG_M$  method prior to each flare at the corresponding optimum heights. We also estimated the expected flare onset time from the duration of the converging motion of the  $D_{pn}$  before every single flare. The estimated onset time and the actual occurrence time of each flare were in good agreement at the corresponding optimum heights, which inspires us now to mainly investigate the changes of  $D_{pn}$  leaping upwards from the photosphere to lower corona at each 45 km in height. If we could identify optimum height(s) from an observational point of view then this would bear key importance for an earliest estimation flare of the onset time.

In this study, the PF and NLFFF extrapolation methods play an equally important role, because the free energy of a flaring AR itself does not take any part in applying our  $WG_M$  method. Here, we will compare the results of the  $WG_M$  method in the case of PF and NLFFF extrapolations as a function of height and draw the conclusion of which extrapolation could be more beneficial for flare prediction.

The first region of interest for the comparative analysis of employing the PF and NLFFF is AR 11158, the second one is AR 11166 and the last one is AR 11283. In particular, the regions of interest are the  $\delta$ -spots of the three ARs. Two  $\delta$ -spots were identified in AR 11158, and one-one each for AR 11166 and AR 11283 by Cui et al. [2006], as we can also see here, in Figs. 5.7a-c. Once the  $\delta$ -spots are identified, the evolution of the  $WG_M$  proxy,  $D_{pn}$  and  $\Phi$  are all tracked for each of the entire  $\delta$ -spots at consecutive 45 km steps in height for both of the PF and NLFFF extrapolation cases.

While performing the  $WG_M$  analyses, we noticed that the evolution of the three characteristic pre-flare components change as a function of height, just like in the case of the simulated flaring AR in Chapter 4. Next, before we begin the analyses with the  $WG_M$  method, we need to determine the two relevant characteristic pre-flare features at each 45 km step in height. We can only apply the pre-flare analyses at the height(s) where the pre-cursor behaviours of

the  $WG_M$  and  $D_{pn}$  parameters are identifiable concurrently prior to flare.

Here, throughout in this chapter, we identified the two characteristic pre-flare features somewhat differently when compared to Chapters 3–4 in order to avoid to be biased as much as possible. Namely, here, we apply the best  $n$ th degree polynomial fit to the  $WG_M$  data ( $f(WG_M)$ ) and to the distance data ( $f(D)$ ) at each 45 km in height. We use a Python script, with the NumPy library, which determines the maximum (orange dots in Figures 5.8– 5.16) and minimum values (blue dots in Fig. 5.8– 5.16) of  $f(WG_M)$  and  $f(D)$ . Next, from these calculated values, we establish the two pre-flare behaviours, which are assumed to be related to the upcoming flare rather than merely an insignificant fluctuation. So, the script evaluates (i) the relative gradient of the rising phase of  $WG_M$  and (ii) the relative gradient of the converging motion from the corresponding maximum and minimum values. The relative gradient of the rising phase of  $WG_M$  is calculated from the difference between the previous minimum and maximum values prior to flare. The relative gradient of the converging motion is determined from the maximum and the minimum values of the converging phase. Furthermore, a maximum of 10% deviation allowance of the diverging phase is also cross-checked at each applicable height. Actually, the 10% deviation allowance is obtained from the difference of the maximum value of the converging phase and the maximum value of the diverging phase.

Once we successfully identified the relevant pre-flare patterns of the  $WG_M$  and  $D_{pn}$  at a certain height, then we just focus on the evolution of the pre-flare behavior of the  $D_{pn}$  parameter as a function of height. Especially, based on Chapter 4, we concentrate on the beginning and finishing moments of the converging phase determined at each 45 km. Let us now plot the starting time ( $f(D)_{Max}$ , green lines) and finishing time ( $f(D)_{Min}$ , blue lines) of the converging phase at each 45 km in the three different AR cases.

In Figures 5.4– 5.6, the fat lines represent the data using PF extrapolation and the dashed lines indicate the results of the NLFFF case for the constructed 3D magnetic skeletons of an AR. Also, the red lines denote when the investigated flare occurred. In Figures 5.4– 5.6, we can observe how the converging phase begins earlier and reaches the closest location also earlier at a certain height (referred to as the *optimum height*) than it does at the photosphere or at other heights, similarly as found in Chapter 4. We also summarise the actual findings in Table 5.1 for establishing evidence for the two relevant pre-flare behaviours in the photosphere and at the defined optimum height in the cases of both the

PF and NLFFF extrapolations.

Once we identified the corresponding optimum height for each flare then we carried out further aspects of the  $WG_M$  analyses in the photosphere and at these optimum heights. We estimated the percentage difference ( $WG_M^{\%}$ ), the expected largest flare intensity class ( $S_{flare}$ ) and the flare onset time ( $T_{est}$ ) by Eqs. (3.1)–(3.2) to test the applicability of the  $WG_M$  method. We summarise the obtained three estimated values in Table 5.2. Furthermore, Table 5.2 also includes how many hours earlier the converging phase ( $T_{Imp}^C$ ) started, and, also finished earlier ( $T_{Imp}^M$ ) at the optimum height when compared to its analogue determined from data in the photosphere in both of the extrapolation cases. The  $T_{Imp}^M$  is a so-called the *lead-time* at the corresponding optimum height because we calculate the flare onset time from  $f(D)_{Min}$ – $f(D)_{Max}$ . Actually, the values of the  $T_{Imp}^M$  could give the desired estimate about how many hours one could win for the flare onset time estimation if one applies the  $WG_M$  method at an identified optimum height.

In the next three subsections, let us now see how to determine the lead-times and the optimum heights in both of the PF and NLFFF extrapolations for four X-class flare of 3 AR cases. We also briefly summarise how the  $WG_M$ ,  $D_{pn}$  and  $\Phi$  evolve in the photosphere and at the defined optimum heights.

### 5.2.1 AR 11158

Let us see first the case of *AR 11158* when the 3D magnetic skeleton is constructed using both the PF and NLFFF magnetic field extrapolation methods. We now analyse the pre-flare dynamics of the two identified  $\delta$ -spots, i.e. the 1st and 2nd  $\delta$ -spots, respectively, before the X2.2 flare. The two  $\delta$ -spots are visualised in Fig. 5.7a. The flare actually occurred at 01:56 on 15/02/2011 from the 2nd  $\delta$ -spot of AR 11158 according to Wang et al. [2012].

- The 1st  $\delta$ -spot: In the photosphere, the pre-flare behavior of the  $WG_M$  is discernible in both of the two extrapolation cases. Nevertheless, the first striking difference, from the analysis of the two characterising pre-flare features of using PF and NLFFF data is in the behavior of the  $D_{pn}$  parameter. In the PF case, the  $D_{pn}$  only increases and seems to be less useful, but, we can see the pre-flare behavior of the  $D_{pn}$  in the NLFFF case (see Fig. 5.8a-b). We also noticed that the deviation of  $D_{pn}$  is not in the

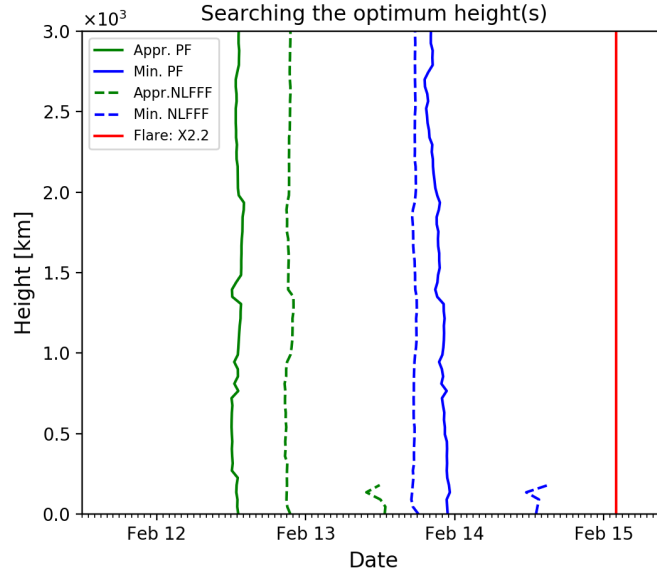


Figure 5.4: *AR 11158*: The fat/dashed lines are associated with the analyses of extrapolation of the observed photospheric input data using the PF/NLFFF technique, respectively. The actual moments of starting time of converging (green lines) and moments of the closest location between two barycenters (blue lines) are plotted as a function of height. The red vertical line indicates the flare occurrence time.

$\pm 10\%$  allowance interval. For satisfaction of our curiosity, we considerate it as a precursor then we could observe the pre-flare behavior of the  $D_{pn}$  from the photosphere up to 180 km in the solar atmosphere, using the NLFFF magnetic data. We also found that the height of 135 km became the optimum height here. At that height, the converging phase began 3 hours beforehand and finished 1.5 hrs earlier than in the photosphere. Here, the  $S_{flare}$  is underestimated, but the values determined for  $WG_M^{\%}$  and  $T_{est}$  are not that bad at all. The  $WG_M^{\%}$  is 38% which is close to the 42% photospheric value whereupon we do not expect X-class energetic flare. The difference between  $T_{est}$  and  $T_{D+F}$  is lower than the uncertainty of the  $T_{est}$  ( $\pm 7.2$  hrs).

- The 2nd  $\delta$ -spot: The two required typical pre-flare behaviors of the  $WG_M$  and the  $D_{pn}$  parameters are both observable prior to X2.2 flare in both of

the extrapolation cases, down from the photosphere up to 3000 km in the low corona. In the PF case, the optimum height is 1395 km because the converging phase started with a maximum of 1.2 hours beforehand and finished 2 hrs earlier than in the photosphere. In the NLFFF case, the  $T_{Imp}^C$  is 0.92 hrs and  $T_{Imp}^M$  is 0.73 hrs at best of 810 km. Here, we could estimate the flare onset time 1.27 hr earlier with the PF data than with the magnetic data of the NLFFF extrapolation. Both of our analyses here, and many observations elsewhere, proof that the 2nd  $\delta$ -spot is the source of the X2.2 flare. The  $S_{flare}$  and  $T_{est}$  are fairly well estimated in the two extrapolation cases (see Table 5.2). The estimated flare onset times are also very close to the actual values of  $T_{D+F}$ . We cannot tell this, however, about the  $WG_M^{\%}$ .

### 5.2.2 AR 11166

The second example is *AR 11166*. Here, we investigate the pre-flare states before the X1.5 flare. This flare occurred in the single  $\delta$ -spot of the AR [Vemareddy and Wiegmann, 2014] at 23:23 on 09/03/2011. We recognise the prominent and typical pre-flare behavior of the  $WG_M$  and the  $D_{pn}$  prior to X1.5 in the vertical region from the photosphere up to 2000 km at each 45 km step. In the PF extrapolation case, we can identify one increasing, one maximum followed by a decreasing phase of the  $WG_M$ , and, also one full converging-diverging motion of the area-weighted barycenters prior to flare. However, in the case of the NLFFF extrapolation, we further notice that two consecutive precursors of the  $WG_M$  and the  $D_{pn}$  appear instead of one above 500 km (see Figs. 5.12- 5.13). It is worth to mention that we applied two best fitting polynomials which handle separately the two consecutive precursors of the  $WG_M/D_{pn}$ . Furthermore, the first diverging phase cannot reach the 10% deviation allowance in the photosphere (see Table 5.1), but for the sake of optimum height identification we considerate the first pre-flare behaviour of the  $D_{pn}$  as a precursor.

In the PF case,  $T_{Imp}^C$  is 0.9 hrs and  $T_{Imp}^M$  is 3.58 hrs at 1080 km. We found two pre-flare behaviors of the  $D_{pn}$  in the NLFFF case, but to identify the optimum height, we use only the first one. At the 315 km, the  $T_{Imp}^C$  is 1.2 hrs and  $T_{Imp}^M$  is 2.93 hrs. Here, we could estimate the flare onset time about 3 hrs earlier in the case of both extrapolations. Unfortunately,  $T_{est}$  seems to be rather overestimated with 10 hrs in the PF extrapolation case. However, the  $T_{est}$  value is well agreement with the  $T_{D+F}$  value in NLFFF extrapolation case. In the PF

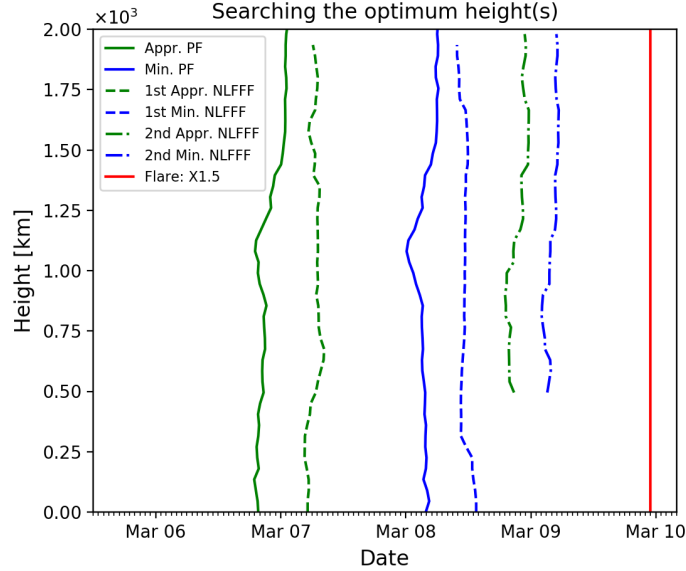


Figure 5.5: Same as Fig. 5.4 but for *AR 11166*.

case, using Eq. (3.1), we underestimate the expected flare intensity class. In the NLFFF case, the  $S_{flare}$  is found to be correct. The  $WG_M^{\%}$  values are not so prominent either in the case of PF or in the case of the NLFFF extrapolation.

### 5.2.3 AR 11283

The last example is *AR 11283* with a flare of X1.8 at 22:20 on 06/09/2011 and with another of X2.1 at 22:38 on 07/09/2011. These two flares occurred in the same  $\delta$ -spot of the AR [Liu et al., 2014]. Here, the characteristic pre-flare behavior of the  $WG_M$  and the  $D_{pn}$  are evaluated using the appropriate 3D magnetic skeletons were both patterns are recognisable prior to each of the two flares. We found that the two pre-flare behaviours of the X1.8 flare disappear from 1000 km upward both of the PF and NLFFF extrapolation cases. In the X1.8 flare case, the optimum height of the PF is 90 km and for the NLFFF it is also 90 km.  $T_{Imp}^C$  is 1.6/1.15 hrs and  $T_{Imp}^M$  is 2.11/1.51 hrs in the PF/NLFFF case, respectively.

In the X2.1 flare case, the optimum height is found to be 1035 km for PF

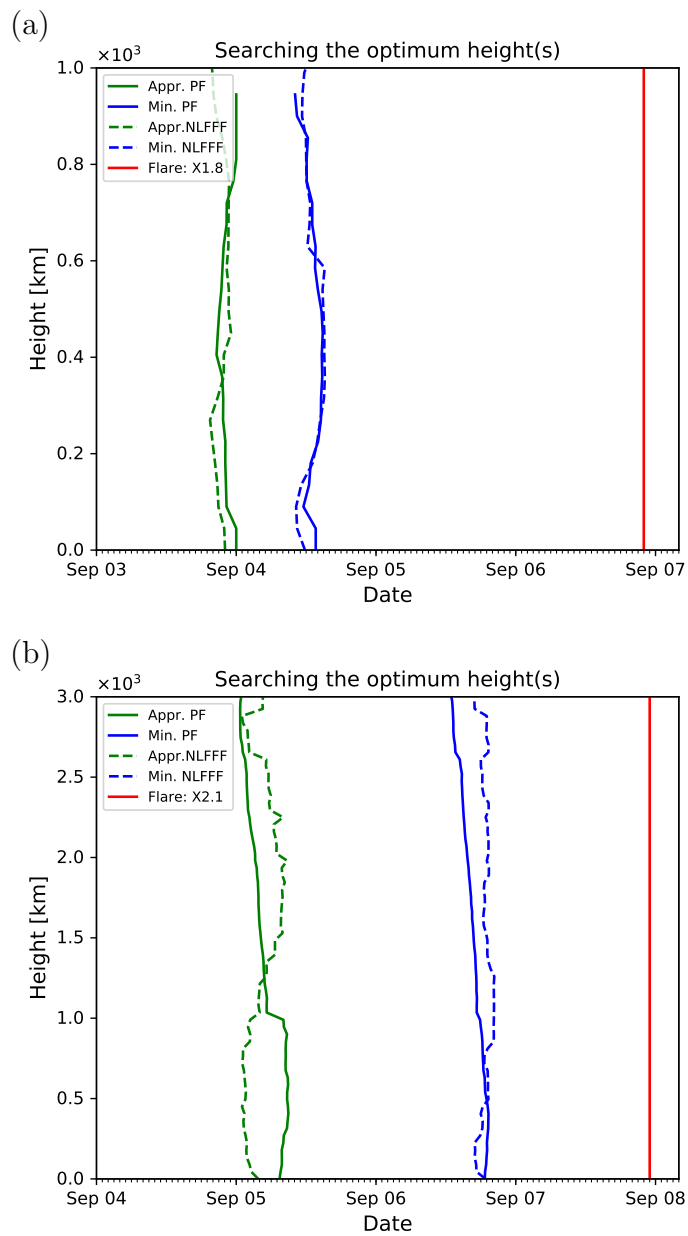


Figure 5.6: The plots (a) and (b) correspond two X-class flares (X1.8 and X2.1 flares) of *AR 11283*.

and 225 km for the NLFFF magnetic skeletons. The converging phase started 2.2 hours beforehand and finished 1.9 hrs earlier at 1035 km compared to the result of analysis applied data to in the photosphere. The  $T_{Imp}^C$  is 1.95 hrs and  $T_{Imp}^M$  is 1.86 hrs at 225 km. Here, we could estimate the onset time of the X1.8 flare 0.60 hrs earlier with the PF data when compared to its counterpart obtained with the NLFFF extrapolation. For the X2.1 flare, the PF and NLFFF are similarly beneficial.

In summary, the overall situation with the estimates is similar to that for *AR 11166* in the PF case. Here, in the two extrapolation cases, the  $T_{est}$  values are underestimated for the X1.8 flare when, while, the  $T_{est}$  values are overestimated for the X2.1 case like in the PF case of *AR 11166*. The  $S_{flare}$  values are fairly well estimated. The  $WG_M^{\%}$  values are also not so prominent, except for the X2.1 flare evaluated from the NLFFF data.

Based on the above Subsections 5.2.1–5.2.3, we summarise the results of the analysis of the NLFFF and PF extrapolations in Fig. 5.17 and Table 5.2. In Fig. 5.17a, the green columns demonstrate the improvement of determining the starting time of the converging phase at the optimum height. The blue columns show the gained time of the finishing of the converging phase at the optimum height. In Fig. 5.17b, the red columns represent the optimum height of the particular flare event. In Figure 5.17, the columns with no cross lines indicate the optimum heights of data analysis carried out using PF and the columns with black cross lines stand for the results obtained with NLFFF extrapolation. The plotted values expressed in numbers are given in Table 5.2.

From Fig. 5.17 and Table 5.2, we conclude that the optimum heights and the lead prediction time improvements are different in the three AR cases. We investigated only three ARs, because the running time of the NLFFF extrapolation code takes about 3-4 months for one AR case, while it is 2-3 hours or could even just be minutes on a powerful computer in the case of PF extrapolation.

Furthermore, we also noticed that, indeed, sometimes the lead-time is better in the NLFFF extrapolation case and at another time it is better in the case of using PF data. But, the differences of the corresponding two lead-times are not so significant. Based on this finding and the needed very long CPU running time for the NLFFF extrapolation, we now propose to use only the PF extrapolation in the further studies.

NOAA AR	PF			NLFFF		
	$WG_M^{Inc}$ -T %- hrs	$D^{Dec}$ -T %- hrs	$D^{Inc}$ %	$WG_M^{Inc}$ -T %- hrs	$D^{Dec}$ -T %- hrs	$D^{Inc}$ %
Photosphere						
11158	28-23	-	-	136 - 17	32 - 24	↓17
	720 - 40	35 - 33	↓2	386 - 36	40 - 20	↑16
11166	363 - 38	42 - 33	↓2	324- 35	58 - 44	↓30
11283	41 - 5	13 - 9	↓9	247 - 15	16 - 20	↓9
	30 - 25	22 - 42	↓9	93 - 38	33 - 41	↓10
Optimum height						
11158	-	-	-	886 - 17	24 - 39	↓12
	413 - 32	30 - 33	↓2	325 - 37	36 - 21	↑14
11166	181 - 47	44 - 30	↑24	265/205 - 30/10	57/51 - 29/12	↑3 / ↓10
11283	61 - 13	14 - 11.5	↓6	20- 18	14- 18	↓6
	39 -38	23- 36	↓10	100- 69	31 - 26	↓7

Table 5.1: Ascertainment of the two flare precursors ( $WG_M$  and  $D_{pn}$ ) (see Chapter 3) with the fitted  $n$ th degree polynomial at the photosphere and at the optimum height for analyses using the PF and NLFFF extrapolations data. The second column shows the relative gradient of the rising phase of  $WG_M$  ( $WG_M^{Inc}$ ). The third column is the relative gradient of the distance parameter of the converging motion ( $D^{Dec}$ ). The fourth column lists the deviation of the distance as it increases back to its original value it had at the moment when the converging phase started ( $D^{Inc}$ ). The ↓/↑ indicate the passed/missed with  $x\%$  compare to the beginning value of the  $D^{Dec}$ . The  $T$  values indicate the elapsed time for the considered  $WG_M^{Inc}$  and  $D^{Dec}$ .

NOAA AR	Flare Intensity	PF						NLFFF							
		$T_{Imp}^C$ [h]	$T_{Imp}^M$ [h]	Opt. Height [km]	$S_{flare}$	$WG_M^{\%}$ [%]	$T_{est}$ [h]	$T_{D+F}$ [h]	$T_{Imp}^C$ [h]	$T_{Imp}^M$ [h]	Opt. Height [km]	$S_{flare}$	$WG_M^{\%}$ [%]	$T_{est}$ [h]	$T_{D+F}$ [h]
11158	X2.2	-	-	-	-	-	-	-	3	1.5	135	<M5	38	34.9	41.7
		1.2	2.00	1395	X	15	29.5	32.7	0.92	0.73	810	X	14	30	32
11166	X1.5	0.9	3.58	1080	>M5	13	40.1	31.6	1.20	2.93	315	X	-	39.5	36.2
		1.6	2.11	90	X	-	22.2	53.6	1.15	1.51	90	X	-	25.5	58.9
11283	X2.1	2.2	1.9	1035	X	14	39.2	29.3	1.95	1.86	225	X	81	51.47	30.1

Table 5.2: Comparison table of the results obtained by means of PF and NLFFF extrapolations in the three investigated AR cases. The table includes how many hours earlier the converging phase ( $T_{Imp}^C$ ) began, and reached the minimum value ( $T_{Imp}^M$ ) at the optimum height when compared to the photosphere.  $S_{flare}$  is the estimated flare class,  $WG_M^{\%}$  is the percentage difference at the corresponding optimum height.  $T_{est}$  is the estimated flare onset time.  $T_{D+F}$  is the elapsed time from the moment of the closest location of the two opposite polarity barycenters to the flare onset.

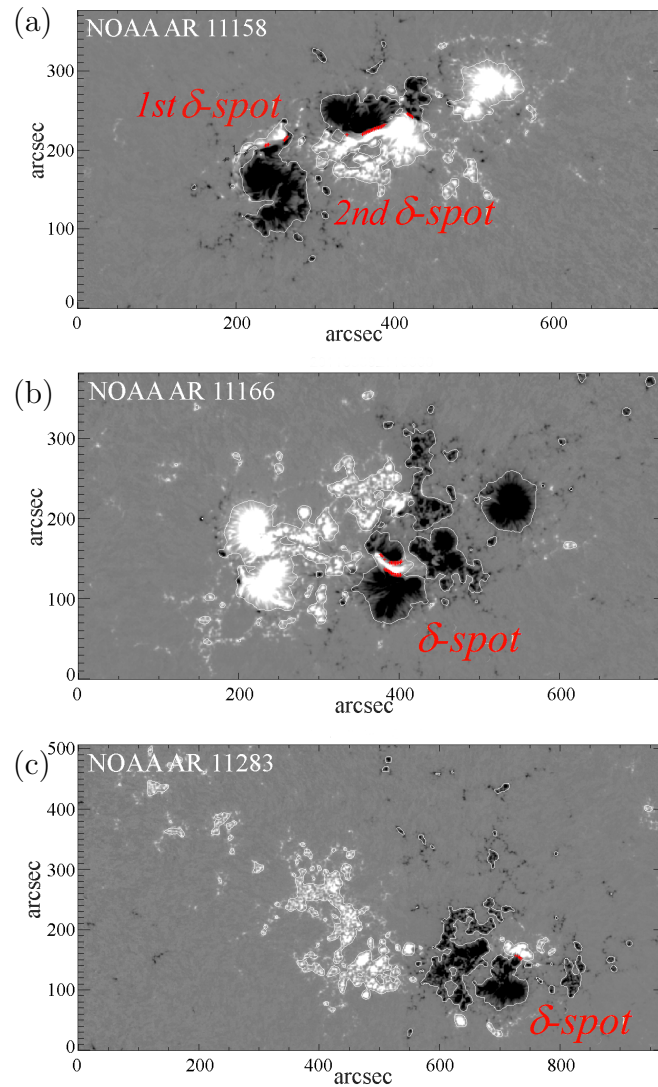


Figure 5.7: LOS magnetogram snapshots showing the analysed  $\delta$ -spots of three example ARs: (a) the two  $\delta$ -spots of AR11158 on 14/02/2012 at 17:00:00; one - one  $\delta$ -spot of (b) AR 11166 on 09/03/2011 at 11:00:00 and (c) AR 11283 on 04/09/2011 at 18:00:00. The red dotted lines are the automatically identified PILs of the ARs. The white countered areas show where the magnetic field is larger than  $|150|$  G.

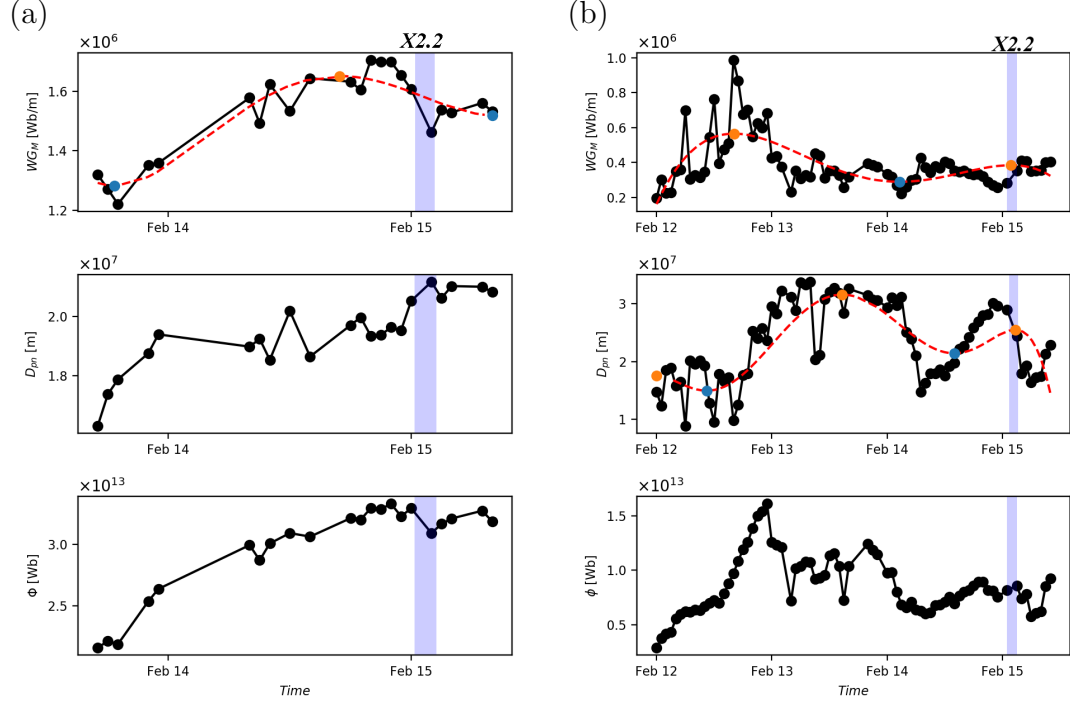


Figure 5.8: Panels (a) and (b) show the result of the  $WG_M$  analysis for the 1st  $\delta$ -spot case of AR 11158 (see Fig. 5.7a at the photosphere). Panels (a) and (b) reveal the evolution of the various pre-flare indicators, applied to the PF and NLFFF magnetic extrapolation data. The  $x$ -axis is time, measured in date. The upper panel is the temporal variation of  $WG_M$ . The pre-flare behavior of  $WG_M$  is fitted by an  $n$ th-order polynomial (red line), where the orange dot corresponds to the maximum of  $WG_M$ . The middle panel demonstrates the evolution of  $D_{pn}$ . The consecutive maximum-minimum-maximum (orange-blue-orange dots) locations of the fitted  $n$ th-degree polynomial highlight the full converging-diverging motion uncovered by  $D_{pn}$ . The vertical blue lines indicate the moment when the flare occurred. The bottom panel shows the evolution of the unsigned magnetic flux ( $\Phi$ ).

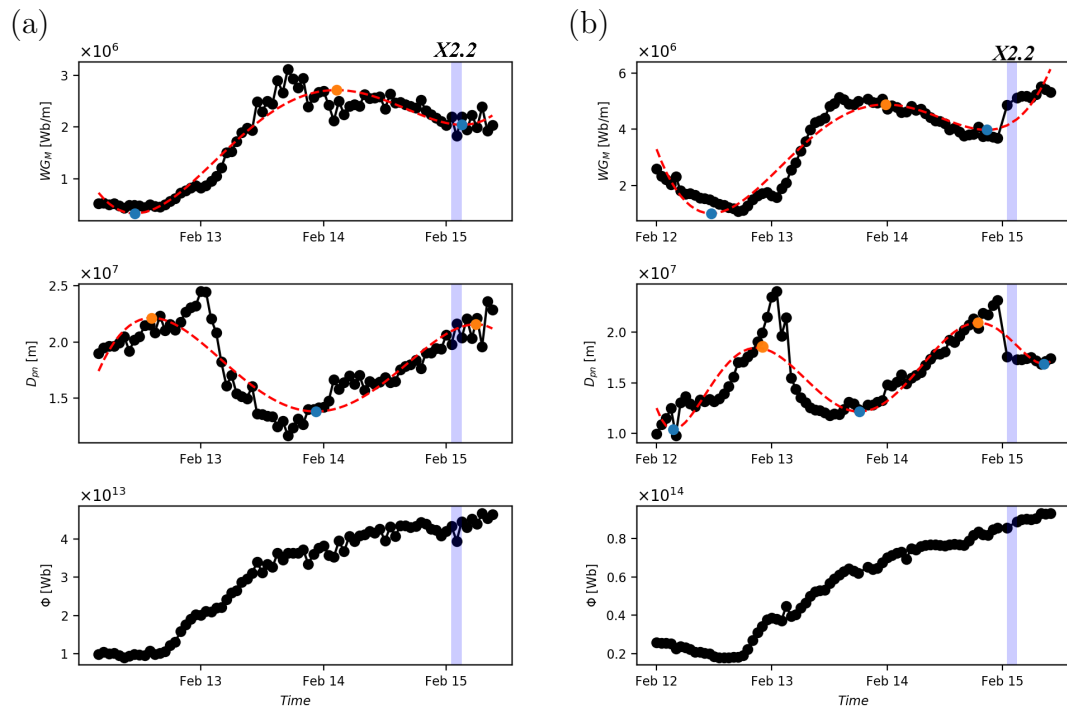


Figure 5.9: Same as Fig. 5.8 but for the 2nd  $\delta$ -spot of 11158 AR at the photosphere (see Fig.5.7a). The panel (a) is the PF and panel (b) the NLFFF extrapolation case, respectively.

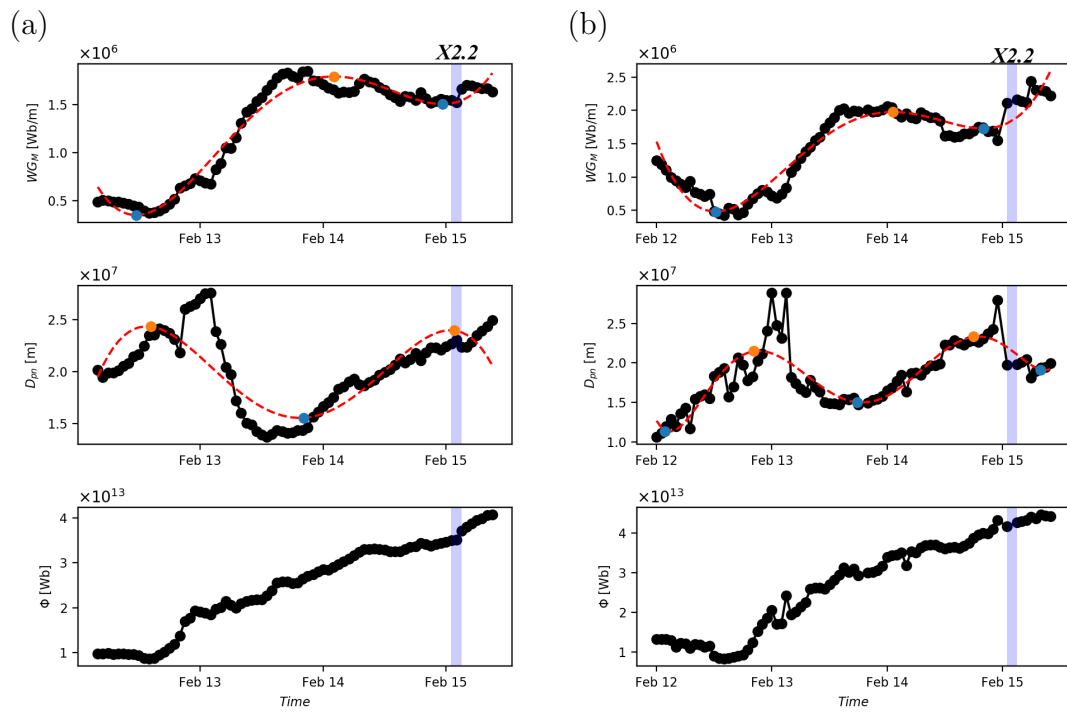


Figure 5.10: Same as Fig. 5.9 for *AR 11158* but panels (a) and (b) illustrate the evolution of the three parameters at the optimum height. (a): The optimum height is 1395 km above the photosphere in the PF case. (b): The optimum height is 810 km from the photosphere in the NLFFF case.

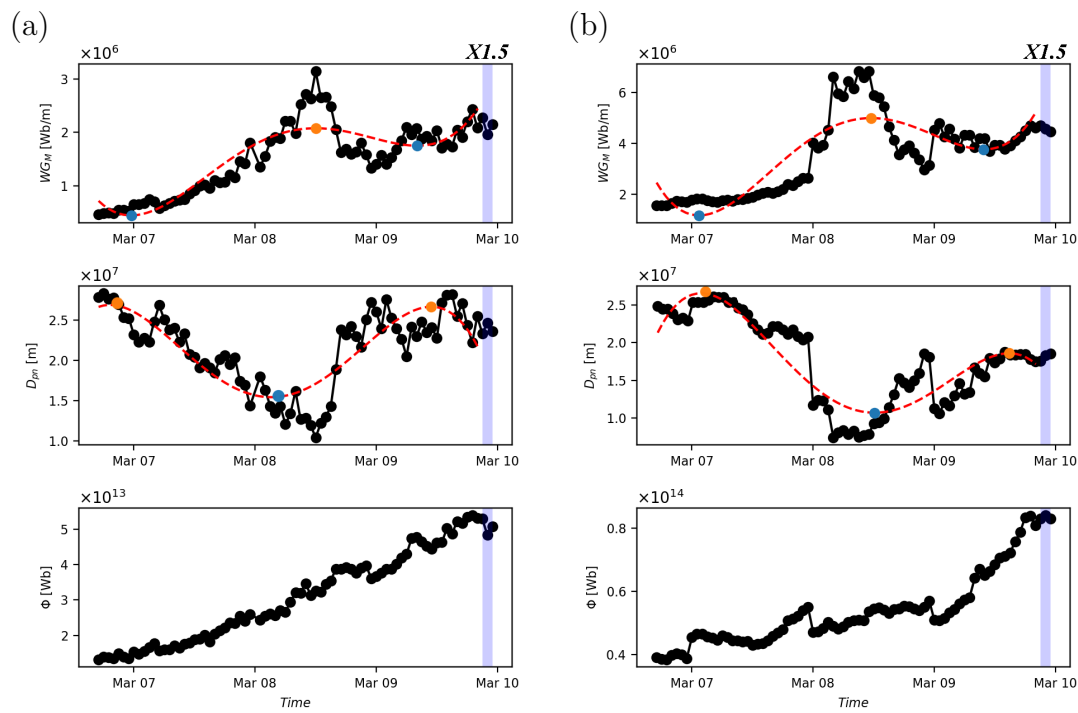


Figure 5.11: Same as Fig. 5.8 but for the  $\delta$ -spot of *AR 11166* (see Fig. 5.7b) at the photosphere.

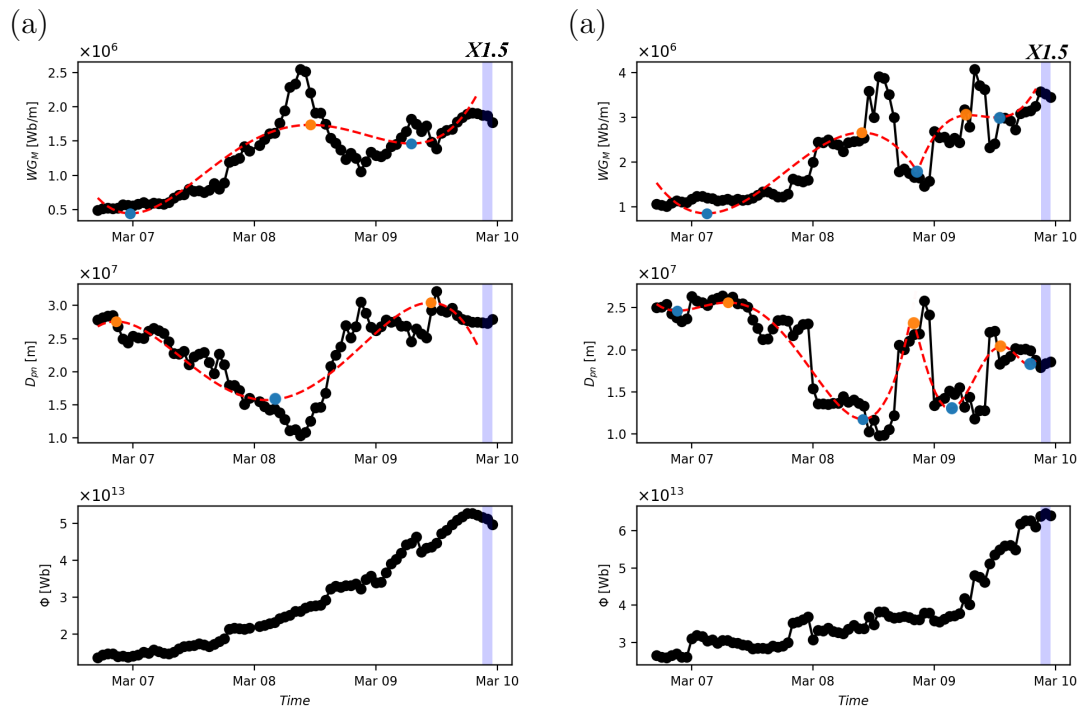


Figure 5.12: Same as Fig. 5.11 for AR 11166 but at 495 km above the photosphere.

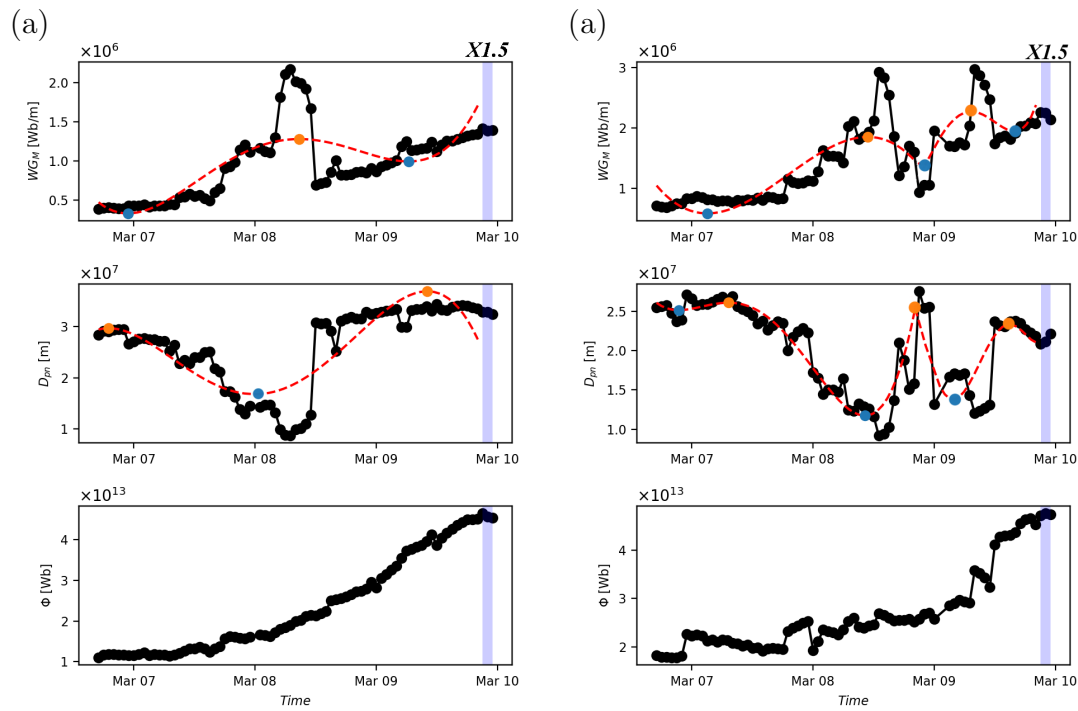


Figure 5.13: Same as Fig. 5.11 for *AR 11166* but at 1080 km above the photosphere, in the lower solar atmosphere.

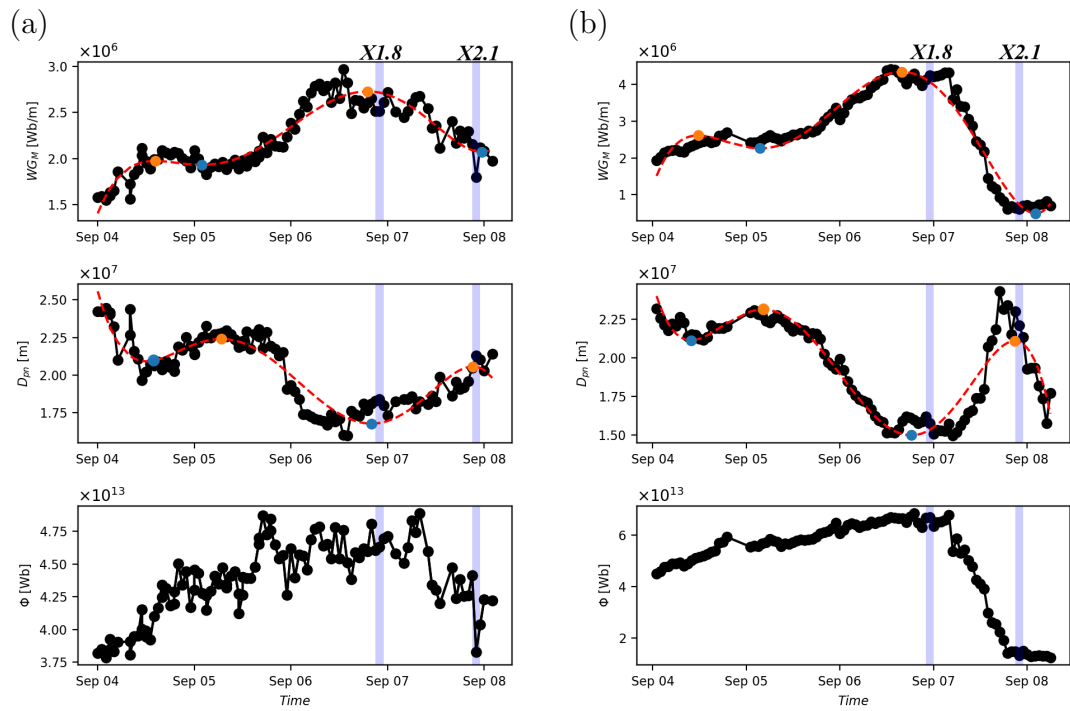


Figure 5.14: Same as Fig. 5.8 but in the  $\delta$ -spot of *AR 11283* (see Fig.5.7c) at the photosphere.

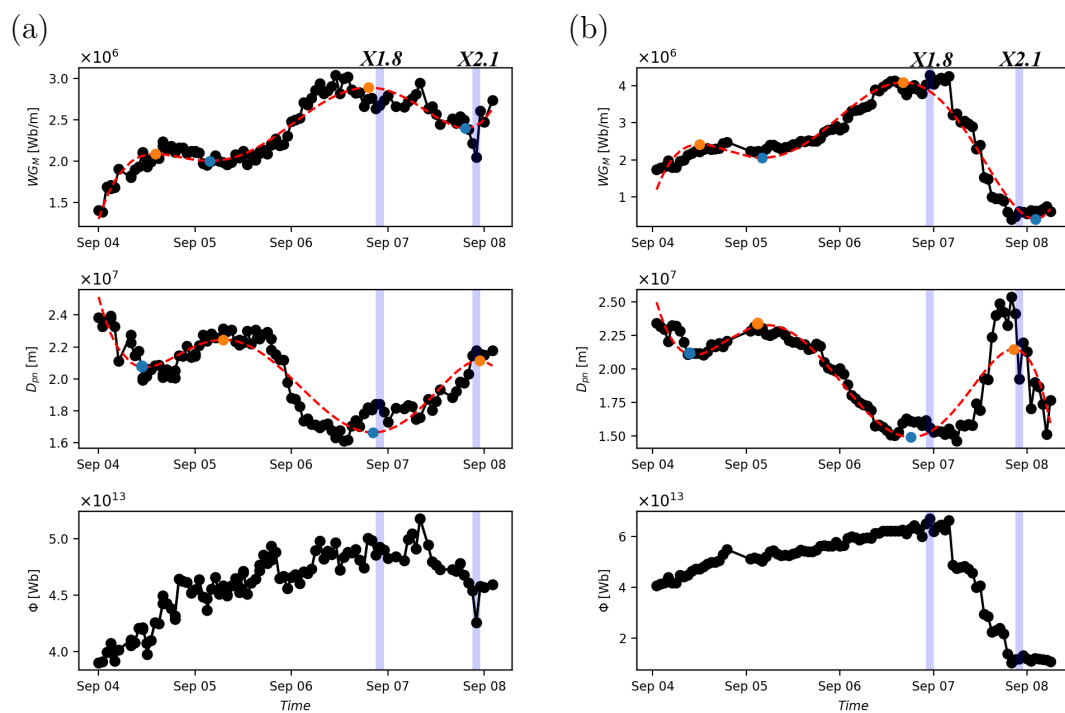


Figure 5.15: Same as Fig. 5.8 but for *AR 11283*. Panels (a) and (b) show the results found after applying the  $WG_M$  method to both the PF and NLFFF extrapolations at the corresponding optimum heights for the first X1.8 flare in the two extrapolation cases. The optimum height of the PF case is 90 km and for the NLFFF it is 90 km from the photosphere.

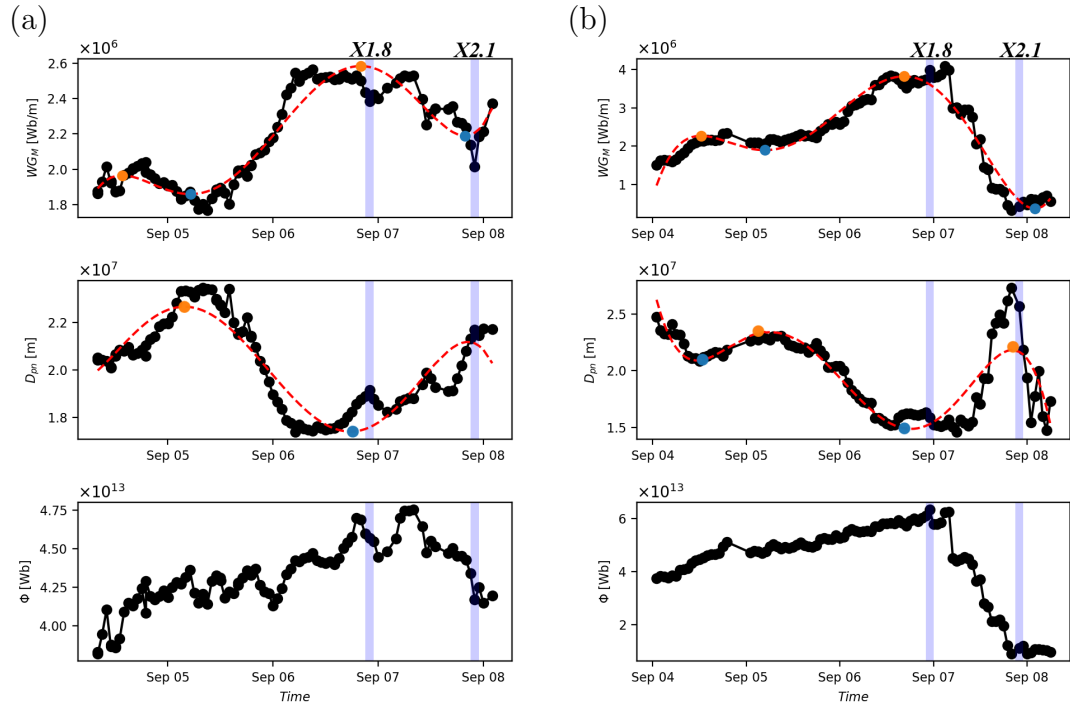


Figure 5.16: Same as Fig. 5.8 but for *AR 11283*. Panels (a) and (b) show the pre-flare evolution of the three parameters for the PF and NLFFF extrapolations at the corresponding optimum height for the second X2.1 flare. Here, the optimum height of the PF case was found to be 1035 km and for the NLFFF case it is 225 km from above the photosphere.

### 5.3 Application of PF to more ARs

In this Section, we analyse further 10 ARs with 16 flare cases (see Table 5.3), which all satisfy the selection criteria given in Sec. 2.2.4. We constructed the 3D magnetic field skeleton of each of them with PF extrapolation and identified the  $\delta$ -spot of each AR. Next, the  $WG_M$  analysis was applied to each  $\delta$ -spot as a function of height with 45 km steps upward in the vertical direction perpendicular to the solar surface. Also, we carried out the necessary analyses accordingly, as given in Section 2.2.4, to identify the relevant pre-flare behaviors of the  $WG_M$  and  $D_{pn}$  parameters at each 45 km level. Similarly to Sec. 5.2, we noticed that the evolution of the three components ( $WG_M$ ,  $D_{pn}$  and  $\Phi$ ) change as a function of height, and also, the converging phase began earlier and reached the closest location also earlier at a certain height in all cases of the investigated 16 flares. We could i) identify the optimum heights, ii) determine where the  $D_{pn}$  parameter yields the earliest sign of converging phase in time, and iii) confirm the PF approximation is applicable for our 3D  $WG_M$  analyses.

Figure 5.18a demonstrates, with the green and blue columns, how many hours earlier the converging phase began ( $T_{Imp}^A$ ) and finished ( $T_{Imp}^M$ ) at the optimum height when compared to their counterparts in the photosphere. Furthermore, the red columns represent the corresponding optimum heights of the particular AR in Figure 5.17b. The  $x$ -axis of Figures 5.17a-b lists the AR that hosted flare in the same order as the ARs are listed in the PF part of Table 5.2 and Table 5.3. Based on Figure 5.18 and Table 5.3, we conclude that we can estimate the expected flare onset time at the associated optimum height earlier.

From the PF part of Table 5.2 and Table 5.3, we can see that the converging phase began between a maximum of 1-16 hrs earlier ( $T_{Imp}^C$ ) and also finished between 1-8 hrs earlier ( $T_{Imp}^M$ ) at the corresponding optimum heights in the most of the cases. We have also noticed that the related optimum heights split into two district intervals, 90-600 km and 1000-1800 km, respectively. Interestingly,  $T_{est}$  is well estimated at the optimum height of 1000-1800 km if we consider the  $\pm 7$  hr uncertainty. This, however, cannot be said for the 90-600 km height range because the differences are large between  $T_{est}$  and  $T_{D+F}$  in most cases. Occasionally, we found that the difference can be even more the 2 days (see e.g. AR 11520, 12158 and etc in Table 5.3). The large overestimation in the range of 90-600 km could come from the potentially poor estimation of the physical conditions of the mid-and-upper chromosphere.

The parameter  $S_{flare}$  is estimated well in about 90% of the 16 flare cases at the corresponding optimum heights.  $S_{flare}$  is highly underestimated only in the cases of AR 11430 and 12158. Unfortunately, similarly to Sec. 5.2, the  $WG_M^{\%}$  values are not so prominent at the corresponding optimum heights.

To realise which optimum height range is more prominent, we subdivided the flare samples accordingly to the two defined intervals, 90-600 km and 1000-1800 km. Furthermore, in order to determine an average lead-time, we use  $T_{Imp}^M$ . The parameter  $T_{Imp}^M$  shows how many hours earlier the converging phase stops at the optimum height when compared to a similar analysis carried out for data in the photosphere. This is a very important information because estimating the flare onset time is based on the linear relationship between the duration of the diverging motion of the opposite polarities until the flare onset and the duration of the converging motion of the opposite polarities. Therefore, when the converging phase is over at some time earlier at some other height in the chromosphere than in the photosphere, then there is an opportunity to estimate the flare onset time earlier.

Finally, we apply descriptive statistics on two set of  $T_{Imp}^M$  values to determine an average lead-time within the given two optimum height intervals. The statistical mean is 2.2 hrs with standard deviation of 1.4 hrs in the 90-600 km interval. Nevertheless, the mean is 3.2 hours and the associated standard deviation is 2.5 hrs between for the data for 1000 km and 1800 km. Based on our findings in the PF extrapolation cases, we conclude that the average lead-time improvement could be  $3.2 \pm 2.5$  hours if we use the  $WG_M^{\%}$  between 1000 and 1800 km in the solar lower atmosphere.

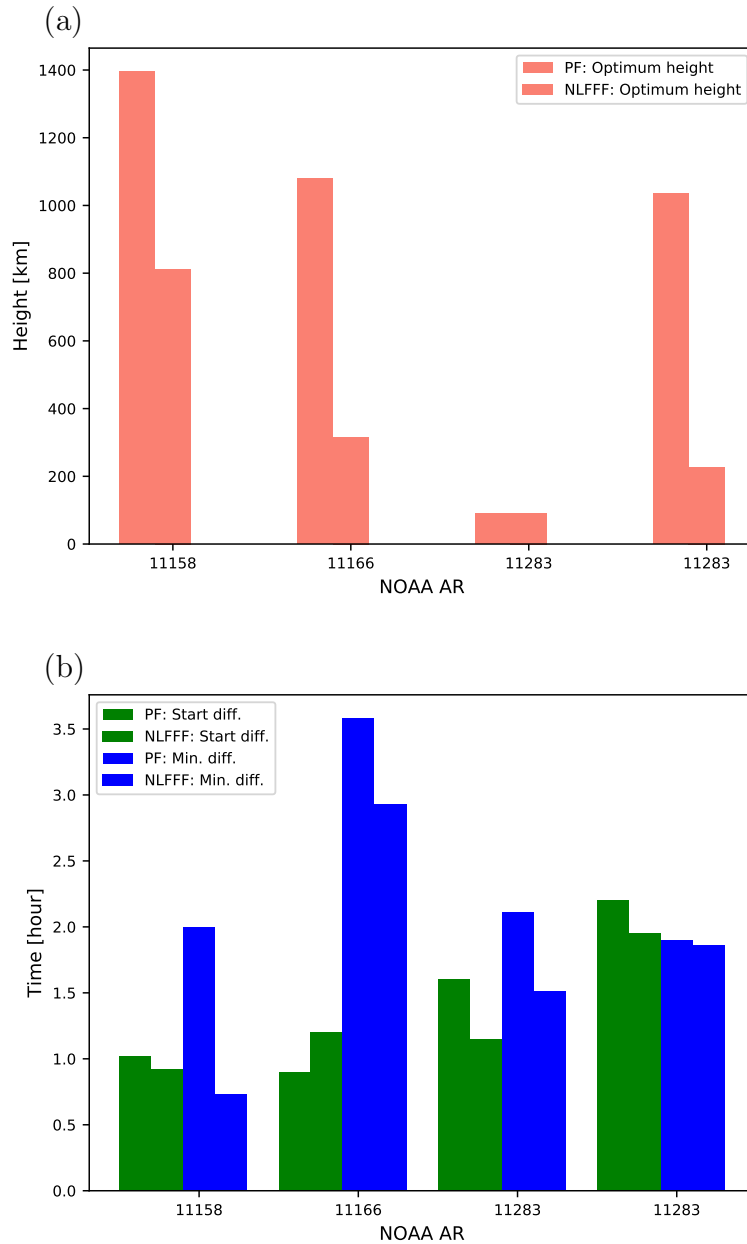


Figure 5.17: Comparison analyses of the optimum heights and lead-times for PF (filled column) and NLFFF (filled column with black crossed lines) extrapolations. Panel (a) shows the identified optimum height of the corresponding flare events in three ARs. Panel (b) gives an insight into the lead-time improvement for each studied flare when the method is applied to data taken at their own optimum height for each AR. The green/blue columns show how much earlier the converging phase started/reached the smallest  $D_{pn}$  value at the optimum height when compared to their corresponding data in the photosphere (see Table 5.2).

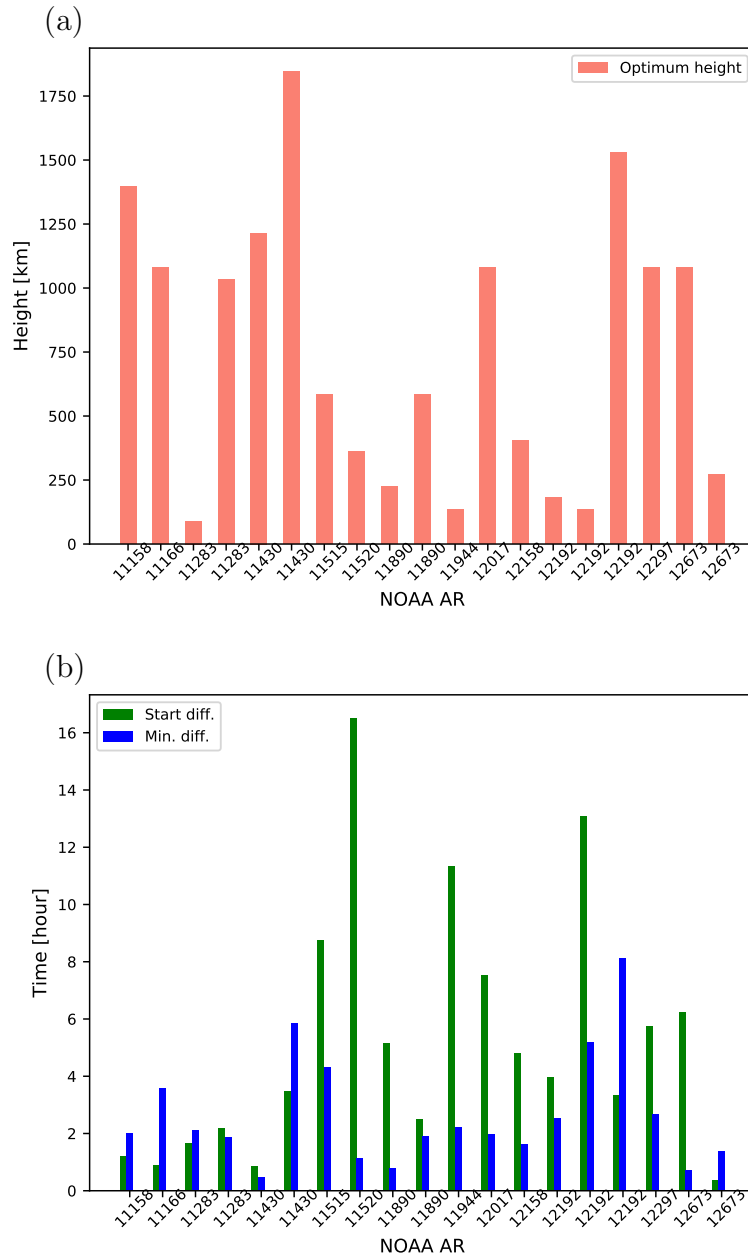


Figure 5.18: Optimum height and lead-time obtained by means of the analyses of the PF extrapolation for constructing the magnetic skeletons of 13 ARs with 20 X-class flare cases (see Table 5.2–5.3). Panels (a) and (b) are in the same spirit as that of in Fig. 5.17.

NOAA AR	Flare Intensity	PF						
		$T_{Imp}^C$ [h]	$T_{Imp}^M$ [h]	Opt. Height [km]	$S_{flare}$	$WG_M^{\%}$ [%]	$T_{est}$ [h]	$T_{D+F}$ [h]
11430	X1.3	0.85/3.48	0.47/5.85	1215	<M5	44	19.8/13.4	26.4/8.6
11515	X1.1	8.75	4.33	585	X	40	89.8	35.3
11520	X1.4	16.5	1.12	360	X	5	65.8	67.7
11890	X1.1	5.15	0.77	225	X	28	62.5	15.5
	X1.1	2.5	1.92	585	>M5	25	27.6	21.4
11944	X1.2	11.35	2.22	135	X	34	45.7	45
12017	X1.0	7.52	1.97	1080	>M5	21	24.9	32.3
12158	X1.6	4.82	1.63	405	<M5	65	49.5	30.5
12192	X1.6	3.98	2.53	180	X	90	34.6	57.6
	X3.1	13.07	5.18	135	X	10	47.6	40.4
	X1.1/X2.0	3.35	8.12	1530	X	16/43	41.6	16.3/33.3
12297	X2.1	5.75	2.68	1080	X	88	42.8	35.5
12673	X2.2/X9.3	6.23	0.7	1080	X	5/50	21.4	19.5
	X1.3	0.37	1.37	270	X	89	17.8	25.2

Table 5.3: Same as Table 5.2 but for constructing the 3D magnetic skeleton of ARs using the PF extrapolation. The table includes the maximum lead-time improvement of the estimated flare onset time at the optimum height for a further 10 AR cases by means of implementing the  $WG_M$  analysis for the data obtained after PF extrapolation.

## 5.4 Conclusions

In this chapter, we have investigated the evolution of the two pre-flare signatures not only at the photosphere but higher up in the lower solar atmosphere, like in Chapter 4. The aim is to improve the efficiency of the flare onset time estimation capability of the  $WG_M$  method applicable to both the PF and NLFFF computations of observed LOS ( $B_z$ ) of magnetic field data. In our presented work, we considered the pre-flare patterns as a function of height instead of the free energy of ARs, therefore, the two extrapolation methods may play equally important roles.

We substantially improved the estimation accuracy of the flare onset time and the performance quality of the  $WG_M$  method by (1) implementing an automated feature tracing code for the detection of ARs in magnetogram images, which makes the manual tracing unnecessary [Welsch and Longcope, 2003], and (2) by optimising the technique to PF [Gary, 1989] and NLFFF [Yan and Sakurai, 2000] extrapolations to build up 3D magnetic structures of the ARs. Also, we used an automated PIL detection program [Cui et al., 2006] to find the areas

of interest, i.e. the  $\delta$ -spots, for applying the  $WG_M$  method.

The  $WG_M$  method was applied to the entire individual  $\delta$ -spot(s) of the ARs where all magnetic fluxes were taken into account for the analysis. The evolution of (i) the  $WG_M$  proxy, (ii) the distance between the area-weighted barycenters of opposite polarities ( $D_{pn}$ ) and (iii) the unsigned magnetic flux ( $\Phi$ ), were followed step-by-step at each 45 km height from the photosphere up to few thousand kms. Furthermore, we carried out the necessary analysis similarly to as described in Section 2.2.4 in order to identify the relevant pre-flare behaviors of the  $WG_M$  and  $D_{pn}$  parameters before each flare cases.

In the first approach, we compared the results obtained by applying the  $WG_M$  method to PF and NLFFF extrapolation data for AR 11158, 11166 and 11283. We found that the starting and the finishing times of the converging phase *changes as a function of height*, as visualised in Figures 5.4– 5.6. At a certain height, i.e. at the so-called *optimum height*, the moment of starting time of the converging phase as well as the moment of closest approach is indeed a passable maximum earlier than at any other heights in the solar atmosphere, as shown in Figs. 5.4– 5.6. This is one of the most important findings of this work because it is useful for the earlier and improve estimating of the flare onset time. On the other hand, we also observed that the optimum heights and the lead-time improvements are different in the four investigated flare cases. Sometimes, the yielded lead-time by PF is better with few hours than in the case of NLFFF extrapolation. It is an important aspect because the 2-3 hours CPU running time of the PF extrapolations is negligible when compared to the 3-4 months of NLFFF's running time. Therefore, in further studies, we applied only the PF extrapolation and analysed with the  $WG_M$  method an additional 10 ARs with 16 flare cases.

Finally, based on our findings in the PF approaches, we would conclude that the average lead-time improvement could be  $3.2 \pm 2.5$  hours if we use the  $WG_M$  method between 1000 and 1800 km in the solar lower atmosphere. It is important to note that for a more definite and conclusive statement one may need to carry out a large ensemble of magnetic field extrapolations and apply the  $WG_M$  method to the evolution of  $\delta$ -sunspots with flares of lower GOES class (M-, and C-classes). Also, to test this finding as well as the flare precursor capability of the  $WG_M$  method, a statistically more significant sample of flaring ARs may be needed to be analysed in the future.

# Chapter 6

## Conclusions and Future Work

In this thesis, we further developed and tested the  $WG_M$  method [introduced by Korsós et al., 2015] to make it more widely applicable and reliable. In Chapter 3, we applied the method to a wide range of energetic flares, i.e. between B- and X-class flares. Furthermore, we presented an extended statistical analysis of AR cases compared to Korsós et al. [2015] and summarised our new findings. In Chapter 4, we tested the reliability of the  $WG_M$  method on synthetic data. We analysed a simulated flaring AR where four flares were identified in terms of Ohmic heating and temperature increase. We compared the findings reached by the  $WG_M$  method with the flare identification made based on the evolution of Ohmic heating and the associated temperature. In Chapter 5, we examined the characteristic pre-flare features of 13 ARs in the lower solar atmosphere by computing their 3D magnetic structures, what we also labelled as magnetic skeletons of ARs. Here, we performed a detailed comparative analysis of flare precursors between PF and NLFFF magnetic extrapolations in three flaring AR cases. Next, also in Chapter 5, we discussed our findings about the improved prediction capability of the  $WG_M$  method. Finally, here, in Chapters 6, the results of each of the investigations presented in this thesis (Chapters 3– 5) are summarised and concluding remarks with a brief future outlook are made.

## 6.1 Principal Results

The goal of this thesis is to further develop, test and apply the weighted horizontal magnetic gradient ( $WG_M$ ) flare prediction method outlined in Korsós et al. [2015] and make it more reliable. Previously, the  $WG_M$  method was based on tracking changes of the magnetic configuration of a  $\delta$ -spot in the photosphere, as flare pre-cursors, with about an hourly temporal resolution, for predicting flares above M5. The  $WG_M$  proxy itself is based on two components: (i) the total unsigned magnetic flux summed for all the considered umbrae of opposite polarities ( $\Phi$ ) and (ii) the distance between area-weighted two barycenters of the positive and negative polarities ( $D_{pn}$ ) within the entire  $\delta$ -spot. Initially, the  $WG_M$  method was developed on a sample of 61 cases using the SOHO/MDI-Debrecen Data catalogue.

In the presented empirical analyses, for all the observed 61 flare cases, two flare pre-cursor patterns were discovered with the  $WG_M$  method:

- The pre-flare behavior of the  $WG_M$  quantity itself exhibits characteristic patterns: increase, and the maximum value of the magnetic flux gradient followed by a gradual decrease prior to flaring (see in Figure 2.7).
- The pre-flare behavior pattern of the  $D_{pn}$  parameter is based on the converging-diverging motion of the area-weighted barycentres of the positive and negative polarities of the  $\delta$ -spot prior to flare. We found that the flare occurs when the value of  $D_{pn}$  is approximately ( $\pm 10\%$ ) equal to the corresponding value of  $D_{pn}$  at the beginning of the converging phase (see in Figure 2.7).

In Korsós et al. [2015], the next additional diagnostic tools were introduced to probe the pre-flare behavior patterns, where the viability of the diagnostic tools were also tested on a sample of 61 cases observed during the SOHO/MDI era:

1. The first one is the estimation of the expected flare intensity. This proxy is based on the relationship between the values of the maxima of the  $WG_M$  ( $WG_M^{max}$ ) and the highest GOES flare intensity class ( $I$ ) of ARs.
2. Next is the estimation of the flare onset time. The estimate of the onset time is based on the relationship found between the duration of diverging

motion of the opposite polarities until the flare onset and duration of the converging motion of the opposite polarities.

3. The last tool is the percentage difference ( $WG_M^{\%}$ ) calculated between the values of pre-flare  $WG_M^{max}$  and the values of  $WG_M$  at the moment of flare onset ( $WG_M^{flare}$ ). If  $WG_M^{\%}$  is over 54%, no further flare of the same class or above would be expected; but, if  $WG_M^{\%}$  is less than  $\sim 42\%$ , further flares of the same class could be probable within about an 18-hour window.

At the beginning of the thesis, three specific research questions were addressed to guide us throughout this work. The questions provided directions on how to further develop the  $WG_M$  flare prediction method and make it even more reliable. Now, we summarise the detailed concluding answers to all of these questions raised and discuss how the different kind of approaches contributed to the goal of this thesis:

- *Are the two typical pre-flare patterns valid across the entire GOES flare spectrum, or not?*

In Chapter 3, our main motivation was to further develop, improve and confirm the applicability of two potentially predictive flare precursor parameters (i.e.  $WG_M$  and  $D_{pn}$ ) introduced by K15. Here, we generalised the application of the  $WG_M$  method in two main ways. First, we have expanded the number of investigated ARs by taking into account not only ARs observed by the SOHO satellite, but also those detected by the higher spatial and temporal resolution SDO mission. Second, we extended the analysis to encompass GOES flare classes from as low as B-class to as high as X-class flares.

We investigated a total number of 127 ARs which produced flares from as small as B-class energetic flares to the strongest X-class flares and found the two distinct and characteristic pre-flare patterns of the  $WG_M$  method regularly. Furthermore, we set out empirical conditions that the  $WG_M$  and the  $D_{pn}$  parameters have to satisfy to qualify as being precursive of a flare rather than an unrelated fluctuation. After identifying the two concurrently required pre-conditions, we investigated the relationship between the largest intensity flare of the host AR in terms of the  $WG_M^{max}$ . By extending the flare samples down to B-class, we found a logarithmic relationship between the intensity  $I$  of flares hosted in the ARs and

$WG_M^{max}$  instead of the linear relationship known earlier (see the 1st point above). This updated relationship may now provide a more accurate and inclusive tool to estimate  $\log(I)$  of the expected largest flare-class from the measured  $WG_M^{max}$ .

The extended statistical sample from SDD and HMIDD data from as low energy as the B-class to highest energy as X-class flares, again, also confirmed the linear relationship between the duration of the converging motion and the time elapsed from the moment of minimum distance until the flare onset (see the 2nd point above). Therefore, we proposed that if one can reliably identify the moment when  $D_{pn}$  begins to grow again, then, one is able to estimate the onset time of the flare with  $\pm 7.2$  hrs of uncertainty.

Next, we revisited the estimated probability of further flare occurrence during the descending phase of the  $WG_M$  after its maximum (see the 3rd point above). We found encouraging results extending the initial findings of K15 to a wider flare energy range, namely: if the percentage difference ( $WG_M^{\%}$ ) is over 55%, no further energetic flare(s) may be expected; but, if  $WG_M^{\%}$  is less than  $\sim 40\%$ , further flaring is probable within about 18 hrs. The importance of this empirical result is that it could be a further auxiliary tool for inferring the properties of imminent flares.

- *Can we reproduce our observational findings by a simulated flaring AR?*

In Chapter 4, we applied the concept of flare predicting capability of the  $WG_M$  method to magneto-hydrodynamic simulations generating solar-like flares. Our view was that it would be encouraging and reassuring if we do observe a similar pre-flare behavior of the  $WG_M$  and the  $D_{pn}$  parameters in the simulation as in real sunspot data discussed in Chapter 3. This would also be indicating that the predictive temporal behavior of these parameters may indeed be an intrinsic feature of the physical processes preceding flare onset. The fact, that the application of the  $WG_M$  method gives similar precursors for observed (GOES B-, C-, M- and X-class) flares as well as the simulated (B- and C-class) flares, also gives us confidence that a basic physical mechanism of flare initiation has been *phenomenologically* captured reasonably well in the flare simulation, reported in Chatterjee et al. [2016].

In particular, four flares were simulated and classified as two B- ( $B_1$  and  $B_2$ ) and two C- ( $C_1$  and  $C_2$ ) classes. To this simulated flaring AR, we

applied the  $WG_M$  method, put forward in Chapter 3 in the context of identifying flare pre-cursors, tracked the temporal evolution of the  $WG_M$ , the variation of  $D_{pn}$  and the  $\Phi$  at different heights in the model solar atmosphere from photosphere up to 3.6 Mm. We successfully identified the two important and characteristic pre-flare behaviors, at stepping intervals of 100 km in height in the solar atmosphere.

Next, we investigated the variation of the moment of start time of the approaching phase, the moment of the closest approach and estimated flare onset time as a function of height. This investigation was completed by searching for specific heights at which the approaching motion of the  $D_{pn}$  corresponding to a flare event would start earlier and reach its closest approach distance earlier than at any other level (well, at least photospheric level) in the solar atmosphere, so that we may, therefore, estimate the moment of onset earlier in time. Also, the pre-flare behavior of  $WG_M$  can be recognised at the optimum heights.

It was found that for the two B-class flares, the most promising levels for flare finding the precursors of the  $WG_M$  method for an eruption are at about 0.3-0.5 Mm above the photosphere. The optimum height for the first C-class flare is between 2.2-2.7 Mm and for the last C-class flare is above 1.3 Mm. These loci in height, found for being most optimal for predicting flares, agree reasonably well with the heights of the occurrence of flares themselves as identified from the analysis of their thermal and Ohmic heating signatures in the simulation.

We also estimated the expected time of the flare onsets from the duration of the converging-receding motion of  $D_{pn}$  before each flare. The estimated onset time and the actual time of occurrence for each flare are in good agreement at the corresponding optimum heights. Therefore, we constructed that our numerical experiment serves as further mounting evidence towards confirming the underlying assumed principles, which we have put forward for potential flare predicting, based on the  $WG_M$  method.

- *Is it possible to increase the flare prediction capability of our  $WG_M$  method if we extend our investigations from the photosphere into 3D embracing an observed solar atmospheric region?*

In Chapter 5, to make an advance in developing Space Weather prediction capability (and capacity), we have generalised our prediction method, by

applying it to the Interface Region and low corona at stepping intervals of 45 km in 3D, in order to identify the optimum height for flare prediction in the lower solar atmosphere. Our motivation is based on two aspects. First, there is the general knowledge that flares actually occur higher up in the solar atmosphere, and not in the photosphere. Based on the results of Chapters 3-4, here, we expected to considerably increase the flare onset time prediction capability of the  $WG_M$  method with PF and NLFFF extrapolation computations. In our study, the two extrapolation methods played an equally important role because there is no bearing of the contained free-energy of the ARs at this stage for our main purpose; namely, we only focused on the two characteristic pre-flare patterns identified by K15 as a function of height.

We found that the moment of starting time of the converging phase as well as the moment of closest approach is indeed earlier at a certain height (labelled as the optimum height) than at any other heights in the solar atmosphere, like found in Chapter 4 when analysing the simulated flaring AR data.

We also noted that the optimum heights and the improvements in estimating the onset time are different in the three AR cases investigated. Namely, sometimes the PF extrapolation provided earliest flare onset time estimation at the corresponding optimum height, sometimes the NLFFF one did. But, the differences of the corresponding two gained lead-times are not so significant overall. Based on this finding and the required long CPU running time for the NLFFF extrapolations, we employed only the PF extrapolation in the further investigated 10 ARs.

While analysing the flare precursors for the additional 10 ARs, we also found that the moment of starting time of the converging phase as well as the moment of closest approach are indeed earlier at the considered optimum height when compared to any other heights in the solar atmosphere. In our study, the maximum starting times of the converging phases were sooner between from about 1 to 16 hrs and the moment of closest approaches ( $T_{Imp}^M$ ) were earlier between about 1 to 8 hrs.

The related optimum heights were found to split into two intervals, 90-600 km and 1000-1800 km, respectively. The measured flare onset times were in a good agreement with the estimated onset times (by Eq. (3.2) with the  $\pm 7.2$  hr uncertainty) in the 1000-1800 km optimum height range.

Next, we applied descriptive statistics on two sets of  $T_{Imp}^M$  values to determine an average lead-time within the given two optimum height intervals. The statistical mean is 2.2 hrs with the standard deviation of 1.4 hrs in the 90-600 km interval. Nevertheless, the mean is 3.2 hours and the associated standard deviation is 2.5 hrs for the data for the 1000 km to 1800 km optimum height range. Based on our findings in the PF extrapolation cases, we conclude that the average lead-time improvement could be  $3.2 \pm 2.5$  hours if we use the  $WG_M$  method between 1000 and 1800 km in the solar lower atmosphere. Here, the values of  $S_{flare}$  are also well estimated in that height range.

For a more definite and conclusive statement one may need to carry out an ensemble of magnetic field extrapolations of the evolution of  $\delta$ -sunspots with flares of lower GOES class (M-, and C-classes) and test this relation as well as flare pre-cursor capability of the  $WG_M$  method on a statistically significant sample of the flaring ARs.

## 6.2 Future Work

Based on the experience encountered during carrying out the research of Chapters 4– 5 a few important, research questions have emerged. To explore how to answer these questions satisfactorily further work is required. The following two points outline some directions for future improvement and further study:

- *Are the different GOES flare classes height-dependent or not?*

To find an answer to this question, first, we need to carry out an ensemble of MHD simulation of the evolution of  $\delta$ -sunspots with flares of higher GOES class (M- and X-classes). Next, we need to apply the  $WG_M$  method at different heights to identify the optimum height for M- and X-class flares, similarly as in Chapter 4. A potential next step may be that we extend the number of 3D analysis samples from B- to X-class and search for the optimum height by means of the  $WG_M$  method, analogue to Chapter 5. Finally, the comparative analysis between the optimum heights of the two approaches could provide an appropriate answer to the question raised above. Maybe, we could find a proper physical explanation for the pre-flare converging-diverging behaviour of a flaring AR.

- *Could we improve the  $WG_M$  method for CME prediction?*

In order to considerably improve the efficiency of the prediction capability based on the observed kinematics of pre-flare evolution, we propose to investigate separately the preceding signatures of flares with CME and flares without CME occurrences from the photosphere to higher up in the lower solar atmosphere. The aim of this future study is to find distinguished and predictive characteristic features between of these two fundamental eruption processes. These features, then, could be used as distinct precursors that may serve the prediction of energetic solar eruptive events like flares and CMEs.

# Appendix A

## Appendix

### A.1 List of investigated ARs in Chapter 3

The first column is the NOAA AR number. The second column is the largest flare-class during the AR's disk passage (M5< denotes classes between M5-M9.9 and M1< stands for M1-M4.9). The third and fourth columns include the starting and finishing moments and the corresponding locations of the AR analysis.

		1997			
8088	M5<	22/09 00:00	S28E53	24/09 23:59	S28E10
8100	X	03/11 00:00	S19W12	04/11 23:59	S21W39

Table A.1

		1998			
8210	X	01/05 00:00	S17W03	03/05 23:00	S17W36

Table A.2

		1999			
8485	M5<	14/03 00:00	N23E00	16/03 23:59	S14W43
8647	X	01/08 17:00	S18W18	04/08 14:00	S18W63
8771	X	23/11 16:00	S15W20	27/11 13:00	S14W71
8806	M5<	20/12 00:00	N24E48	25/12 00:00	N24W18

Table A.3

		2000			
8882	X	01/03 00:00	S18W31	02/03 23:59	S16W60
8910	X	19/03 00:00	N11W10	22/06 23:59	N13W61
9026	X	04/06 00:00	N20E48	08/06 23:59	N22W17
9077	X	10/07 00:00	N18E55	14/07 23:59	N18W09
9090	M5<	20/07 00:00	N11E32	21/07 10:00	N12E05
9087	M5<	18/07 00:00	S12E28	19/07 23:59	S12E13
9097	M5<	23/07 00:00	N06E25	25/07 23:59	N08W15
9165	M5<	15/09 00:00	N13E14	19/09 10:00	N14W40

Table A.4

		2001			
9368	M5<	07/03 12:00	N25W15	08/03 23:59	N26W33
9393	X	26/03 00:00	N20E39	02/04 23:59	N16W70
9415	X	05/04 00:00	S21E60	14/04 23:59	S22W72
9433	M5<	23/04 00:00	N17E26	29/04 23:59	N17W50
9503	M5<	21/06 00:00	N16W20	22/06 23:59	N17W46
9511	X	22/06 14:00	N10E30	23/06 23:59	N10E00
9601	M5<	04/09 00:00	N14W06	05/09 23:59	N14W38
9608	M5<	14/09 00:00	S25W33	17/09 23:59	S28W75
9628	M5<	23/09 00:00	S17E25	27/09 23:59	S18W01
9632	X	22/09 00:00	S17E56	24/09 23:59	S19E06
9661	X	13/10 00:00	N14E55	19/10 23:59	N16W35
9672	X	23/10 00:00	S18E13	25/10 23:59	S18W27
9684	X	01/11 00:00	N06E29	04/11 23:59	N05W28
9704	X	17/11 00:00	S18E41	22/10 23:59	S18W38
9727	M5<	09/12 00:00	S22E03	12/12 23:59	S21W52
9733	X	10/12 00:00	N14E58	18/12 23:59	N13W65
9742	M5<	22/12 00:00	N10W03	26/12 23:59	N12W68

Table A.5

		2002			
9773	M5<	08/01 14:00	N12E17	09/01 23:59	N14W05
9866	M5<	12/03 00:00	S10E43	14/03 23:59	S10E07
10017	X	02/07 00:00	S19W37	03/07 23:59	S18W63
10044	M5<	25/07 17:00	S20E34	26/07 23:59	S21E17
10069	X	14/08 00:00	S07E50	21/08 06:00	S08W50
10226	M5<	16/12 00:00	S28E25	20/12 23:59	S28W41

Table A.6

		2003			
10314	X	15/03 11:00	S14W05	18/03 23:59	S16W52
10338	M5<	22/04 11:00	N18W10	26/04 23:59	N18W71
10365	X	25/05 00:00	S08E11	30/05 23:59	S07W59
10375	X	06/06 00:00	N12E24	11/06 23:59	N12W62
10484	X	20/10 00:00	N06E53	28/10 23:59	N03W68
10486	X	25/10 00:00	N06E53	02/11 23:59	N03W68
10488	X	28/10 00:00	N09E09	03/11 12:00	N08W74
10501	M5<	15/11 00:00	N04E61	21/11 23:59	N02W18

Table A.7

		2004			
10564	X	23/02 00:00	N13E26	26/02 23:59	N14W27
10649	X	14/07 00:00	S10E64	19/07 23:59	S10E00
10652	M5<	21/07 00:00	N10E32	22/07 23:59	N08E06
10691	X	29/10 14:00	N15W02	30/10 23:59	N14W25
10696	X	04/11 00:00	N09E32	10/11 23:59	N08W62
10715	X	30/12 00:00	N04E61	31/12 23:59	N04E34

Table A.8

		2005			
10720	X	12/01 00:00	N13E52	20/01 23:59	N14W70
10759	M5<	11/05 00:00	N12E50	13/05 23:59	N12E06

Table A.9

		2006			
10875	M5<	25/04 00:00	S10E62	27/04 23:59	S11E20
10930	X	11/12 00:00	S05E06	15/12 23:59	S06W59

Table A.10

		2010			
11045	M5<	06/02 04:00	N24E20	08/02 23:59	N23W17
11046	M5<	10/02 00:00	N24E42	12/02 23:59	N24E00
11066	B	03/05 00:00	S27E16	03/05 23:59	S27E04
11069	M1<	05/05 00:00	N40W20	07/05 23:59	N40W63
11078	B	08/06 08:00	S21W40	09/06 23:59	S21W61
11081	C	12/07 00:00	N23W45	13/07 10:00	N23W66
11092	C	31/07 18:00	N13E50	01/08 23:59	N13E20
11099	C	13/08 11:00	N19W42	14/08 23:59	N19W60
11109	C	13/08 11:00	N19W42	14/08 23:59	N19W60
11117	C	24/10 00:00	S22E24	11/10 12:00	S22W70
11123	C	11/10 12:00	N20E23	11/10 12:00	N20W16
11130	C	30/11 00:00	N13W54	02/12 23:59	N13W54

Table A.11

		2011			
11142	C	03/01 18:00	S14E11	03/01 23:35	S14E08
11158	X	12/02 00:00	S19E25	15/02 23:59	S21W27
11164	M1<	05/03 00:00	N2319	07/03 23:59	N23W58
11166	X	07/03 00:00	N11E27	11/03 17:00	N09W36
11169	M1<	12/03 00:00	N17W11	15/03 23:59	N17W65
11176	M1<	24/03 00:00	S15E56	25/03 23:59	S15E30
11190	M1<	14/04 08:00	N13W05	17/03 23:59	N13W55
11204	B	09/05 00:00	N17W43	11/05 03:00	N17W60
11210	C	09/05 00:00	N20E20	10/05 23:59	N20W08
11224	C	28/05 00:00	N21W15	30/05 00:00	N21W55
11226	M1<	05/06 06:00	S22W27	07/06 07:00	S22W55
11227	C	31/05 18:00	S20E66	02/06 08:00	S20E27
11236	C	20/06 18:00	N17E23	21/06 23:59	N17W60
11241	B	25/06 04:00	N20W05	27/06 12:00	N20W40
11244	C	03/07 00:00	N16W25	03/07 23:59	N16W40
11249	C	09/07 19:00	S19E01	11/07 12:00	S19W22
11260	M1<	26/07 16:00	N19E50	28/07 19:00	N19E20
11261	M5<	29/07 00:00	N16E48	05/08 23:59	N16W64
11281	C	31/08 19:00	S20E30	04/09 23:59	S20W12
11283	X	04/09 00:00	N13E22	10/09 23:59	N13W71
11363	C	02/12 17:00	S21E35	06/12 20:00	S21W20
11387	M1<	25/12 04:00	S21E36	27/12 23:59	S21W57

Table A.12

		2012			
11402	M5<	20/01 00:00	N24E16	23/01 23:59	N30W24
11429	X	04/03 00:00	N17E67	11/03 12:00	N17W31
11430	X	05/03 00:00	N20E38	07/03 23:59	N17E12
11455	B	13/04 00:00	N06E06	14/04 08:00	N14W24
11465	C	21/04 00:00	S18E40	27/04 23:59	S18W55
11476	M5<	07/05 00:00	N10E60	13/05 23:59	N10W37
11490	B	28/05 00:00	S12E17	28/05 15:00	S12E08
11494	M1<	05/06 18:00	S17E20	08/06 23:59	S17W32
11504	M1<	12/06 00:00	S17E40	14/06 19:00	S17E03
11512	C	26/06 00:00	S16E40	29/06 18:00	S16W14
11515	X	01/07 00:00	S17E30	07/07 23:59	S17W65
11520	X	09/07 00:00	S16E46	13/07 00:00	S17W60
11542	C	08/08 09:00	S14E63	12/08 08:00	S14W05
11553	C	30/08 09:00	S20W16	02/09 23:59	S20W68
11613	M5<	12/11 00:00	S22E57	13/11 23:59	S22E31
11618	M1<	19/11 00:00	S12E40	26/11 23:59	N06W66

Table A.13

		2013			
11719	M5<	08/04 17:00	N10E53	11/04 23:59	N11W14
11776	C	18/06 08:00	N11E11	19/06 18:00	N11W07
11818	M1<	16/08 04:00	S07W04	17/08 23:59	S07W35
11865	M1<	09/10 16:00	S22E60	15/10 15:00	S22W22
11875	X	19/10 00:00	N06E16	28/10 03:00	N06W68
11877	M5<	23/10 00:00	S12W08	24/10 10:00	S12W15
11884	M5<	29/10 04:00	S12E52	03/11 17:00	S12W21
11890	X	04/11 00:00	S11E63	12/11 23:59	S11W58
11936	M5<	30/12 00:00	S16W09	02/01 23:59	S16W67

Table A.14

		2014			
11944	X	05/01 00:00	S09E40	10/01 09:00	S09W33
11966	M5<	10/03 10:00	N14W41	12/03 22:00	N14W72
11967	M5<	31/01 00:00	S12E44	08/02 23:59	S12W63
12017	X	28/03 00:00	N10W08	30/03 23:59	N10W50
12036	M5<	15/04 00:00	S17E13	18/04 23:59	S17W40
12146	M1<	22/08 19:00	N09W01	25/08 23:59	N09W43
12158	X	07/09 15:00	N15E54	11/09 23:59	N15W12
12192	X	18/10 09:00	S13E70	27/10 15:00	S13W52
12205	X	05/11 12:00	N15E66	12 /11 23:59	N15W35
12241	M5<	18/12 00:00	S09E20	21/12 23:59	S09W34
12246	M5<	18/12 00:00	S09E20	21/12 23:59	S09W34
12242	X	15/12 15:00	S17W33	20/12 23:59	S17W33

Table A.15

## A.2 List of investigated ARs in Chapter 5

Summary table of the investigated 20 X-class flares of 13 ARs. The first column is the NOAA AR number. The second and third columns show the associated GOES flare intensity and the onset time/position of the flares. The fourth and fifth columns include the starting and finishing moments and the corresponding locations of the AR analysis. The grey shaded rows indicate that the AR has two  $\delta$ -spots identified by the automated PIL program [Cui et al., 2006].

NOAA AR	Flare			Following from:		Following to:	
	Intensity	Peak time	Position	Time	Position	Time	Position
11158	X2.2	15/02/2011 01:56	S20W12	12/02/2011 00:00	S19E26	17/02/2011 00:00	S19W40
11166	X1.5	09/03/2011 23:23	N08W09	06/03/2011 00:00	N9E40	10/03/2011 00:00	N09W40
11283	X1.8	06/09/2011 22:20	N14W18	04/09/2011 00:00	N14E22	09/09/2011 00:00	N14W40
	X2.1	07/09/2011 22:38	N14W28	04/09/2011 00:00	N14E22	09/09/2011 00:00	N14W40
11430	X1.3	07/03/2012 01:14	N22E12	04/03/2012 15:00	N20E43	09/03/2012 00:00	N20W15
11515	X1.1	06/07/2012 23:08	S16W52	29/06/2012 13:00	S16E50	07/07/2012 00:00	S16W50
11520	X1.4	12/07/2012 16:49	S15W01	08/07/2012 12:00	S17E53	15/07/2012 12:00	S17W40
11890	X1.1	08/11/2013 04:26	S14E15	05/11/2013 00:00	S11E53	12/11/2013 07:00	S11W40
	X1.1	10/11/2013 05:14	S14W13	05/11/2013 00:00	S11E53	12/11/2013 07:00	S11W40
11944	X1.2	07/01/2014 18:32	S09E12	05/01/2014 03:00	S09E37	07/01/2014 11:00	S09E06
12017	X1.0	29/03/2014 17:48	N11W32	27/03/2014 21:00	N10W06	30/03/2014 00:00	N10W40
12158	X1.6	10/09/2014 17:45	N14E02	06/09/2014 12:00	N15E60	10/09/2014 12:00	N15E06
12192	X1.6	22/10/2014 14:28	S14E13	19/10/2014 00:00	S13E60	26/10/2014 16:00	S13W40
	X3.1	24/10/2014 21:41	S16W21	19/10/2014 00:00	S13E60	26/10/2014 16:00	S13W40
	X1.0	25/10/2014 17:08	S16W31	19/10/2014 00:00	S13E60	26/10/2014 16:00	S13W40
	X2.0	26/10/2014 10:56	S18W40	519/10/2014 00:00	S13E60	26/10/2014 16:00	S13W40
12297	X2.1	11/03/2015 16:22	S17E21	08/03/2015 12:00	S17E60	16/03/2015 00:00	S17W37
12673	X2.2	06/09/2017 09:10	S09W32	03/09/2017 08:00	S10E07	07/09/2017 17:00	S10W50
	X9.3	06/09/2017 12:02	S09W33	03/09/2017 08:00	S10E07	07/09/2017 17:00	S10W50
	X1.3	07/09/2017 14:36	S09W45	03/09/2017 08:00	S10E07	07/09/2017 17:00	S10W50

Table A.16

# Bibliography

- W. P. Abbett and G. H. Fisher. A Coupled Model for the Emergence of Active Region Magnetic Flux into the Solar Corona. *Astrophys. J.*, 582:475–485, January 2003. doi: 10.1086/344613.
- A. Al-Ghraibah, L. E. Boucheron, and R. T. J. McAteer. An automated classification approach to ranking photospheric proxies of magnetic energy build-up. *Astron. Astrophys.*, 579:A64, July 2015. doi: 10.1051/0004-6361/201525978.
- C. E. Alissandrakis. On the computation of constant alpha force-free magnetic field. *Astron. Astrophys.*, 100:197–200, July 1981.
- J. J. Aly. On some properties of force-free magnetic fields in infinite regions of space. *Astrophys. J.*, 283:349–362, August 1984. doi: 10.1086/162313.
- J. J. Aly. Some properties of the solutions of a non-linear boundary value problem for a force-free field in an infinite region of space. I - Energy estimates. *Astron. Astrophys.*, 203:183–188, September 1988.
- S. K. Antiochos, C. R. DeVore, and J. A. Klimchuk. A Model for Solar Coronal Mass Ejections. *Astrophys. J.*, 510:485–493, January 1999. doi: 10.1086/306563.
- M. J. Aschwanden. *Physics of the Solar Corona. An Introduction with Problems and Solutions (2nd edition)*. December 2005.
- M. J. Aschwanden. The Vertical-current Approximation Nonlinear Force-free Field Code: Description, Performance Tests, and Measurements of Magnetic Energies Dissipated in Solar Flares. *Astrophysical Journal Supplement Series*, 224:25, June 2016. doi: 10.3847/0067-0049/224/2/25.

- M. J. Aschwanden, L. Fletcher, C. J. Schrijver, and D. Alexander. Coronal Loop Oscillations Observed with the Transition Region and Coronal Explorer. *Astrophys. J.*, 520:880–894, August 1999a. doi: 10.1086/307502.
- M. J. Aschwanden, J. S. Newmark, J.-P. Delaboudinière, W. M. Neupert, J. A. Klimchuk, G. A. Gary, F. Portier-Fozzani, and A. Zucker. Three-dimensional Stereoscopic Analysis of Solar Active Region Loops. I. SOHO/EIT Observations at Temperatures of  $(1.0-1.5)\times 10^6$  K. *Astrophys. J.*, 515:842–867, April 1999b. doi: 10.1086/307036.
- A. Asensio Ramos and J. de la Cruz Rodríguez. Sparse inversion of Stokes profiles. I. Two-dimensional Milne-Eddington inversions. *Astron. Astrophys.*, 577:A140, May 2015. doi: 10.1051/0004-6361/201425508.
- R. G. Athay and G. E. Moreton. Impulsive Phenomena of the Solar Atmosphere. I. Some Optical Events Associated with Flares Showing Explosive Phase. *Astrophys. J.*, 133:935, May 1961. doi: 10.1086/147098.
- H. W. Babcock. The Solar Magnetograph. *Astrophys. J.*, 118:387, November 1953. doi: 10.1086/145767.
- T. Baranyi, L. Gyóri, and A. Ludmány. On-line Tools for Solar Data Compiled at the Debrecen Observatory and Their Extensions with the Greenwich Sunspot Data. *Solar Phys.*, 291:3081–3102, November 2016. doi: 10.1007/s11207-016-0930-1.
- G. Barnes, K. D. Leka, C. J. Schrijver, T. Colak, R. Qahwaji, O. W. Ashamari, Y. Yuan, J. Zhang, R. T. J. McAteer, D. S. Bloomfield, P. A. Higgins, P. T. Gallagher, D. A. Falconer, M. K. Georgoulis, M. S. Wheatland, C. Balch, T. Dunn, and E. L. Wagner. A Comparison of Flare Forecasting Methods. I. Results from the All-Clear Workshop. *Astrophys. J.*, 829:89, October 2016. doi: 10.3847/0004-637X/829/2/89.
- B. M. Bein, S. Berkebile-Stoiser, A. M. Veronig, M. Temmer, and B. Vršnak. Impulsive Acceleration of Coronal Mass Ejections. II. Relation to Soft X-Ray Flares and Filament Eruptions. *Astrophys. J.*, 755:44, August 2012. doi: 10.1088/0004-637X/755/1/44.
- A. O. Benz. Flare Observations. *Living Reviews in Solar Physics*, 14:2, December 2017. doi: 10.1007/s41116-016-0004-3.

- D. Biskamp. *Magnetic Reconnection in Plasmas*. September 2000.
- M. G. Bobra, X. Sun, J. T. Hoeksema, M. Turmon, Y. Liu, K. Hayashi, G. Barnes, and K. D. Leka. The Helioseismic and Magnetic Imager (HMI) Vector Magnetic Field Pipeline: SHARPs - Space-Weather HMI Active Region Patches. *Solar Phys.*, 289:3549–3578, September 2014. doi: 10.1007/s11207-014-0529-3.
- N. S. Brickhouse and B. J. Labonte. Mass and energy flow near sunspots. I - Observations of moat properties. *Solar Phys.*, 115:43–60, March 1988. doi: 10.1007/BF00146229.
- H. Carmichael. A Process for Flares. *NASA Special Publication*, 50:451, 1964.
- R. C. Carrington. Description of a Singular Appearance seen in the Sun on September 1, 1859. *Mon. Not. Roy. Astron. Soc.*, 20:13–15, November 1859. doi: 10.1093/mnras/20.1.13.
- R. C. Carrington. On the Motion of the Solar System in Space. *Mon. Not. Roy. Astron. Soc.*, 23:203, April 1863. doi: 10.1093/mnras/23.6.203.
- R. Chandra, B. Schmieder, C. H. Mandrini, P. Démoulin, E. Pariat, T. Török, and W. Uddin. Homologous Flares and Magnetic Field Topology in Active Region NOAA 10501 on 20 November 2003. *Solar Phys.*, 269:83–104, March 2011. doi: 10.1007/s11207-010-9670-9.
- P. Chatterjee, V. Hansteen, and M. Carlsson. Modeling Repeatedly Flaring  $\delta$  Sunspots. *Physical Review Letters*, 116(10):101101, March 2016. doi: 10.1103/PhysRevLett.116.101101.
- M. C. M. Cheung and M. L. DeRosa. A Method for Data-driven Simulations of Evolving Solar Active Regions. *Astrophys. J.*, 757:147, October 2012. doi: 10.1088/0004-637X/757/2/147.
- M. C. M. Cheung, M. Schüssler, and F. Moreno-Insertis. Flux Emergence at the Photosphere. In J. Leibacher, R. F. Stein, and H. Uitenbroek, editors, *Solar MHD Theory and Observations: A High Spatial Resolution Perspective*, volume 354 of *Astronomical Society of the Pacific Conference Series*, page 97, December 2006.

- C. Cid, J. Palacios, E. Saiz, A. Guerrero, and Y. Cerrato. On extreme geomagnetic storms. *Journal of Space Weather and Space Climate*, 4(27):A28, October 2014. doi: 10.1051/swsc/2014026.
- Y. Cui, R. Li, L. Zhang, Y. He, and H. Wang. Correlation Between Solar Flare Productivity and Photospheric Magnetic Field Properties. 1. Maximum Horizontal Gradient, Length of Neutral Line, Number of Singular Points. *Solar Phys.*, 237:45–59, August 2006. doi: 10.1007/s11207-006-0077-6.
- C. E. DeForest, H. J. Hagenaar, D. A. Lamb, C. E. Parnell, and B. T. Welsch. Solar Magnetic Tracking. I. Software Comparison and Recommended Practices. *Astrophys. J.*, 666:576–587, September 2007. doi: 10.1086/518994.
- P. Démoulin. Recent theoretical and observational developments in magnetic helicity studies. *Advances in Space Research*, 39:1674–1693, 2007. doi: 10.1016/j.asr.2006.12.037.
- P. Démoulin and E. Pariat. Modelling and observations of photospheric magnetic helicity. *Advances in Space Research*, 43:1013–1031, April 2009. doi: 10.1016/j.asr.2008.12.004.
- J. W. Dungey. The motion of magnetic fields. *Mon. Not. Roy. Astron. Soc.*, 113:679, 1953. doi: 10.1093/mnras/113.6.679.
- R. B. Dunn, editor. *Solar instrumentation: What's next?*, 1981.
- T. L. Duvall, S. D'Silva, S. M. Jefferies, J. W. Harvey, and J. Schou. Downflows under sunspots detected by helioseismic tomography. *Nature*, 379:235–237, January 1996. doi: 10.1038/379235a0.
- T. Emonet and F. Moreno-Insertis. The Physics of Twisted Magnetic Tubes Rising in a Stratified Medium: Two-dimensional Results. *Astrophys. J.*, 492:804–821, January 1998. doi: 10.1086/305074.
- Pulkkinen A. A. Zheng Y. Mays M. L. Taktakishvili A. Kuznetsova M. M. Hesse M. Evans, R. M. The SCORE Scale: A Coronal Mass Ejection Typification System Based On Speed. *Space Weather*, 11:333, June 2013.
- J. Evershed. Radial movement in sun-spots. *Mon. Not. Roy. Astron. Soc.*, 69:454, March 1909. doi: 10.1093/mnras/69.5.454.

- Y. Fan. CMEs due to Loss of Confinement of Coronal Flux Ropes. In *37th COSPAR Scientific Assembly*, volume 37 of *COSPAR Meeting*, page 851, 2008.
- T. G. Forbes and E. R. Priest. A comparison of analytical and numerical models for steadily driven magnetic reconnection. *Reviews of Geophysics*, 25:1583–1607, November 1987. doi: 10.1029/RG025i008p01583.
- T. G. Forbes and E. R. Priest. Photospheric Magnetic Field Evolution and Eruptive Flares. *Astrophys. J.*, 446:377, June 1995. doi: 10.1086/175797.
- P. A. Fox, S. Sofia, and K. L. Chan. Convective flows around sunspot-like objects. *Solar Phys.*, 135:15–42, September 1991. doi: 10.1007/BF00146696.
- G. A. Gary. Linear force-free magnetic fields for solar extrapolation and interpretation. *Astrophysical Journal Supplement Series*, 69:323–348, February 1989. doi: 10.1086/191316.
- M. K. Georgoulis. Are Solar Active Regions with Major Flares More Fractal, Multifractal, or Turbulent Than Others? *Solar Phys.*, 276:161–181, February 2012. doi: 10.1007/s11207-010-9705-2.
- M. K. Georgoulis. Toward an Efficient Prediction of Solar Flares: Which Parameters, and How? *Entropy*, 15:5022–5052, November 2013. doi: 10.3390/e15115022.
- R. G. Giovanelli. A Theory of Chromospheric Flares. *Nature*, 158:81–82, July 1946. doi: 10.1038/158081a0.
- J. T. Gosling, E. Hildner, R. M. MacQueen, R. H. Munro, A. I. Poland, and C. L. Ross. The speeds of coronal mass ejection events. *Solar Phys.*, 48:389–397, June 1976. doi: 10.1007/BF00152004.
- L. Győri. Automation of Area Measurement of Sunspots. *Solar Phys.*, 180:109–130, June 1998. doi: 10.1023/A:1005081621268.
- L. Győri. Automation of Tracking Various Sunspot Group Entities and Demonstrating Its Usage on the Flaring NOAA AR 11429. *Solar Phys.*, 290:1627–1645, June 2015. doi: 10.1007/s11207-015-0714-z.

- L. Gyóri, T. Baranyi, and A. Ludmány. Photospheric data programs at the Debrecen Observatory. In D. Prasad Choudhary and K. G. Strassmeier, editors, *IAU Symposium*, volume 273 of *IAU Symposium*, pages 403–407, August 2011. doi: 10.1017/S174392131101564X.
- G. E. Hale, F. Ellerman, S. B. Nicholson, and A. H. Joy. The Magnetic Polarity of Sun-Spots. *Astrophys. J.*, 49:153, April 1919. doi: 10.1086/142452.
- P. S. Hardersen, K. Balasubramaniam, S. Shkolyar, and B. Zak. Intrinsic Sunspot Rotations and Energetic Events. In *AAS/Solar Physics Division Abstracts #42*, volume 43 of *Bulletin of the American Astronomical Society*, page 17.16, May 2011.
- R. A. Harrison. The nature of solar flares associated with coronal mass ejection. *Astron. Astrophys.*, 304:585, December 1995.
- G. Herzberg. *Molecular spectra and molecular structure. Vol.1: Spectra of diatomic molecules*. 1950.
- J. Heyvaerts, E. R. Priest, and D. M. Rust. An emerging flux model for the solar flare phenomenon. *Astrophys. J.*, 216:123–137, August 1977. doi: 10.1086/155453.
- B. W. Hindman, D. A. Haber, and J. Toomre. Subsurface Circulations within Active Regions. *Astrophys. J.*, 698:1749–1760, June 2009. doi: 10.1088/0004-637X/698/2/1749.
- T. Hirayama. Theoretical Model of Flares and Prominences. I: Evaporating Flare Model. *Solar Phys.*, 34:323–338, February 1974. doi: 10.1007/BF00153671.
- R. F. Howard. Axial tilt angles of sunspot groups. *Solar Phys.*, 136:251–262, December 1991. doi: 10.1007/BF00146534.
- T. A. Howard and R. A. Harrison. Stealth Coronal Mass Ejections: A Perspective. *Solar Phys.*, 285:269–280, July 2013. doi: 10.1007/s11207-012-0217-0.
- F. Hoyle. *Some recent researches in solar physics*. 1949.
- H. Isobe, H. Takasaki, and K. Shibata. Measurement of the Energy Release Rate and the Reconnection Rate in Solar Flares. *Astrophys. J.*, 632:1184–1195, October 2005. doi: 10.1086/444490.

- C. Jiang and X. Feng. Extrapolation of the Solar Coronal Magnetic Field from SDO/HMI Magnetogram by a CESE-MHD-NLFFF Code. *Astrophys. J.*, 769:144, June 2013. doi: 10.1088/0004-637X/769/2/144.
- R. A. Kopp and G. W. Pneuman. Magnetic reconnection in the corona and the loop prominence phenomenon. *Solar Phys.*, 50:85–98, October 1976. doi: 10.1007/BF00206193.
- M. B. Korsós and M. S. Ruderman. On Flare and CME Predictability Based on Sunspot Group Evolution. In I. Dorotovic, C. E. Fischer, and M. Temmer, editors, *Coimbra Solar Physics Meeting: Ground-based Solar Observations in the Space Instrumentation Era*, volume 504 of *Astronomical Society of the Pacific Conference Series*, page 43, April 2016.
- M. B. Korsós, T. Baranyi, and A. Ludmány. Pre-flare Dynamics of Sunspot Groups. *Astrophys. J.*, 789:107, July 2014. doi: 10.1088/0004-637X/789/2/107.
- M. B. Korsós, A. Ludmány, R. Erdélyi, and T. Baranyi. On Flare Predictability Based on Sunspot Group Evolution. *Astrophys. J. Lett.*, 802:L21, April 2015. doi: 10.1088/2041-8205/802/2/L21.
- M. B. Korsós, P. Chatterjee, and R. Erdélyi. Applying the Weighted Horizontal Magnetic Gradient Method to a Simulated Flaring Active Region. *Astrophys. J.*, 857:103, April 2018. doi: 10.3847/1538-4357/aab891.
- A. G. Kosovichev and V. V. Zharkova. X-ray flare sparks quake inside Sun. *Nature*, 393:317–318, May 1998. doi: 10.1038/30629.
- R. M. Kulsrud. Magnetic reconnection in a magnetohydrodynamic plasma. *Physics of Plasmas*, 5:1599–1606, May 1998. doi: 10.1063/1.872827.
- H. Künzel. Die Flare-Häufigkeit in Fleckengruppen unterschiedlicher Klasse und magnetischer Struktur. *Astronomische Nachrichten*, 285:271, August 1960. doi: 10.1002/asna.19592850516.
- C. Liu, N. Deng, J. Lee, T. Wiegmann, C. Jiang, B. R. Dennis, Y. Su, A. Donea, and H. Wang. Three-dimensional Magnetic Restructuring in Two Homologous Solar Flares in the Seismically Active NOAA AR 11283. *Astrophys. J.*, 795:128, November 2014. doi: 10.1088/0004-637X/795/2/128.

- R. E. Loughhead and R. J. Bray. The Wilson Effect in Sunspots. *Australian Journal of Physics*, 11:177, June 1958. doi: 10.1071/PH580177.
- R. E. Louis, B. Kliem, B. Ravindra, and G. Chintzoglou. Triggering an Eruptive Flare by Emerging Flux in a Solar Active-Region Complex. *Solar Phys.*, 290: 3641–3662, December 2015. doi: 10.1007/s11207-015-0726-8.
- S. Masuda, T. Kosugi, H. Hara, S. Tsuneta, and Y. Ogawara. A loop-top hard X-ray source in a compact solar flare as evidence for magnetic reconnection. *Nature*, 371:495–497, October 1994. doi: 10.1038/371495a0.
- P. S. McIntosh. The classification of sunspot groups. *Solar Phys.*, 125:251–267, February 1990. doi: 10.1007/BF00158405.
- D. B. Melrose. Current Paths in the Corona and Energy Release in Solar Flares. *Astrophys. J.*, 451:391, September 1995. doi: 10.1086/176228.
- Z. Mikic and J. A. Linker. Disruption of coronal magnetic field arcades. *Astrophys. J.*, 430:898–912, August 1994. doi: 10.1086/174460.
- W. M. Neupert. Comparison of Solar X-Ray Line Emission with Microwave Emission during Flares. *Astrophys. J. Lett.*, 153:L59, July 1968. doi: 10.1086/180220.
- E. Parker. *Cosmical Magnetic Fields*. February 1979.
- E. N. Parker. Sweet’s Mechanism for Merging Magnetic Fields in Conducting Fluids. *J. Geophys. Res.*, 62:509–520, December 1957. doi: 10.1029/JZ062i004p00509.
- E. N. Parker. Dynamics of the Interplanetary Gas and Magnetic Fields. *Astrophys. J.*, 128:664, November 1958. doi: 10.1086/146579.
- E. N. Parker. The Solar-Flare Phenomenon and the Theory of Reconnection and Annihilation of Magnetic Fields. *Astrophysical Journal Supplement Series*, 8:177, July 1963. doi: 10.1086/190087.
- S. Patsourakos, A. Vourlidas, and G. Stenborg. Direct Evidence for a Fast Coronal Mass Ejection Driven by the Prior Formation and Subsequent Destabilization of a Magnetic Flux Rope. *Astrophys. J.*, 764:125, February 2013. doi: 10.1088/0004-637X/764/2/125.

- A. G. Petschek. Author's Reply to the Preceding Discussion. *J. Geophys. Res.*, 69:1428–1428, April 1964. doi: 10.1029/JZ069i007p01428.
- E. Priest. *Magnetohydrodynamics of the Sun*. May 2014.
- E. Priest and T. Forbes. *Magnetohydrodynamics*. November 2000. doi: 10.1888/0333750888/1983.
- C. T. Russell, R. A. Mewaldt, J. G. Luhmann, G. M. Mason, T. T. von Rosenvinge, C. M. S. Cohen, R. A. Leske, R. Gomez-Herrero, A. Klassen, A. B. Galvin, and K. D. C. Simunac. The Very Unusual Interplanetary Coronal Mass Ejection of 2012 July 23: A Blast Wave Mediated by Solar Energetic Particles. *Astrophys. J.*, 770:38, June 2013. doi: 10.1088/0004-637X/770/1/38.
- I. Sammis, F. Tang, and H. Zirin. The Dependence of Large Flare Occurrence on the Magnetic Structure of Sunspots. *Astrophys. J.*, 540:583–587, September 2000. doi: 10.1086/309303.
- P. H. Scherrer, R. S. Bogart, R. I. Bush, J. T. Hoeksema, A. G. Kosovichev, J. Schou, W. Rosenberg, L. Springer, T. D. Tarbell, A. Title, C. J. Wolfson, I. Zayer, and MDI Engineering Team. The Solar Oscillations Investigation - Michelson Doppler Imager. *Solar Phys.*, 162:129–188, December 1995. doi: 10.1007/BF00733429.
- P. H. Scherrer, J. Schou, R. I. Bush, A. G. Kosovichev, R. S. Bogart, J. T. Hoeksema, Y. Liu, T. L. Duvall, J. Zhao, A. M. Title, C. J. Schrijver, T. D. Tarbell, and S. Tomczyk. The Helioseismic and Magnetic Imager (HMI) Investigation for the Solar Dynamics Observatory (SDO). *Solar Phys.*, 275: 207–227, January 2012. doi: 10.1007/s11207-011-9834-2.
- R. Schlichenmaier and S. K. Solanki. On the heat transport in a sunspot penumbra. *Astron. Astrophys.*, 411:257–262, November 2003. doi: 10.1051/0004-6361:20031120.
- H. U. Schmidt. On the Observable Effects of Magnetic Energy Storage and Release Connected With Solar Flares. *NASA Special Publication*, 50:107, 1964.
- J. Schou, P. H. Scherrer, R. I. Bush, R. Wachter, S. Couvidat, M. C. Rabello-Soares, R. S. Bogart, J. T. Hoeksema, Y. Liu, T. L. Duvall, D. J. Akin, B. A.

- Allard, J. W. Miles, R. Rairden, R. A. Shine, T. D. Tarbell, A. M. Title, C. J. Wolfson, D. F. Elmore, A. A. Norton, and S. Tomczyk. Design and Ground Calibration of the Helioseismic and Magnetic Imager (HMI) Instrument on the Solar Dynamics Observatory (SDO). *Solar Phys.*, 275:229–259, January 2012. doi: 10.1007/s11207-011-9842-2.
- C. J. Schrijver. A Characteristic Magnetic Field Pattern Associated with All Major Solar Flares and Its Use in Flare Forecasting. *Astrophys. J. Lett.*, 655:L117–L120, February 2007. doi: 10.1086/511857.
- R. Schwenn, J. C. Raymond, D. Alexander, A. Ciaravella, N. Gopalswamy, R. Howard, H. Hudson, P. Kaufmann, A. Klassen, D. Maia, G. Munoz-Martinez, M. Pick, M. Reiner, N. Srivastava, D. Tripathi, A. Vourlidis, Y.-M. Wang, and J. Zhang. Coronal Observations of CMEs. Report of Working Group A. *Space Sci. Rev.*, 123:127–176, March 2006. doi: 10.1007/s11214-006-9016-y.
- B. V. Somov, T. Kosugi, and T. Sakao. Collisionless Three-dimensional Reconnection In Impulsive Solar Flares. *Astrophys. J.*, 497:943–956, April 1998. doi: 10.1086/305492.
- P. A. Sturrock. Model of the High-Energy Phase of Solar Flares. *Nature*, 211: 695–697, August 1966. doi: 10.1038/211695a0.
- P. A. Sturrock. Maximum energy of semi-infinite magnetic field configurations. *Astrophys. J.*, 380:655–659, October 1991. doi: 10.1086/170620.
- P. A. Sweet. The topology of force-free magnetic fields. *The Observatory*, 78: 30–32, February 1958.
- J. H. Thomas and N. O. Weiss. Fine Structure in Sunspots. *Ann. Rev. of Astron. Astrophys.*, 42:517–548, September 2004. doi: 10.1146/annurev.astro.42.010803.115226.
- T. Török and B. Kliem. The evolution of twisting coronal magnetic flux tubes. *Astron. Astrophys.*, 406:1043–1059, August 2003. doi: 10.1051/0004-6361:20030692.
- B. Tsurutani, M. Abdu, T. Araki, G. Lakhina, A. Mannucci, H. McCreddie, A. Saito, J. Sobral, T. Tsuda, and O. Verkhoglyadova. The Dayside Superfountain Effect: October 30, 2003 (Halloween) Magnetic Storm. *AGU Fall Meeting Abstracts*, December 2005a.

- B. T. Tsurutani, W. D. Gonzalez, G. S. Lakhina, and S. Alex. Reply to comment by S.-I. Akasofu and Y. Kamide on “The extreme magnetic storm of 1-2 September 1859”. *Journal of Geophysical Research (Space Physics)*, 110: A09227, September 2005b. doi: 10.1029/2005JA011121.
- B. T. Tsurutani, D. L. Judge, F. L. Guarnieri, P. Gangopadhyay, A. R. Jones, J. Nuttall, G. A. Zambon, L. Didkovsky, A. J. Mannucci, B. Iijima, R. R. Meier, T. J. Immel, T. N. Woods, S. Prasad, L. Floyd, J. Huba, S. C. Solomon, P. Straus, and R. Viereck. The October 28, 2003 extreme EUV solar flare and resultant extreme ionospheric effects: Comparison to other Halloween events and the Bastille Day event. *Geophys. Res. Lett.*, 32:L03S09, January 2005c. doi: 10.1029/2004GL021475.
- Y. Uchida. A Model Flare and the Continued Post-Flare Mass Release from the Flare Region. In M. Dryer and E. Tandberg-Hanssen, editors, *Solar and Interplanetary Dynamics*, volume 91 of *IAU Symposium*, page 303, 1980.
- A. A. van Ballegooijen and P. C. H. Martens. Formation and eruption of solar prominences. *Astrophys. J.*, 343:971–984, August 1989. doi: 10.1086/167766.
- L. van Driel-Gesztelyi and L. M. Green. Evolution of Active Regions. *Living Reviews in Solar Physics*, 12:1, September 2015. doi: 10.1007/lrsp-2015-1.
- P. Vemareddy and T. Wiegmann. Quasi-static Three-dimensional Magnetic Field Evolution in Solar Active Region NOAA 11166 Associated with an X1.5 Flare. *Astrophys. J.*, 792:40, September 2014. doi: 10.1088/0004-637X/792/1/40.
- P. Vemareddy, A. Ambastha, R. A. Maurya, and J. Chae. On the Injection of Helicity by the Shearing Motion of Fluxes in Relation to Flares and Coronal Mass Ejections. *Astrophys. J.*, 761:86, December 2012. doi: 10.1088/0004-637X/761/2/86.
- P. Vemareddy, X. Cheng, and B. Ravindra. Sunspot Rotation as a Driver of Major Solar Eruptions in the NOAA Active Region 12158. *Astrophys. J.*, 829:24, September 2016. doi: 10.3847/0004-637X/829/1/24.
- J. E. Vernazza, E. H. Avrett, and R. Loeser. Structure of the solar chromosphere. III - Models of the EUV brightness components of the quiet-sun. *Astrophysical Journal Supplement Series*, 45:635–725, April 1981. doi: 10.1086/190731.

- S. Wang, C. Liu, R. Liu, N. Deng, Y. Liu, and H. Wang. Response of the Photospheric Magnetic Field to the X2.2 Flare on 2011 February 15. *Astrophys. J. Lett.*, 745:L17, February 2012. doi: 10.1088/2041-8205/745/2/L17.
- D. F. Webb and T. A. Howard. Coronal Mass Ejections: Observations. *Living Reviews in Solar Physics*, 9, June 2012. doi: 10.12942/lrsp-2012-3.
- B. T. Welsch and D. W. Longcope. Magnetic Helicity Injection by Horizontal Flows in the Quiet Sun. I. Mutual-Helicity Flux. *Astrophys. J.*, 588:620–629, May 2003. doi: 10.1086/368408.
- T. Wiegmann and T. Sakurai. Solar Force-free Magnetic Fields. *Living Reviews in Solar Physics*, 9, September 2012. doi: 10.12942/lrsp-2012-5.
- M. Yamada. Review of controlled laboratory experiments on physics of magnetic reconnection. *J. Geophys. Res.*, 104:14529–14542, July 1999. doi: 10.1029/1998JA900169.
- M. Yamada, R. Kulsrud, and H. Ji. Magnetic reconnection. *Reviews of Modern Physics*, 82:603–664, January 2010. doi: 10.1103/RevModPhys.82.603.
- X. L. Yan and Z. Q. Qu. Rapid rotation of a sunspot associated with flares. *Astron. Astrophys.*, 468:1083–1088, June 2007. doi: 10.1051/0004-6361:20077064.
- X.-L. Yan, Z.-Q. Qu, C.-L. Xu, Z.-K. Xue, and D.-F. Kong. The causality between the rapid rotation of a sunspot and an X3.4 flare. *Research in Astronomy and Astrophysics*, 9:596–602, May 2009. doi: 10.1088/1674-4527/9/5/010.
- Y. Yan and Z. Li. Direct Boundary Integral Formulation for Solar Non-constant- $\alpha$  Force-free Magnetic Fields. *Astrophys. J.*, 638:1162–1168, February 2006. doi: 10.1086/499064.
- Y. Yan and T. Sakurai. New Boundary Integral Equation Representation for Finite Energy Force-Free Magnetic Fields in Open Space above the Sun. *Solar Phys.*, 195:89–109, July 2000. doi: 10.1023/A:1005248128673.
- S. Yang, J. Zhang, and Y. Xiang. Magnetic reconnection between small-scale loops observed with the New Vacuum Solar Telescope. *Astrophys. J. Lett.*, 798:L11–L17, January 2015. doi: 10.1088/2041-8205/798/1/L11.

- W. H. Yang, P. A. Sturrock, and S. K. Antiochos. Force-free magnetic fields - The magneto-frictional method. *Astrophys. J.*, 309:383–391, October 1986. doi: 10.1086/164610.
- S. Yashiro, S. Akiyama, N. Gopalswamy, and R. A. Howard. Different Power-Law Indices in the Frequency Distributions of Flares with and without Coronal Mass Ejections. *Astrophys. J. Lett.*, 650:L143–L146, October 2006. doi: 10.1086/508876.
- Y. Ye, M. B. Korsós, and R. Erdélyi. Detailed analysis of dynamic evolution of three Active Regions at the photospheric level before flare and CME occurrence. *Advances in Space Research*, 61:673–682, January 2018. doi: 10.1016/j.asr.2017.09.038.
- J. Zhang, K. P. Dere, R. A. Howard, M. R. Kundu, and S. M. White. On the Temporal Relationship between Coronal Mass Ejections and Flares. *Astrophys. J.*, 559:452–462, September 2001. doi: 10.1086/322405.
- J. Zhang, L. Li, and Q. Song. Interaction between a Fast Rotating Sunspot and Ephemeral Regions as the Origin of the Major Solar Event on 2006 December 13. *Astrophys. J. Lett.*, 662:L35–L38, June 2007. doi: 10.1086/519280.
- R. Zheng, M. B. Korsós, and R. Erdélyi. Semicircular-like Secondary Flare Ribbons Associated with a Failed Eruption. *Astrophys. J.*, 809:45, August 2015. doi: 10.1088/0004-637X/809/1/45.
- C. Zwaan. The emergence of magnetic flux. *Solar Phys.*, 100:397–414, October 1985. doi: 10.1007/BF00158438.